Chapter 9

Fourth-Order Statistics: Strong Fluctuation Theory

Overview: In this chapter we extend our examination begun in Chap. 8 of various fourth-order statistical quantities, like the *scintillation index* and the *irradiance covariance function*, to the strong fluctuation regime. We develop separate scintillation models for plane waves, spherical waves, and Gaussian-beam waves. These models evolve from the extended Rytov theory (Chap. 5) by taking into account the role of decreasing spatial coherence of the optical wave as it propagates further and further through the random medium. The net result is a modification of the atmospheric spectrum to an "effective spectrum" arising in the form of a multiplicative spatial filter function that eliminates the effects of moderate-sized refractive-index scales (or turbulent "eddies") under strong fluctuation conditions. This is similar to the use of spatial filters in adaptive optics applications to eliminate piston and tilt effects (among others) in the received wave front.

Under the general irradiance fluctuation theory developed here, the covariance function acquires a two-scale behavior in the strong fluctuation regime, consistent with earlier theories. From the *frozen-turbulence hypothesis*, we can infer the *temporal covariance function* from which we calculate the *temporal spectrum* of irradiance fluctuations. As shown in Chap. 8, the spectral width is determined by the transverse wind velocity scaled by the first Fresnel zone under weak irradiance fluctuations, but the power becomes concentrated at higher and higher frequencies as the strength of turbulence increases. Nonetheless, under strong irradiance fluctuations the two-scale behavior in the covariance function is also evident in the power spectrum.

In the last two sections, we review probability distribution models proposed for the irradiance fluctuations, including the gamma-gamma distribution that is theoretically valid under all fluctuation conditions. A favorable characteristic of the gamma-gamma distribution is that it has two parameters that are completely determined by atmospheric conditions.

9.1 Introduction

The topic of *optical scintillation* has been studied for many years. Early investigations concerning the scintillation of unbounded plane waves and spherical waves led to the classical monographs published in the early 1960s by Tatarskii [1] and by Chernov [2], but their scintillation results were limited to *weak fluctuations*. Based on weak fluctuation theory, Tatarskii [1,3] predicted that the *correlation width* of the irradiance fluctuations is on the order of the first Fresnel zone $\sqrt{L/k}$, where L denotes propagation path length and $k = 2\pi/\lambda$ is optical wave number. The Fresnel zone defines the most effective turbulent cell size in producing scintillation at distance L from the source. That is, turbulent cell sizes smaller than the Fresnel zone contribute less to scintillation because of the weaker refractivity fluctuations associated with them, and cell sizes larger than

the Fresnel zone do not diffract light through a large enough angle to reach the receiver.

The *saturation effect* of the scintillation index under *strong irradiance fluctuations* was first observed experimentally in 1965 by Gracheva and Gurvich [4]. This work attracted much attention and stimulated a number of theoretical and experimental studies devoted to irradiance fluctuations under strong fluctuation conditions. In particular, measurements [5,6] of the irradiance covariance function revealed that the correlation width decreases from $\sqrt{L/k}$ with increasing values of the Rytov variance σ_R^2 beyond unity, and that a large residual correlation tail emerges at large separation distances.

In an effort to better understand the theoretical foundation of the saturation phenomenon, several qualitative models describing the underlying physics associated with amplitude or irradiance fluctuations were developed in the mid-1970s. Yura [7] generalized Tatarskii's physical optics model to include the loss of spatial coherence of the wave as it propagates into the strong fluctuation regime. His results are primarily an order of magnitude estimate rather than a rigorous quantitative derivation, but he demonstrated that the scintillation index saturates at a value on the order of unity. Clifford et al. [8] extended Tatarskii's theory to the log-amplitude variance under strong fluctuations and showed why the smallest scales of irradiance fluctuations persist into the saturation regime. This latter model, called the heuristic theory, was subsequently modified by Hill and Clifford [9]. Although quantitative predictions from Yura's physical model and the heuristic theory of Hill and Clifford do not fully agree with other results [10,11], the basic qualitative arguments presented in these early models are still valid. The first asymptotic theory for the saturation regime under the assumption of Kolmogorov turbulence was published in 1974 by Gochelashvili and Shishov [12]. Inner-scale models for the saturation regime were later introduced by Fante [13] for the plane wave and by Frehlich [14] for the spherical wave. Unfortunately, numerical predictions from these asymptotic theories generally do not match experimental measurements [15–18] or numerical simulation results [19–24] for the scintillation index. In particular, the slopes of the scintillation curves from these theoretical models in the saturation regime do not agree with simulation results [25].

More recently, refinements made in the above physics-based models have led to a scintillation theory that is valid from weak fluctuations through strong fluctuations, including the deep saturation regime [26–30]. Specifics of the basic physics model leading to this theory are summarized in this chapter.

9.2   Modeling Optical Scintillation

Experimental data reveal that the *scintillation index* σ_I^2 increases initially within the regime of weak irradiance fluctuations with increasing values of the *Rytov variance* $\sigma_R^2 = 1.23 C_n^2 k^{7/6} L^{11/6}$, where C_n^2 is the *refractive index structure constant*. It then increases beyond unity and reaches its maximum value in the so-called *focusing regime* (possibly becoming as large as 5 or 6). With increasing path length, or increasing C_n^2, the focusing effect is weakened by the loss of spatial
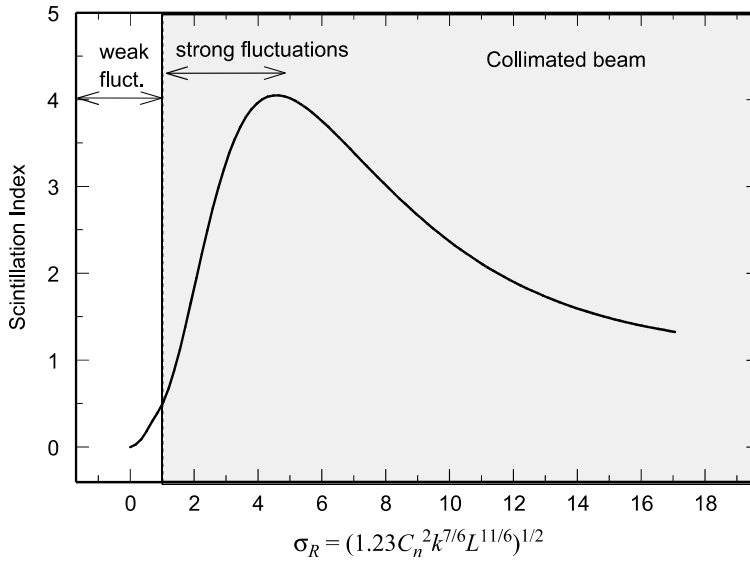
Figure 9.1 Typical behavior of the scintillation index of a collimated beam as a function of σ_R. The shaded area corresponds to strong fluctuations.

coherence and the scintillation index gradually decreases toward a value of unity as the Rytov variance increases without bound. This general behavior is depicted in Fig. 9.1 where we show a typical scintillation curve for a collimated beam as a function of σ_R. The vertical dashed line represents the division between regimes of weak fluctuations and strong fluctuations.

9.2.1 Extended Rytov theory

The conventional Rytov approximation is limited to weak fluctuation conditions in describing optical scintillation because it does not account for the role of the decreasing transverse spatial coherence radius of the propagating wave. To develop a relatively simple model for irradiance fluctuations that is applicable in moderate-to-strong fluctuation regimes, we will use a modification of the Rytov method called the *extended Rytov theory* (see Section 5.9). This variation of the conventional Rytov theory as applied to scintillation statistics is based on the following assumptions:

- The refractive index $n_1(\mathbf{R})$ can be replaced by an "effective" refractive index that is a simple sum of two terms that represent only large-scale inhomogeneities $n_X(\mathbf{R})$ and small-scale inhomogeneities $n_Y(\mathbf{R})$, i.e.,

$$n_{1,e}(\mathbf{R}) = n_X(\mathbf{R}) + n_Y(\mathbf{R}).$$

- The Rytov method for optical scintillation is valid even into the saturation regime by properly accounting for the loss of spatial coherence of the

optical wave in strong fluctuation regimes through the use of the "effective" refractive index.

- The received irradiance of an optical wave can be modeled as a modulation process in which small-scale (diffractive) fluctuations are multiplicatively modulated by statistically independent large-scale (refractive) fluctuations.

By invoking the first assumption above, it was shown in Section 5.9 that

$$U(\mathbf{r}, L) = U_0(\mathbf{r}, L) \exp[\psi_X(\mathbf{r}, L) + \psi_Y(\mathbf{r}, L)]$$
$$= U_0(\mathbf{r}, L) \exp[\psi_X(\mathbf{r}, L)] \exp[\psi_Y(\mathbf{r}, L)], \tag{1}$$

where $\psi_X(\mathbf{r},L)$ and $\psi_Y(\mathbf{r},L)$ are statistically independent complex phase perturbations due only to large-scale and small-scale effects of the effective refractive index, respectively, on the propagating wave. We note that additivity in the complex phase perturbations in Eq. (1) is equivalent to a "modulation" of small-scale effects on the optical field by large-scale effects. Because we assume large-scale effects are statistically independent of small-scale effects, it follows that all field moments deduced from (1) also lead to a similar modulation process.

To help identify what is considered "large scale" and what is "small scale" in reference to a propagating wave, we previously identified the following special scale sizes (see Section 5.9):

- the *inner scale of turbulence* l_0
- the *spatial coherence radius* of the optical wave ρ_0
- the first Fresnel zone $\sqrt{L/k}$
- the *beam radius W*
- the *scattering disk* $L/k\rho_0$
- the *outer scale of turbulence* L_0

In general, the first three scale sizes listed above are considered measures of the small-scale inhomogeneities and the last three are measures of the large-scale inhomogeneities. However, in the development directly below on scintillation we will neglect the size of the beam in our discussion because it plays a role only in the treatment of Gaussian-beam waves (which are discussed separately in Section 9.6) and our initial treatment is based on the plane wave model.

Small-scale contributions to scintillation are primarily diffractive in nature and are associated with turbulent cells smaller than the first *Fresnel zone* $\sqrt{L/k}$ or the transverse *spatial coherence radius* ρ_0, whichever is smallest. Large-scale fluctuations in the irradiance are generated by turbulent cells larger than that of the first Fresnel zone or the *scattering disk* $L/k\rho_0$, whichever is largest, and can be described by the method of geometrical optics. Thus, in the absence of both inner scale and outer scale effects, the irradiance is mainly affected by only three cell sizes (or eddies) described by

$$l_1 \sim \rho_0, \quad \text{(spatial coherence radius)},$$

$$l_2 \sim \sqrt{L/k}, \quad \text{(Fresnel zone size)}, \tag{2}$$

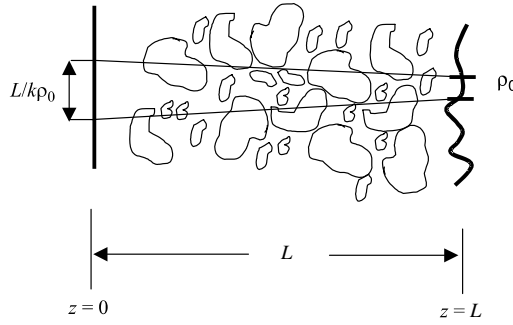$$l_3 \sim L/k\rho_0, \quad \text{(scattering disk)}.$$

Figure 9.2 Schematic illustrating the relation of the scattering disk at $z = 0$ to the coherence cell size at $z = L$.

Under weak irradiance fluctuations it is known that the Fresnel zone l_2 defines the dominant scale size for scintillation, but the propagating wave is still sensitive to all scale sizes within the inertial range. In this regime the Fresnel zone is smaller than the transverse spatial coherence radius l_1 but larger than l_1 in strong fluctuations. As the optical wave propagates into regimes of stronger irradiance fluctuations, it is influenced less and less by eddy sizes near the Fresnel zone scale. Instead, two dominant scale sizes are evident in the scintillation pattern that lead to the behavior illustrated in Fig. 9.2—the smaller scale is on the order of the spatial coherence radius whereas the larger scale is on the order of the scattering disk. A "scattering disk" in both weak and strong fluctuations is defined by the refractive cell size l at which the focusing angle $\theta_F \sim l/L$ is equal to the average scattering angle θ_D. Under weak fluctuations the scattering angle is roughly $\theta_D \sim \lambda/\sqrt{L/k} \sim 1/\sqrt{Lk}$, so the size of the scattering disk is on the order of the first Fresnel zone l_2. Under strong fluctuations, we find $\theta_D \sim \lambda/\rho_0 \sim 1/k\rho_0$ (recall Fig. 5.3), and consequently, the scattering disk is defined by l_3. Therefore, the field within the coherence cell area of size ρ_0 at distance L from the transmitter under strong fluctuations is assumed to originate from the scattering disk area of size $L/k\rho_0$ near the transmitter as illustrated in Fig. 9.2. Only eddy sizes *equal to or larger than $L/k\rho_0$* can contribute to the field within the coherence cell size ρ_0.

As the optical wave propagates, there is a gradual transition from the Fresnel scale as the most critical cell size for scintillation to the spatial coherence radius and the scattering disk. That is, as the Fresnel zone scale approaches the size of the coherence radius at the onset of strong fluctuations (focusing regime), all three cell sizes (2) are roughly equal ($l_1 \sim l_2 \sim l_3$). For yet stronger fluctuation conditions, the focusing effect is weakened, and the spatial coherence radius is smaller than the Fresnel zone whereas the scattering disk is larger. We illustrate the relative cell sizes $l_1, l_2,$ and l_3 in Fig. 9.3 for a propagating plane wave.

9.2.2 Spatial filter functions

It has long been recognized that cell sizes bounded below by the spatial coherence radius and above by the scattering disk radius contribute little to scintillation under
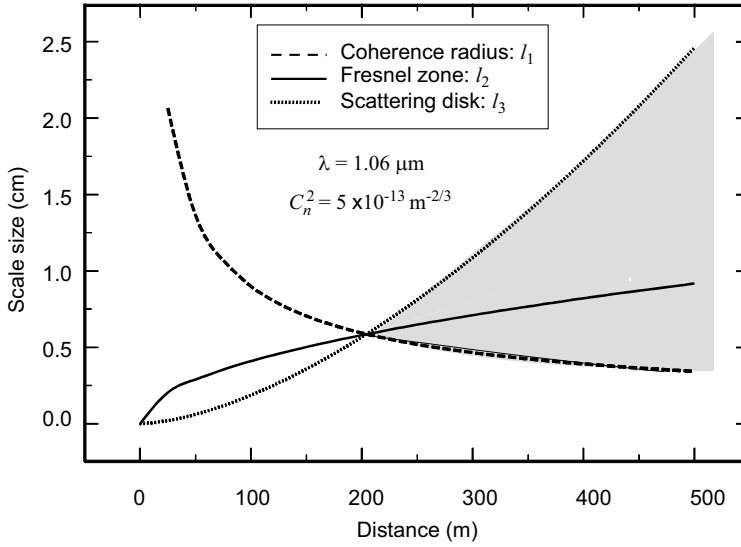
Figure 9.3   Relative turbulent scale sizes defined by l_1, l_2, and l_3 in Eq. (2) vs. propagation distance for an infinite plane wave. The shaded area denotes excluded scale sizes under strong fluctuations.

strong fluctuations [7−9]. This particular range of cell sizes is portrayed by the shaded region in Fig. 9.3. To construct an atmospheric spectrum model for scintillation that characterizes this behavior of the various cell sizes, we introduce a technique similar to that used in adaptive optics methods whereby we modify the conventional Kolmogorov power-law spectrum with a spatial filter. By also including the effects from the inner scale and outer scale, this leads to the so-called *effective atmospheric spectrum*

$$\Phi_{n,e}(\kappa) = \Phi_n(\kappa)G(\kappa, l_0, L_0) = 0.033C_n^2\kappa^{-11/3}G(\kappa, l_0, L_0), \tag{3}$$

where l_0 is the inner scale, L_0 is the outer scale, and $G(\kappa, l_0, L_0)$ is an amplitude *spatial filter*.

The notion of an "effective atmospheric spectrum" like (3) is actually a direct consequence of introducing the "effective index of refraction" composed of only large-scale and small-scale components as first discussed in Section 5.9. Thus, the spatial filter appearing in Eq. (3) must eliminate the impact of the ineffective scale sizes on scintillation under strong fluctuation conditions. For horizontal paths in which C_n^2 is essentially constant, we represent such a spatial filter by

$$G(\kappa, l_0, L_0) \equiv G_X(\kappa, l_0, L_0) + G_Y(\kappa, l_0)$$

$$= f(\kappa l_0)g(\kappa L_0)\exp\left(-\frac{\kappa^2}{\kappa_X^2}\right) + \frac{\kappa^{11/3}}{(\kappa^2 + \kappa_Y^2)^{11/6}}, \tag{4}$$

where $f(\kappa l_0)$ is a factor that describes inner scale modifications of the basic Kolmogorov power law, $g(\kappa L_0)$ describes outer scale effects, κ_X is a large-scale (or refractive) spatial frequency cutoff, and κ_Y is a small-scale (or diffractive) spatial frequency cutoff. Thus, the filter function $G(\kappa, l_0, L_0)$ only permits low-pass spatial frequencies $\kappa < \kappa_X$ and high-pass frequencies $\kappa > \kappa_Y$ at a given propagation distance L. The inner-scale factor $f(\kappa l_0)$ plays an important role in the large-scale filter $G_X(\kappa, l_0, L_0)$ because the inner scale affects the spatial coherence radius ρ_0 and, hence, also the scattering disk $L/k\rho_0$. We have not explicitly included the inner-scale factor $f(\kappa l_0)$ in the small-scale filter $G_Y(\kappa, l_0)$, but inner scale effects are included through the spatial frequency cutoff κ_Y. And, like filter functions in general, the actual mathematical forms given in (4) are not critical—these particular mathematical forms are chosen on the basis of mathematical tractability. Other filter shapes may produce essentially the same numerical results for the scintillation index as those in (4).

In the absence of inner scale effects, we take $f(\kappa l_0) = 1$, and when the inner scale must be taken into account, we assume

$$f(\kappa l_0) = \exp\left(-\kappa^2/\kappa_l^2\right)\left[1 + 1.802(\kappa/\kappa_l) - 0.254(\kappa/\kappa_l)^{7/6}\right], \quad \kappa_l = 3.3/l_0, \quad (5)$$

which includes the characteristic rise in the spectrum at high wave numbers just prior to the dissipation range [see Eq. (22) in Chap. 3]. Under weak fluctuations it is widely accepted that the scintillation index of a plane wave or spherical wave is not greatly influenced by the outer scale of turbulence L_0; however, when a propagating optical wave experiences stronger conditions of optical turbulence the role of the outer scale on scintillation is less clear. Along horizontal paths near the ground the outer scale is typically on the order of Kh, where h denotes height above ground and K is a constant on the order of unity. In this case the outer scale imposes a strict limitation on the size of the largest eddies that can focus a less coherent beam. That is, isotropic turbulent cells larger than the outer scale do not actually exist and the energy spectrum must necessarily fall off at lower wave numbers approaching $1/L_0$. Thus, the large-scale scintillation under strong fluctuations will be reduced by this natural filtering process. In our modeling of outer scale effects, we assume

$$g(\kappa L_0) = 1 - \exp\left(-\kappa^2/\kappa_0^2\right), \quad (6)$$

where $\kappa_0 = 8\pi/L_0$.[1] The functional form (6) is commonly used in place of the von Kármán spectrum for introducing outer scale effects. Once again, it is chosen here on the basis of mathematical tractability.

9.2.3 Scintillation index model

Based on the form of the extended Rytov theory as described by the modulation process given in Eq. (1), it is clear that the resulting irradiance of the field can

---

[1]Note that the scaling constant 8π of the outer scale wave number κ_0 used here is not the same as that assumed in the von Kármán spectrum or modified atmospheric spectrum.

also be expressed as some form of product which, for mathematical reasons, we choose to write in normalized form as

$$\hat{I} = \frac{I}{\langle I \rangle} = XY. \tag{7}$$

Here we assume X arises from large-scale turbulent eddy effects and Y from *statistically independent* small-scale eddy effects. The notion of one random process modulating another as depicted in Eq. (7) is an old idea that is fundamental in many diverse areas of application [31–33]. In some cases the modulation process may be described as a *nonstationary process* [31,32], e.g., the mean value may act like a random variable. In other cases it may be described as a *multiply stochastic process* [33]. The basic concept in all these cases usually involves the "mean" of one distribution being "smeared" by another distribution. The case important to us involves a scattering medium (i.e., the atmosphere) that treats the instantaneous light source that passes through it as a modulation process.

The scintillation theory that we present below follows directly from the form suggested by Eq. (7). In particular, based on (7) the second moment of irradiance (regardless of the assumed distributions for X and Y) can be written as

$$\begin{aligned} \langle \hat{I}^2 \rangle &= \langle X^2 \rangle \langle Y^2 \rangle \\ &= (1 + \sigma_X^2)(1 + \sigma_Y^2), \end{aligned} \tag{8}$$

where we are assuming that X and Y have unit means, i.e., $\langle X \rangle = \langle Y \rangle = 1$, and that σ_X^2 and σ_Y^2 are normalized variances of X and Y, respectively. From Eq. (8), the implied scintillation index is found to be a sum of three terms involving the normalized variances of large-scale and small-scale irradiance fluctuations, viz.,

$$\begin{aligned} \sigma_I^2 &= (1 + \sigma_X^2)(1 + \sigma_Y^2) - 1 \\ &= \sigma_X^2 + \sigma_Y^2 + \sigma_X^2 \sigma_Y^2. \end{aligned} \tag{9}$$

Under the Rytov approximation, the *log amplitude* of an optical wave is related to the irradiance of the random field by $\chi = (1/2) \ln (I/A_0^2)$. The relation between the log-amplitude variance and the scintillation index is given by (see Problem 18 in Chap. 5)

$$\sigma_I^2 = \exp(4\sigma_\chi^2) - 1 = \exp(\sigma_{\ln I}^2) - 1, \quad \sigma_\chi^2 \ll 1, \tag{10}$$

where $\sigma_{\ln I}^2 = 4\sigma_\chi^2$ is the variance of *log irradiance*. Similarly, we assume that large- and small-scale scintillations can be defined by

$$\begin{aligned} \sigma_X^2 &= \exp(\sigma_{\ln X}^2) - 1, \\ \sigma_Y^2 &= \exp(\sigma_{\ln Y}^2) - 1, \end{aligned} \tag{11}$$

where $\sigma_{\ln X}^2$ and $\sigma_{\ln Y}^2$ are called large- and small-scale log-irradiance variances, respectively. Consequently, the total scintillation index then takes the form

$$\sigma_I^2 = \exp(\sigma_{\ln I}^2) - 1 = \exp(\sigma_{\ln X}^2 + \sigma_{\ln Y}^2) - 1. \tag{12}$$

The quantity $\sigma_{\ln I}^2 = \sigma_{\ln X}^2 + \sigma_{\ln Y}^2$ is equivalent to the conventional variance of log irradiance only under weak irradiance fluctuations ($\sigma_{\ln I}^2 \ll 1$), and in this case Eqs. (11) and (12) yield the results $\sigma_X^2 \cong \sigma_{\ln X}^2$, $\sigma_Y^2 \cong \sigma_{\ln Y}^2$, and $\sigma_I^2 \cong \sigma_{\ln I}^2 = \sigma_{\ln X}^2 + \sigma_{\ln Y}^2$.

9.3   Asymptotic Theory

The method we develop in this chapter for the scintillation index makes use of known expressions for both the weak and strong fluctuation regimes. We developed expressions in Chap. 8 for weak fluctuations, and here we develop expressions for the saturation regime based on the *asymptotic theory* [12–14, 34,35].

9.3.1   Plane waves and spherical waves

In the saturation regime, the scintillation index for an unbounded plane wave or spherical wave based on a Kolmogorov spectrum can be expressed as

$$\sigma_I^2(L) = 1 + 32\pi^2 k^2 L \int_0^1 \int_0^\infty \kappa \Phi_n(\kappa) \sin^2\left[\frac{L\kappa^2}{2k} w(\xi, \xi)\right]$$

$$\times \exp\left\{-\int_0^1 D_S\left[\frac{L\kappa}{k} w(\tau, \xi)\right] d\tau\right\} d\kappa \, d\xi, \quad \sigma_R^2 \gg 1, \tag{13}$$

where τ is a normalized distance variable and the exponential function acts like a low-pass spatial filter defined by the plane wave structure function of phase $D_S(\rho)$ [see Eq. (66) in Chap. 6]. The function $w(\tau, \xi)$ is defined by

$$w(\tau, \xi) = \begin{cases} \tau(1 - \overline{\Theta}\xi), & \tau < \xi, \\ \xi(1 - \overline{\Theta}\tau), & \tau > \xi, \end{cases} \tag{14}$$

where $\overline{\Theta} = 1 - \Theta = 0$ for a plane wave and $\overline{\Theta} = 1$ for a spherical wave.

The low-pass spatial filter in (13) ensures that $L\kappa^2/k \ll 1$, which represents a *geometrical optics approximation*.[2] If we first consider the plane wave case ($\overline{\Theta} = 0$) under the assumption that the inner scale of turbulence is smaller than the spatial coherence radius of the optical wave, then based on a Kolmogorov spectrum with $D_S(\rho) = 2.91 C_n^2 k^2 L \rho^{5/3}$, it follows that

$$\int_0^1 D_S\left[\frac{L\kappa}{k} w(\tau, \xi)\right] d\tau = 2.37 \sigma_R^2 \left(\frac{L}{k}\right)^{5/6} \kappa^{5/3} \xi^{5/3}\left(1 - \frac{5}{8}\xi\right). \tag{15}$$

---

[2]The geometrical optics approximation means that diffraction effects are negligible. It is generally characterized by the limiting case in which wavelength $\lambda \to 0$.

Also, the sine function in Eq. (13) may be approximated by its leading term, which yields

$$\sin^2\left(\frac{L\kappa^2\xi}{2k}\right) \cong \frac{L^2\kappa^4\xi^2}{4k^2} \tag{16}$$

and, consequently, Eq. (13) leads to

$$\sigma_{I,\mathrm{pl}}^2(L) = 1 + 2.12\sigma_R^2\left(\frac{L}{k}\right)^{7/6}\int_0^1 \xi^2 \int_0^\infty \kappa^{4/3}$$

$$\times \exp\left[-2.37\sigma_R^2\left(\frac{L}{k}\right)^{5/6}\kappa^{5/3}\xi^{5/3}\left(1-\frac{5}{8}\xi\right)\right]d\kappa\,d\xi \tag{17}$$

$$= 1 + \frac{0.34}{\sigma_R^{4/5}}\int_0^1 \frac{\xi^{-1/3}}{\left(1-\frac{5}{8}\xi\right)^{7/5}}\,d\xi, \quad \sigma_R^2 \gg 1.$$

By completing the remaining integration in (17), we find in the *plane wave* case that

$$\sigma_{I,\mathrm{pl}}^2(L) = 1 + \frac{0.86}{\sigma_R^{4/5}}, \quad \sigma_R^2 \gg 1. \tag{18}$$

Under a similar analysis for a *spherical wave* ($\overline{\Theta} = 1$), it can be shown that

$$\sigma_{I,\mathrm{sp}}^2(L) = 1 + \frac{2.73}{\sigma_R^{4/5}}, \quad \sigma_R^2 \gg 1. \tag{19}$$

9.3.2 Gaussian-beam waves

By following the asymptotic analysis for plane waves and spherical waves provided in Sec. 9.3.1, we first express the *on-axis scintillation index* for a Gaussian-beam wave in the saturation regime in the form

$$\sigma_I^2(0,L) = 1 + 32\pi^2 k^2 L \int_0^1 \int_0^\infty \kappa\Phi_n(\kappa)\sin^2\left[\frac{L\kappa^2}{2k}\xi(1-\overline{\Theta}\xi)\right]$$

$$\times \exp\left(-\frac{\Lambda L\kappa^2\xi^2}{k}\right)\exp\left\{-\int_0^1 D_S\left[\frac{L\kappa}{k}w(\tau,\xi)\right]d\tau\right\}d\kappa\,d\xi, \quad \sigma_R^2 \gg 1, \tag{20}$$

where $D_S(\rho)$ is the *plane wave structure function of phase* and the parameter $w(\tau,\xi)$ is defined by Eq. (14). However, for a Gaussian-beam wave the parameter $\overline{\Theta}$ assumes values between zero and unity, except for a focused beam, which we generally exclude in this analysis.

Under the geometrical optics approximation ($L\kappa^2/k \ll 1$), the phase structure function can be approximated by the wave structure function. In this case, we also find that

$$\sin^2\left[\frac{L\kappa^2}{2k}\xi(1-\overline{\Theta}\xi)\right] \cong \frac{L^2\kappa^4}{4k^2}\xi^2(1-\overline{\Theta}\xi)^2, \ \ \exp\left(-\frac{\Lambda L\kappa^2\xi^2}{k}\right) \cong 1. \tag{21}$$

The first approximation in (21) is the same as that leading to (16). Physically, the second result in (21) expresses the fact that the size of the optical wave in the saturation regime is so large that the longitudinal component of the scintillation index behaves like that of a large-diameter wave with uniform amplitude (e.g., a spherical wave). To more clearly see this, we note that (21) implies

$$\frac{\Lambda L\kappa^2}{k} \sim \left(\frac{L\kappa}{kW}\right)^2 \ll 1.$$

Hence, for any size beam in which $\kappa \ll kW/L$, the GOM can be invoked.

In the case where the inner scale of turbulence is smaller than the spatial coherence radius of the optical wave, i.e., $l_0 < \rho_0$, we parallel the plane wave analysis and base our calculations on the conventional Kolmogorov spectrum for which the phase structure function is $D_S(\rho) = 2.91C_n^2 k^2 L\rho^{5/3}$. Thus, in this case Eq. (20) reduces to the functional form [29]

$$\sigma_I^2(0, L) = 1 + \frac{1.33\overline{\Theta}^{7/5}}{\sigma_R^{4/5}}\int_0^1 \frac{(1-\overline{\Theta}\xi)^2}{\xi^{1/3}\left[(1-\overline{\Theta}\xi)^{5/3}-(1-\overline{\Theta})^{8/3}\right]^{7/5}}d\xi$$

$$= 1 + \frac{C(\overline{\Theta})}{\sigma_R^{4/5}}, \quad \sigma_R^2 \gg 1. \tag{22}$$

An exact form for $C(\overline{\Theta})$ is unknown, but it can be closely approximated by a quadratic polynomial in $\overline{\Theta}$. Nonetheless, for our purposes it suffices to approximate it by a simple linear function that leads to the result

$$\sigma_I^2(0, L) = 1 + \frac{0.86 + 1.87\overline{\Theta}}{\sigma_R^{4/5}}, \quad \sigma_R^2 \gg 1. \tag{23}$$

Expressions for the plane wave and spherical wave cases (18) and (19) are readily deduced from (23) by setting $\overline{\Theta} = 0$ and $\overline{\Theta} = 1$, respectively.

When inner scale effects must be taken into account, it has been shown that the longitudinal component leads to the more general result [29]

$$\sigma_I^2(0, L) = 1 + \frac{2.39 + 5.26\overline{\Theta}}{\left(\sigma_R^2 Q_l^{7/6}\right)^{1/6}}, \quad \sigma_R^2 Q_l^{7/6} \gg 100, \tag{24}$$

where $Q_l = 10.89L/kl_0^2$. Comparable results for the plane wave and spherical wave cases can be deduced from (24) by setting $\overline{\Theta} = 0$ and $\overline{\Theta} = 1$, respectively.

9.4   Scintillation Theory: Plane Wave Model

Under the Rytov approximation, the log-irradiance variance for an infinite plane wave is defined by (see Chap. 8)

$$\sigma_{\ln I, \, \text{pl}}^2(L) = 8\pi^2 k^2 \int_0^L \int_0^\infty \kappa \Phi_n(\kappa) \left[1 - \cos\left(\frac{\kappa^2 z}{k} \right) \right] d\kappa \, dz. \qquad (25)$$

Based on the Kolmogorov power-law spectrum and the change of parameters $\xi = z/L$ and $\eta = L\kappa^2/k$, Eq. (25) takes the simpler form

$$\sigma_{\ln I, \, \text{pl}}^2(L) = 1.06\sigma_R^2 \int_0^1 \int_0^\infty \eta^{-11/6}(1 - \cos \eta\xi) \, d\eta \, d\xi. \qquad (26)$$

Performing the integration in (26) and using the relation $\sigma_I^2 \cong \sigma_{\ln I}^2, \sigma_R^2 \ll 1$, we obtain the well-known weak fluctuation result (see Chap. 8)

$$\sigma_{I, \, \text{pl}}^2(L) \cong \sigma_{\ln I, \, \text{pl}}^2(L) = \sigma_R^2, \quad \sigma_R^2 \ll 1. \qquad (27)$$

At the other extreme, the asymptotic theory predicts that the scintillation index in the saturation regime is described by Eq. (18). Our approach here is to derive an expression for the scintillation index that reduces to (27) under weak irradiance fluctuations and approaches (18) under strong fluctuations.

9.4.1   Zero inner scale model

For the case in which both inner scale and outer scale effects can be ignored, we use the *effective power spectrum* defined by Eqs. (9) and (10) with $f(\kappa l_0) = g(\kappa L_0) = 1$. Thus, if we invoke the extended Rytov theory suggested by Eq. (1), then the scintillation index can be expressed in the form

$$\sigma_I^2(L) = \exp(\sigma_{\ln X}^2 + \sigma_{\ln Y}^2) - 1, \qquad (28)$$

where $\sigma_{\ln X}^2$ and $\sigma_{\ln Y}^2$ are large-scale and small-scale log-irradiance scintillations defined, respectively, by

$$\sigma_{\ln X}^2 = 8\pi^2 k^2 \int_0^L \int_0^\infty \kappa \Phi_n(\kappa) G_X(\kappa) \left[1 - \cos\left(\frac{\kappa^2 z}{k} \right) \right] d\kappa \, dz, \qquad (29)$$

$$\sigma_{\ln Y}^2 = 8\pi^2 k^2 \int_0^L \int_0^\infty \kappa \Phi_n(\kappa) G_Y(\kappa) \left[1 - \cos\left(\frac{\kappa^2 z}{k} \right) \right] d\kappa \, dz. \qquad (30)$$

The large scale and small scale filter functions appearing in (29) and (30) are defined, respectively, by

$$G_X(\kappa) = \exp\left(-\frac{\kappa^2}{\kappa_X^2} \right), \qquad (31)$$

$$G_Y(\kappa) = \frac{\kappa^{11/3}}{\left(\kappa^2 + \kappa_Y^2\right)^{11/6}}. \tag{32}$$

The quantities κ_X and κ_Y represent cutoff spatial frequencies that eliminate mid range scale size effects under moderate-to-strong fluctuations (see Fig. 9.3).

Because the low-pass and high-pass spatial frequency cutoffs appearing in the filter functions (31) and (32) are directly related to the correlation width and scattering disk of the propagating optical wave, we assume at any distance L into the random medium there exists an effective scattering disk L/kl_X and an effective correlation width l_Y related, respectively, to the cutoff wave numbers according to

$$\frac{L}{kl_X} = \frac{1}{\kappa_X} \sim \begin{cases} \sqrt{L/k}, & \sigma_R^2 \ll 1, \\ L/k\rho_0, & \sigma_R^2 \gg 1, \end{cases} \tag{33}$$

$$l_Y = \frac{1}{\kappa_Y} \sim \begin{cases} \sqrt{L/k}, & \sigma_R^2 \ll 1, \\ \rho_0, & \sigma_R^2 \gg 1. \end{cases} \tag{34}$$

In the development of a scintillation model below we select the cutoff frequencies κ_X and κ_Y on the basis of the assumed asymptotic behavior in (33) and (34) as well as established behavior of the scintillation index in these asymptotic regimes provided by Eqs. (18) and (27). In particular, in weak and strong fluctuation regimes, the assumed scintillation index (28) reduces to

$$\sigma_I^2(L) \cong \begin{cases} \sigma_{\ln X}^2 + \sigma_{\ln Y}^2, & \sigma_R^2 \ll 1 \\ 1 + 2\sigma_{\ln X}^2, & \sigma_R^2 \gg 1, \end{cases} \tag{35}$$

where the second expression in (35) is based on the limiting value $\sigma_Y^2 = \exp(\sigma_{\ln Y}^2) - 1 \to 1$, or $\sigma_{\ln Y}^2 \to \ln 2$ in the saturation regime. Thus, we need to determine the large scale and small scale log irradiances so that

$$\sigma_{\ln X}^2 + \sigma_{\ln Y}^2 = \sigma_R^2, \quad \sigma_R^2 \ll 1,$$
$$\sigma_{\ln X}^2 = \frac{0.43}{\sigma_R^{4/5}}, \quad \sigma_R^2 \gg 1. \tag{36}$$

For the large-scale log irradiance (29) we can use the geometrical optics approximation, which in this case corresponds to

$$1 - \cos\left(\frac{\kappa^2 z}{k}\right) \cong \frac{1}{2}\left(\frac{\kappa^2 z}{k}\right)^2, \quad \kappa \ll \kappa_X. \tag{37}$$

Consequently, by using the approximation (37) and again introducing the parameter changes $\xi = z/L$ and $\eta = L\kappa^2/k$, the large-scale log-irradiance variance reduces to

$$\sigma_{\ln X}^2 = 8\pi^2 k^2 \int_0^L \int_0^\infty \kappa \Phi_n(\kappa) G_X(\kappa) \left[1 - \cos\left(\frac{\kappa^2 z}{k}\right) \right] d\kappa\, dz$$

$$\cong 0.53\sigma_R^2 \int_0^1 \xi^2 d\xi \int_0^\infty \eta^{1/6} \exp\left(-\eta/\eta_X\right) d\eta \tag{38}$$

$$\cong 0.16\sigma_R^2 \eta_X^{7/6},$$

where $\eta_X = L\kappa_X^2/k$. To determine the cutoff wave number κ_X, we use the asymptotic results (33) and (34) according to

$$\frac{1}{\kappa_X^2} = \frac{c_1 L}{k} + c_2 \left(\frac{L}{k\rho_0}\right)^2 = \frac{0.38L}{k} + 0.35\left(\frac{L}{k\rho_0}\right)^2. \tag{39}$$

The scaling constants c_1 and c_2 appearing in (39) are deduced from the asymptotic behavior given by (35) and (36). Specifically, under weak fluctuations we tacitly make the assumption that large scale effects account for roughly half of the total scintillation index in (36). From the result (39), it follows that

$$\eta_X = \frac{L\kappa_X^2}{k} = \frac{1}{0.38 + 0.35L/k\rho_0^2} = \frac{2.61}{1 + 1.11\sigma_R^{12/5}}, \tag{40}$$

and hence, the large-scale log-irradiance variance (29) can be written as[3]

$$\sigma_{\ln X}^2 = \frac{0.49\sigma_R^2}{\left(1 + 1.11\sigma_R^{12/5}\right)^{7/6}} \sim \begin{cases} 0.49\sigma_R^2, & \sigma_R^2 \ll 1, \\ \dfrac{0.43}{\sigma_R^{4/5}}, & \sigma_R^2 \gg 1. \end{cases} \tag{41}$$

In the small-scale log-irradiance variance (30), we use the approximation

$$\int_0^L \int_0^\infty \frac{\kappa}{\left(\kappa^2 + \kappa_Y^2\right)^{11/6}} \left[1 - \cos\left(\frac{\kappa^2 z}{k}\right) \right] d\kappa\, dz$$

$$\cong \int_0^L \int_0^\infty \frac{\kappa}{\left(\kappa^2 + \kappa_Y^2\right)^{11/6}} d\kappa\, dz, \quad \kappa_Y \gg \sqrt{k/L}. \tag{42}$$

That is, at high wave numbers ($\kappa > \kappa_Y \gg \sqrt{k/L}$) the integral of the cosine term in (42) with respect to z yields the form $(\sin \eta)/\eta$ which, for large $\eta = L\kappa^2/k$, tends to zero. Hence, using (42) the small-scale log-irradiance scintillation (30) leads to

$$\sigma_{\ln Y}^2 = 8\pi^2 k^2 \int_0^L \int_0^\infty \kappa \Phi_n(\kappa) G_Y(\kappa) \left[1 - \cos\left(\frac{\kappa^2 z}{k}\right) \right] d\kappa\, dz$$

$$\cong 1.06\sigma_R^2 \int_0^\infty (\eta + \eta_Y)^{-11/6} d\eta \tag{43}$$

$$\cong 1.27\sigma_R^2 \eta_Y^{-5/6},$$

---

[3]Choosing the scaling constants in (39) so that $\sigma_{\ln X}^2 \cong 0.49\sigma_R^2$ in the weak fluctuation limit in (41) is somewhat arbitrary, not necessarily an optimum choice.

where $\eta_Y = L\kappa_Y^2/k$. Similar to the large-scale case, here it has been shown that

$$\kappa_Y^2 = \frac{c_3 k}{L} + \frac{c_4}{\rho_0^2} = \frac{3k}{L} + \frac{1.7}{\rho_0^2}, \tag{44}$$

$$\eta_Y = \frac{L\kappa_Y^2}{k} = 3 + \frac{1.7L}{k\rho_0^2} = 3\left(1 + 0.69\sigma_R^{12/5}\right), \tag{45}$$

and thus, Eq. (43) becomes

$$\sigma_{\ln Y}^2 = \frac{0.51\sigma_R^2}{\left(1 + 0.69\sigma_R^{12/5}\right)^{5/6}} \sim \begin{cases} 0.51\sigma_R^2, & \sigma_R^2 \ll 1, \\ \ln 2, & \sigma_R^2 \gg 1. \end{cases} \tag{46}$$

By combining (41) and (46), we see that the scintillation index (28) for a plane wave in the absence of inner scale and outer scale effects is given by

$$\sigma_{I,\mathrm{pl}}^2(L) = \exp\left[\frac{0.49\sigma_R^2}{\left(1 + 1.11\sigma_R^{12/5}\right)^{7/6}} + \frac{0.51\sigma_R^2}{\left(1 + 0.69\sigma_R^{12/5}\right)^{5/6}}\right] - 1, \quad 0 \le \sigma_R^2 < \infty. \tag{47}$$

Equation (47) is our general result for the case of negligible inner scale and infinite outer scale, and is considered valid for all values of the Rytov variance σ_R^2. That is, although (38) and (43) were derived by use of the approximations (37) and (42), which are strictly valid only under strong irradiance fluctuations for which $\eta_X \ll 1$ and $\eta_Y \gg 1$, we defined the normalized filter cutoff wave numbers (40) and (45) in such a way that (47) reduces to the correct result under weak and strong irradiance fluctuations.

In Fig. 9.4 we show separate plots of the large-scale (solid line) and small-scale (dashed line) fluctuations σ_X^2 and σ_Y^2 versus the strength-of-turbulence parameter σ_R for a propagating plane wave. Note that only in the large-scale fluctuations does there appear to be a focusing regime (where scintillation first reaches a peak value before decreasing), which occurs near $\sigma_R = 1$. For increasing values of σ_R, small-scale fluctuations increase monotonically toward a limiting value of unity; moreover, small-scale fluctuations clearly dominate large-scale fluctuations for $\sigma_R > 1$. In Fig. 9.5 we show the combined effects of large- and small-scale fluctuations on the predicted scintillation index of a plane wave given by Eq. (47). Again, we plot scintillation as a function of strength-of-turbulence parameter σ_R. Lastly, for the sake of comparison, the dashed curves in Fig. 9.5 are based on (i) the asymptotic behavior (27) under weak irradiance fluctuations and (ii) the asymptotic theory approximation (18) for strong irradiance fluctuations. In both limiting cases the general model (47) compares well with the established asymptotic behavior for $\sigma_R < 1$ and $\sigma_R > 6$.
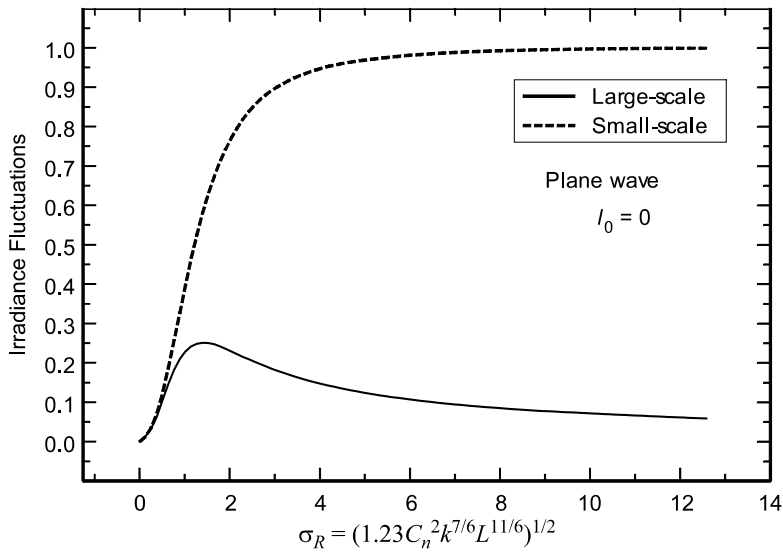
Figure 9.4 Large- and small-scale irradiance fluctuations vs. strength-of-turbulence. Inner scale/outer scale effects are not included.

9.4.2 Inner scale and outer scale effects

When inner scale and outer scale effects are taken into account, we use the spectrum model described by Eqs. (3)–(6) to deduce large-scale and small-scale scintillation.
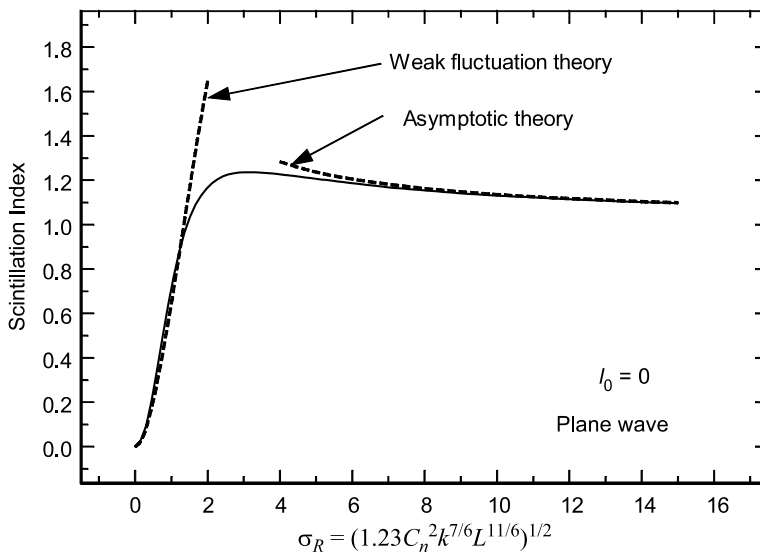

Figure 9.5 Scintillation index of a plane wave vs. strength-of-turbulence. Inner scale/outer scale effects are not included.

Under weak irradiance fluctuations, the plane wave scintillation index based on the modified atmospheric spectrum [Eq. (22) in Chap. 3] is closely approximated by the quantity [36]

$$
\sigma_{PL}^2 = 3.86\sigma_R^2 \left\{ (1 + 1/Q_l^2)^{11/12} \left[\sin\left(\frac{11}{6} \tan^{-1} Q_l \right) \right. \right.
$$

$$
+ \frac{1.51}{(1 + Q_l^2)^{1/4}} \sin\left(\frac{4}{3} \tan^{-1} Q_l \right)
$$

$$
\left. \left. - \frac{0.27}{(1 + Q_l^2)^{7/24}} \sin\left(\frac{5}{4} \tan^{-1} Q_l \right) \right] - \frac{3.50}{Q_l^{5/6}} \right\}, \quad \sigma_R^2 < 1, \qquad (48)
$$

where $Q_l = 10.89 L/k l_0^2$. In the saturation regime, the expression deduced from (24) is

$$
\sigma_{I,\,\mathrm{pl}}^2(L) = 1 + \frac{2.39}{(\sigma_R^2 Q_l^{7/6})^{1/6}}, \quad \sigma_R^2 Q_l^{7/6} \gg 100. \qquad (49)
$$

The large scale filter function in the present case takes the form

$$
G_X(\kappa, l_0, L_0) = f(\kappa l_0) \left[\exp\left(-\frac{\kappa^2}{\kappa_X^2} \right) - \exp\left(-\frac{\kappa^2}{\kappa_{X0}^2} \right) \right], \qquad (50)
$$

where $f(\kappa l_0)$ is defined by (5) and $\kappa_{X0}^2 = \kappa_X^2 \kappa_0^2/(\kappa_X^2 + \kappa_0^2)$. Hence, it follows that the large-scale scintillation can be expressed as a difference, viz.,

$$
\sigma_{\ln X}^2(l_0, L_0) = \sigma_{\ln X}^2(l_0) - \sigma_{\ln X}^2(L_0). \qquad (51)
$$

The first term on the right-hand side in (51) is given by

$$
\sigma_{\ln X}^2(l_0) = 1.06\sigma_R^2 \int_0^1 \int_0^\infty \eta^{-11/6} \exp\left(-\eta/Q_l - \eta/\eta_X \right)
$$

$$
\times \left[1 + 1.80(\eta/Q_l)^{1/2} - 0.25(\eta/Q_l)^{7/12} \right] (1 - \cos \eta\xi) \, d\eta \, d\xi
$$

$$
\cong 0.53\sigma_R^2 \int_0^1 \xi^2 d\xi \int_0^\infty \eta^{1/6} \exp\left(-\eta/Q_l - \eta/\eta_X \right)
$$

$$
\times \left[1 + 1.80(\eta/Q_l)^{1/2} - 0.25(\eta/Q_l)^{7/12} \right] d\eta, \qquad (52)
$$

where we have used a geometrical optics approximation in the second step. Upon evaluation of this last expression, we obtain

$$
\sigma_{\ln X}^2(l_0) = 0.16\sigma_R^2 \left(\frac{\eta_X Q_l}{\eta_X + Q_l} \right)^{7/6} \left[1 + 1.75\left(\frac{\eta_X}{\eta_X + Q_l} \right)^{1/2} - 0.25\left(\frac{\eta_X}{\eta_X + Q_l} \right)^{7/12} \right].
$$

$$
(53)
$$

Under moderate-to-strong irradiance fluctuations we can approximate the non-dimensional quantity η_X in (53) by an expression similar to that used in the zero inner scale case; that is,

$$\eta_X = \frac{1}{0.38 + 0.17L/k\rho_0^2} = \frac{2.61}{1 + 0.45\sigma_R^2 Q_l^{1/6}}, \tag{54}$$

where $L/k\rho_0^2 = 1.02\sigma_1^2 Q_l^{1/6}$ in the case $\rho_0 \ll l_0$. Thus, by inserting (54) into (53), we find that the large-scale log-irradiance scintillation with inner scale parameter can be written in the form

$$\sigma_{\ln X}^2(l_0) = 0.16\sigma_R^2 \left(\frac{2.61Q_l}{2.61 + Q_l + 0.45\sigma_R^2 Q_l^{7/6}}\right)^{7/6}$$

$$\times \left[1 + 1.75\left(\frac{2.61}{2.61 + Q_l + 0.45\sigma_R^2 Q_l^{7/6}}\right)^{1/2}\right.$$

$$\left. - 0.25\left(\frac{2.61}{2.61 + Q_l + 0.45\sigma_R^2 Q_l^{7/6}}\right)^{7/12}\right]. \tag{55}$$

By an entirely analogous evaluation, it follows that the large-scale log-irradiance scintillation with outer scale parameter becomes[4]

$$\sigma_{\ln X}^2(L_0) = 0.16\sigma_R^2 \left(\frac{\eta_{X0} Q_l}{\eta_{X0} + Q_l}\right)^{7/6} \left[1 + 1.75\left(\frac{\eta_{X0}}{\eta_{X0} + Q_l}\right)^{1/2}\right.$$

$$\left. - 0.25\left(\frac{\eta_{X0}}{\eta_{X0} + Q_l}\right)^{7/12}\right], \tag{56}$$

where

$$\eta_{X0} = \frac{\eta_X Q_0}{\eta_X + Q_0} = \frac{2.61Q_0}{2.61 + Q_0 + 0.45\sigma_R^2 Q_0 Q_l^{1/6}}, \tag{57}$$

and where $Q_0 = L\kappa_0^2/k = 64\pi^2 L/kL_0^2$.

Because the form of the filter function is the same for the small-scale log-irradiance scintillations in this case as that for the zero inner scale case, these scintillations are again described by

$$\sigma_{\ln Y}^2(l_0) \cong 1.27\sigma_R^2 \eta_Y^{-5/6}. \tag{58}$$

However, in weak fluctuations we impose $\sigma_{\ln Y}^2(l_0) \sim 0.51\sigma_{PL}^2$, so that the parameter η_Y now depends on the inner scale according to $\eta_Y \sim 3(\sigma_R^2/\sigma_{PL}^2)^{6/5}$. Inner scale effects tend to diminish under strong fluctuations such that

---

[4]Note that although we refer to (56) as an "outer scale term," it also has a dependency on the inner scale as indicated in both (56) and (57).

$\eta_Y \sim 2.07\sigma_R^{12/5}, \sigma_R^2 \gg 1$, in agreement with Eq. (45). Thus, we assume

$$\begin{aligned}\eta_Y &= 3(\sigma_R/\sigma_{PL})^{12/5} + 2.07\sigma_R^{12/5} \\ &= 3(\sigma_R/\sigma_{PL})^{12/5}\left(1 + 0.69\sigma_{PL}^{12/5}\right),\end{aligned} \tag{59}$$

and Eq. (58) becomes

$$\sigma_{\ln Y}^2(l_0) = \frac{0.51\sigma_{PL}^2}{\left(1 + 0.69\sigma_{PL}^{12/5}\right)^{5/6}}. \tag{60}$$

We note here that although the small-scale filter (32) does not explicitly contain an inner scale factor like the large-scale filter (50), the cutoff spatial frequency κ_Y for the small-scale filter does depend on the inner scale [see (59)] and, hence, small-scale scintillation described by (60) also depends on the inner scale, particularly in the weak fluctuation regime. Outer-scale effects are negligible here. Finally, by combining (55), (56), and (60), the scintillation index for an infinite plane wave in the presence of a finite (nonzero) inner scale and a finite outer scale is

$$\sigma_{I,\mathrm{pl}}^2(L) = \exp\left[\sigma_{\ln X}^2(l_0) - \sigma_{\ln X}^2(L_0) + \frac{0.51\sigma_{PL}^2}{(1 + 0.69\sigma_{PL}^{12/5})^{5/6}}\right] - 1, \quad 0 \le \sigma_R^2 < \infty. \tag{61}$$

The influence of the inner scale and outer scale on plane wave scintillation is shown in Fig. 9.6. The dashed curves are based on Eq. (61) with $L_0 = \infty$ and
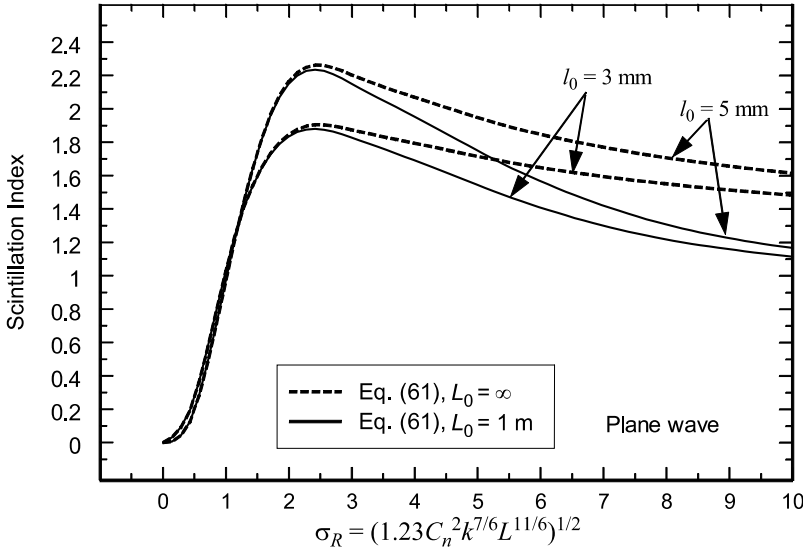

Figure 9.6 Plane wave scintillation index vs. σ_R for outer scale $L_0 = \infty$ (dashed lines) and $L_0 = 1$ m (solid lines). Inner scale values of 3 mm and 5 mm are included in each outer scale case.

inner scale values $l_0 = 3$ mm and $l_0 = 5$ mm, illustrating the effect of the inner scale alone on scintillation. The solid curves are for the same inner-scale values but with $L_0 = 1$ m, typical of the outer scale for horizontal path propagation near the ground. Note in Fig. 9.6 that the outer scale has a negligible effect on scintillation under weak fluctuations ($\sigma_R < 1$), consistent with conventional weak fluctuation theory (see Chap. 8). However, from the vicinity of the focusing regime where $\sigma_R > 2$, the presence of a finite outer scale in the scintillation model is quite clear. Namely, the outer-scale effect initially reduces scintillation at a steeper rate toward its limiting value of unity than would occur with an infinite outer scale (dashed lines). Outer-scale values satisfying $L_0 < 1$ can lead to an even more pronounced outer-scale effect in the scintillation index.

9.5 Scintillation Theory: Spherical Wave Model

Our treatment of the scintillation theory for a spherical wave will mostly parallel the development in Section 9.4 for the infinite plane wave. Under weak fluctuation theory, the log-irradiance variance is defined by

$$\sigma_{\ln I, \text{sp}}^2(L) = 8\pi^2 k^2 \int_0^L \int_0^\infty \kappa \Phi_n(\kappa) \left\{ 1 - \cos\left[\frac{\kappa^2}{k} z\left(1 - \frac{z}{L}\right)\right]\right\} d\kappa \, dz, \qquad (62)$$

which, based on a Kolmogorov power-law spectrum, leads to

$$\sigma_{I, \text{sp}}^2(L) \cong \sigma_{\ln I, \text{sp}}^2(L) = 0.4\sigma_R^2, \quad \sigma_R^2 \ll 1. \qquad (63)$$

It is customary in some analyses to introduce the *spherical wave Rytov variance* β_0^2, related to the plane wave parameter according to

$$\beta_0^2 = 0.4\sigma_R^2. \qquad (64)$$

Like the plane wave case, the spherical wave Rytov variance is simply the weak fluctuation scintillation index of a spherical wave based on a conventional Kolmogorov power-law spectrum.

9.5.1 Zero inner scale model

We begin our treatment for the special case in which the inner scale is zero and the outer scale is infinite. The large- and small-scale log-irradiance variances are defined, respectively, by

$$\sigma_{\ln X}^2 = 8\pi^2 k^2 \int_0^L \int_0^\infty \kappa \Phi_n(\kappa) G_X(\kappa) \left\{ 1 - \cos\left[\frac{\kappa^2 z(1 - z/L)}{k}\right]\right\} d\kappa \, dz, \qquad (65)$$

$$\sigma_{\ln Y}^2 = 8\pi^2 k^2 \int_0^L \int_0^\infty \kappa \Phi_n(\kappa) G_Y(\kappa) \left\{ 1 - \cos\left[\frac{\kappa^2 z(1 - z/L)}{k}\right]\right\} d\kappa \, dz, \qquad (66)$$

where the filter functions have the same form as given in (31) and (32).

To evaluate (65), we use the geometrical optics approximation to get

$$
\begin{aligned}
\sigma_{\ln X}^2 &= 8\pi^2 k^2 \int_0^L \int_0^\infty \kappa \Phi_n(\kappa) G_X(\kappa) \left\{ 1 - \cos\left[\frac{\kappa^2 z(1 - z/L)}{k}\right] \right\} d\kappa\, dz \\
&\cong 0.53 \sigma_R^2 \int_0^1 \xi^2 (1 - \xi)^2 d\xi \int_0^\infty \eta^{1/6} \exp(-\eta/\eta_X)\, d\eta \\
&\cong 0.016 \sigma_R^2 \eta_X^{7/6},
\end{aligned}
\tag{67}
$$

where, for a spherical wave,

$$
\eta_X = \frac{L\kappa_X^2}{k} = \frac{8.56}{1 + 0.19\sigma_R^{12/5}},
\tag{68}
$$

and where we have used the relation $L/k\rho_0^2 = 1.22\sigma_R^{12/5}$. Hence, the large-scale log-irradiance variance can be written as

$$
\sigma_{\ln X}^2 = \frac{0.20\sigma_R^2}{(1 + 0.19\sigma_R^{12/5})^{7/6}} \sim \begin{cases} 0.20\sigma_R^2, & \sigma_R^2 \ll 1, \\ \dfrac{1.37}{\sigma_R^{4/5}}, & \sigma_R^2 \gg 1. \end{cases}
\tag{69}
$$

In the development of the small-scale log-irradiance variance, we are led to

$$
\begin{aligned}
\sigma_{\ln Y}^2 &= 8\pi^2 k^2 \int_0^L \int_0^\infty \kappa \Phi_n(\kappa) G_Y(\kappa) \left\{ 1 - \cos\left[\frac{\kappa^2 z(1 - z/L)}{k}\right] \right\} d\kappa\, dz \\
&\cong 1.06 \sigma_R^2 \int_0^\infty (\eta + \eta_Y)^{-11/6} d\eta \\
&\cong 1.27 \sigma_R^2 \eta_Y^{-5/6},
\end{aligned}
\tag{70}
$$

where

$$
\eta_Y = \frac{L\kappa_Y^2}{k} = 9(1 + 0.23\sigma_R^{12/5}).
\tag{71}
$$

Thus, Eq. (70) becomes

$$
\sigma_{\ln Y}^2 = \frac{0.20\sigma_R^2}{\left(1 + 0.23\sigma_R^{12/5}\right)^{5/6}} \sim \begin{cases} 0.20\sigma_R^2, & \sigma_R^2 \ll 1, \\ \ln 2, & \sigma_R^2 \gg 1. \end{cases}
\tag{72}
$$

Now, by combining (69) and (72), the scintillation index is given by

$$
\sigma_{I,\,\mathrm{sp}}^2(L) = \exp\left[\frac{0.20\sigma_R^2}{\left(1 + 0.19\sigma_R^{12/5}\right)^{7/6}} + \frac{0.20\sigma_R^2}{\left(1 + 0.23\sigma_R^{12/5}\right)^{5/6}} \right] - 1,
$$
$$
0 \leq \sigma_R^2 < \infty. \tag{73}
$$

In Fig. 9.7 we plot the scintillation index (73) as a function of the strength-of-turbulence parameter σ_R. For comparison, we also plot the corresponding
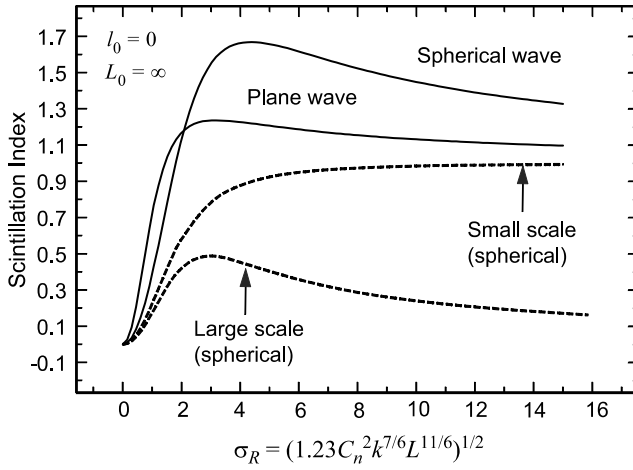
Figure 9.7 The solid curves depict the scintillation index for the plane wave and spherical wave models in the absence of inner scale and/or outer scale effects. The dashed curves are the large- and small-scale scintillation for the spherical wave model.

scintillation index of a plane wave (47). Whereas peak scintillation for the plane wave model occurs near $\sigma_R = 2$, peak scintillation for the spherical wave model occurs near $\sigma_R = 4$. The dashed curves are the large-scale and small-scale scintillation of a spherical wave.

Last, in terms of the spherical wave Rytov variance $\beta_0^2 = 0.4\sigma_R^2$, Eq. (73) becomes

$$\sigma_{I,\,sp}^2(L) = \exp\left[\frac{0.49\beta_0^2}{\left(1 + 0.56\beta_0^{12/5}\right)^{7/6}} + \frac{0.51\beta_0^2}{\left(1 + 0.69\beta_0^{12/5}\right)^{5/6}} \right] - 1,$$

$$0 \le \beta_0^2 < \infty. \quad (74)$$

Equation (74) using Rytov variance β_0^2 more clearly emphasizes the numerical similarity in the coefficients to the plane wave model (47) using Rytov variance σ_R^2.

9.5.2 Inner scale and outer scale effects

Under weak irradiance fluctuations, the scintillation index based on the modified atmospheric spectrum leads to the approximation [36]

$$\sigma_{SP}^2 \cong 9.65\beta_0^2\left\{ 0.40(1 + 9/Q_l^2)^{11/12}\left[\sin\left(\frac{11}{6}\tan^{-1}\frac{Q_l}{3} \right) \right.\right.$$

$$+ \frac{2.61}{(9 + Q_l^2)^{1/4}}\sin\left(\frac{4}{3}\tan^{-1}\frac{Q_l}{3} \right)$$

$$\left.\left. - \frac{0.52}{(9 + Q_l^2)^{7/24}}\sin\left(\frac{5}{4}\tan^{-1}\frac{Q_l}{3} \right) \right] - \frac{3.50}{Q_l^{5/6}} \right\}, \quad \beta_0^2 < 1, \quad (75)$$

where $Q_l = 10.89L/kl_0^2$. In the saturation regime, the corresponding approximation to the scintillation index deduced from (24) is

$$\sigma_I^2(L) = 1 + \frac{7.65}{\left(\beta_0^2 Q_l^{7/6}\right)^{1/6}}, \quad \beta_0^2 Q_l^{7/6} \gg 100. \tag{76}$$

As in the plane wave case, we assume the large-scale filter function is (50), which contains both inner scale and outer scale parameters. Under the geometrical optics approximation, the large-scale scintillation due to inner scale alone is described by the log-irradiance variance

$$\begin{aligned}
\sigma_{\ln X}^2(l_0) &= 2.65\beta_0^2 \int_0^1 \int_0^\infty \eta^{-11/6} \exp\left(-\eta/Q_l - \eta/\eta_X\right) \\
&\quad \times \left[1 + 1.80(\eta/Q_l)^{1/2} - 0.25(\eta/Q_l)^{7/12}\right] \\
&\quad \times \left\{1 - \cos\left[\eta\xi(1-\xi)\right]\right\}d\eta\, d\xi \\
&\cong 1.33\beta_0^2 \int_0^1 \xi^2(1-\xi)^2 d\xi \int_0^\infty \eta^{1/6} \exp\left(-\eta/Q_l - \eta/\eta_X\right) \\
&\quad \times \left[1 + 1.80(\eta/Q_l)^{1/2} - 0.25(\eta/Q_l)^{7/12}\right]d\eta.
\end{aligned} \tag{77}$$

Completing the integration, this last expression simplifies to

$$\begin{aligned}
\sigma_{\ln X}^2(l_0) &= 0.04\beta_0^2 \left(\frac{8.56Q_l}{8.56 + Q_l + 0.20\beta_0^2 Q_l^{7/6}}\right)^{7/6} \\
&\quad \times \left[1 + 1.75\left(\frac{8.56}{8.56 + Q_l + 0.20\beta_0^2 Q_l^{7/6}}\right)^{1/2}\right. \\
&\quad \left. - 0.25\left(\frac{8.56}{8.56 + Q_l + 0.20\beta_0^2 Q_l^{7/6}}\right)^{7/12}\right].
\end{aligned} \tag{78}$$

where we have used

$$\eta_X = \frac{8.56}{1 + 0.08L/k\rho_0^2} = \frac{8.56}{1 + 0.20\beta_0^2 Q_l^{1/6}}. \tag{79}$$

Similarly, the large-scale scintillation due to outer scale effects is described by

$$\sigma_{\ln X}^2(L_0) = 0.04\beta_0^2 \left[\frac{8.56 Q_0 Q_l}{8.56(Q_0 + Q_l) + Q_0 Q_l \left(1 + 0.20\beta_0^2 Q_l^{1/6}\right)} \right]^{7/6}$$

$$\times \left\{ 1 + 1.75 \left[\frac{8.56 Q_0}{8.56(Q_0 + Q_l) + Q_0 Q_l \left(1 + 0.20\beta_0^2 Q_l^{1/6}\right)} \right]^{1/2} \right.$$

$$\left. - 0.25 \left[\frac{8.56 Q_0}{8.56(Q_0 + Q_l) + Q_0 Q_l \left(1 + 0.20\beta_0^2 Q_l^{1/6}\right)} \right]^{7/12} \right\}. \qquad (80)$$

The small-scale log-irradiance variance is once again given by (70), where

$$\eta_Y = 9(\beta_0/\sigma_{SP})^{12/5} \left(1 + 0.69\sigma_{SP}^{12/5}\right), \qquad (81)$$

and where we have used $\sigma_R^2 = 2.5\beta_0^2$. Hence, the small-scale log-irradiance becomes

$$\sigma_{\ln Y}^2(l_0) = \frac{0.51\sigma_{SP}^2}{\left(1 + 0.69\sigma_{SP}^{12/5}\right)^{5/6}}, \qquad (82)$$

and if we combine (78), (80), and (82), we obtain the scintillation index for a spherical wave in the presence of a finite inner scale and outer scale given by

$$\sigma_{I,\,sp}^2(L) = \exp\left[\sigma_{\ln X}^2(l_0) - \sigma_{\ln X}^2(L_0) + \frac{0.51\sigma_{SP}^2}{\left(1 + 0.69\sigma_{SP}^{12/5}\right)^{5/6}} \right] - 1. \qquad (83)$$

In Fig. 9.8 we plot the scintillation index (83) as a function of the Rytov parameter $\beta_0 = (0.5 C_n^2 k^{7/6} L^{11/6})^{1/2}$, with $L_0 = \infty$ and several values of inner scale l_0. The fixed parameters in β_0 are $\lambda = 2\pi/k = 0.488\,\mu m$ and $C_n^2 = 5 \times 10^{-13}\,m^{-2/3}$. Thus, changes in β_0 are caused by allowing the propagation distance L to vary. We note that the spherical wave is quite sensitive to the inner scale, leading to a scintillation index reaching around 6 and higher near the peak. Similar scintillation values associated with inner-scale sizes in the range of 8–10 mm, however, are consistent with measured data [18]. The presence of a finite outer scale will cause a steeper decline in scintillation beyond the focusing regime as illustrated in Fig. 9.6 for an infinite plane wave.

The curves shown in Fig. 9.8 should not be interpreted as universal curves for a given value of inner scale l_0 and given β_0. Changes in wavelength λ, propagation distance L, or structure constant C_n^2 can produce different values of the scintillation index for the same inner-scale value and same β_0. That is, propagation conditions with fixed propagation path length and wavelength, but variable C_n^2, lead to somewhat different scintillation values than conditions with fixed C_n^2 and propagation distance, but changing wavelength.
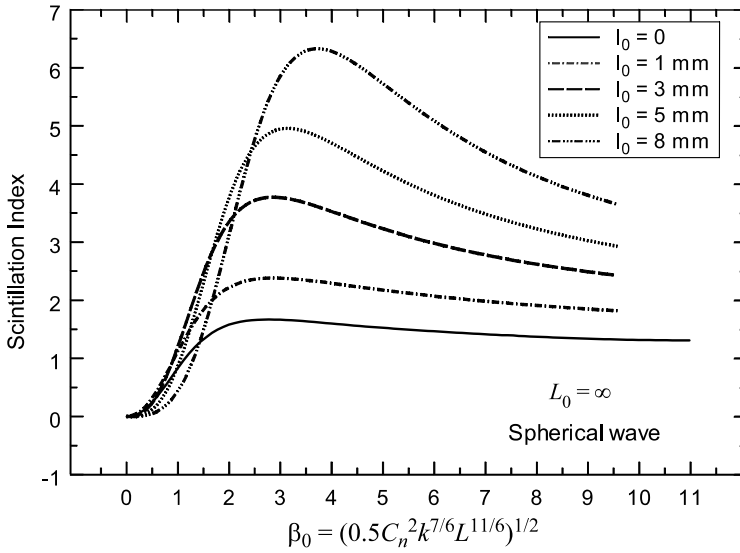
Figure 9.8 The scintillation index of a spherical wave vs. β_0 and several inner-scale values for $\lambda = 0.488\ \mu$m, $C_n^2 = 5 \times 10^{-3}\ \text{m}^{-2/3}$, and variable distance L. The outer scale $L_0 = \infty$.

9.5.3 Comparison with experimental data

In 1993, Consortini et al. [18] published results of simultaneous measurements of scintillation, inner scale, and refractive-index structure parameter associated with a spherical wave propagating along a horizontal 1200-m path. Measured values of C_n^2 varied from 10^{-15} to $10^{-12}\ \text{m}^{-2/3}$ and the inner scale ranged from around 2.5 to 12 mm. The transmitter was an argon-ion laser operating at 0.488 μm and the diverged beam was directed into the atmosphere at a height of approximately 1.2 m above the ground. The structure parameter for each run was inferred from measured data taken on a 600-m path over the last half of the total propagation path, and the inner scale was deduced from a separate measurement over a 150-m path directly in front of the receiver.

Some of the data from the experiment [18] were plotted for a number of intervals of the inner scale. Two such data sets are replotted in Figs. 9.9 and 9.10 (open circles) for inner-scale values $3\ \text{mm} < l_0 < 4\ \text{mm}$ and $5\ \text{mm} < l_0 < 6\ \text{mm}$, typical of many near-ground horizontal propagation paths. Theoretical values (dashed lines) predicted by Eq. (83) with $L_0 \gg 1$ are shown for $l_0 = 3$ and 4 mm in Fig. 9.9 and for $l_0 = 5$ and 6 mm in Fig. 9.10. Also shown in Figs. 9.9 and 9.10 by the solid curves are theoretical values generated from Eq. (83) with outer scale $L_0 = 0.6$ m, corresponding to half the height of the laser source above the ground. Here we clearly see the impact of a finite outer scale for data in which $\beta_0 > 4$. Although there is considerable scatter in the strong scintillation data in both figures, the theoretical curves taken from (83) with $L_0 = 0.6$ m do pass through the middle portion of the data, whereas those with $L_0 \gg 1$ do not! Vertical
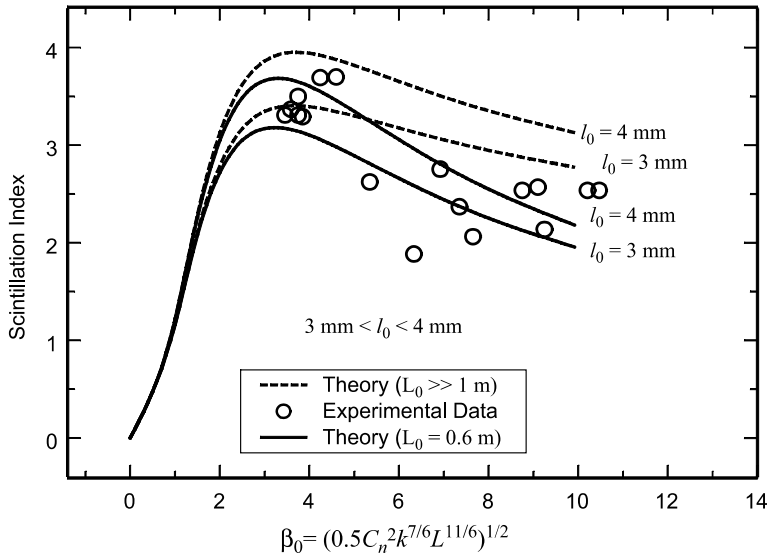
Figure 9.9 Open circles represent scintillation data for a fixed propagation distance of 1200 m taken from Ref. [18] and replotted here for inner-scale values ranging in size between 3 and 4 mm. Dashed curves are based on the scintillation theory with $L_0 = \infty$ and the solid curves represent $L_0 = 0.6$ m.

scatter in the data can generally be attributed to changes in inner scale l_0, whereas horizontal shifting of the data corresponds to changes in C_n^2.

In Fig. 9.11 we show results from the asymptotic theory (76) for inner scale values $l_0 = 3$ mm and $l_0 = 6$ mm along with the experimental data taken from
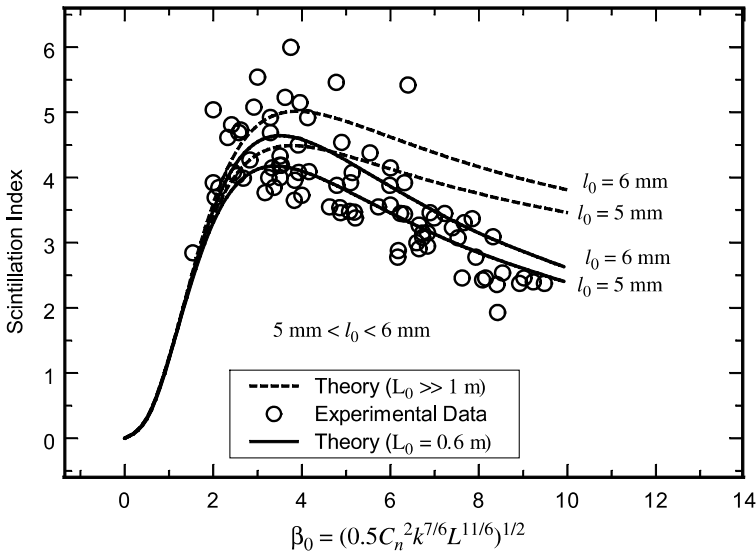

Figure 9.10 Same as Fig. 9.9 except inner scale values range in size between 5 and 6 mm.
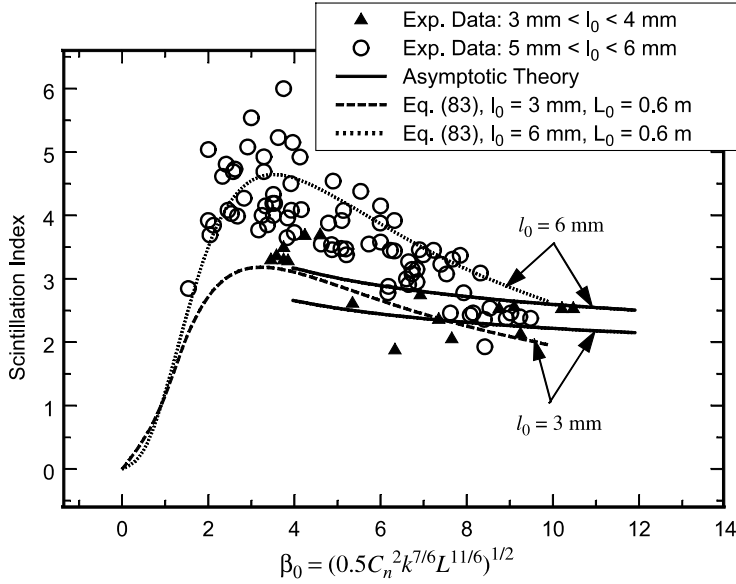
Figure 9.11 Scintillation index (solid lines) as predicted by the asymptotic theory (76) vs. β_0. Open circles and filled triangles are experimental data taken from Ref. [18]. Also shown are theoretical curves from (83) for $l_0 = 3$ mm, $l_0 = 6$ mm, and $L_0 = 0.6$ m.

Figs. 9.9 and 9.10. For contrast, we also show theoretical curves obtained from (83) for $l_0 = 3$ mm, $l_0 = 6$ mm, and $L_0 = 0.6$ m. Here we can see that the asymptotic theory does not agree well with the data. A modification of (76) to include the outer scale can be readily deduced from the scintillation model (83) in the saturation regime, which leads to

$$\sigma_{I,\,\text{sp}}^2(L) \cong 1 + 2\sigma_{\ln X}^2(l_0) - 2\sigma_{\ln X}^2(L_0), \quad \beta_0^2 \gg 1. \tag{84}$$

Even with the outer-scale term in (84), it still does not provide a good approximation to the data except for $\beta_0 > 8$. In developing the scintillation model (83), the asymptotic theory result (76) was used primarily as an aid for selecting the large-scale spatial cutoff wave number κ_X in strong fluctuation regimes.

A failure of the asymptotic theory to correctly match data for large values of β_0 was previously pointed out by others [14,25]. In particular, Flatté and Gerber [25] compared Eq. (76) with simulation results for a spherical wave and various values of inner scale and found that the power-law indices in (76) do not match the behavior of the simulation results. Part of the failure of the asymptotic theory can be attributed to the fact that the theory does not account for outer-scale effects that are important in near-ground propagation. However, even including outer-scale effects, as in (84), the resulting asymptotic theory still has strict limitations and may be applicable only far into the saturation regime.

9.6 Scintillation Theory: Gaussian-Beam Wave Model

In this section we will present expressions for the scintillation index of a Gaussian-beam wave comparable to the results given in Sections 9.4 and 9.5 for the plane wave and spherical wave models. In the case of a beam wave, however, there is also a radial component and beam wander effects that we must separately treat.

9.6.1 Radial component

In developing an expression for the radial component under strong irradiance fluctuations, we will rely largely on the approach of Miller et al. [37−39] using the notion of effective beam parameters.

Effective beam parameters were introduced in Chap. 7 to account for additional diffraction effects on the wave structure function (WSF) and the spatial coherence radius. These parameters are [see Eqs. (40) in Section 7.4.1]

$$\Theta_e = 1 + \frac{L}{F_{\mathrm{LT}}} = \frac{\Theta - 0.81\sigma_R^{12/5}\Lambda}{1 + 1.63\sigma_R^{12/5}\Lambda}, \quad \overline{\Theta}_e = 1 - \Theta_e, \tag{85}$$

$$\Lambda_e = \frac{2L}{kW_{\mathrm{LT}}^2} = \frac{\Lambda}{1 + 1.63\sigma_R^{12/5}\Lambda}. \tag{86}$$

Neglecting beam wander effects, the radial component of scintillation vanishes on the optical axis ($r = 0$) and, in *weak fluctuations* using a Kolmogorov power-law spectrum, is closely approximated by the radial log variance [see Eqs. (18) and (22) in Section 8.2], i.e.,

$$\sigma_{I,r}^2(\mathbf{r}, L) \cong 4.42\sigma_R^2 \Lambda^{5/6} \frac{r^2}{W^2}, \qquad r < W, \qquad \sigma_R^2 < 1, \tag{87}$$

where W is the free-space spot radius of the beam at the receiver. In strong fluctuations we expect the radial component of the scintillation to eventually diminish as the beam propagates into the saturation regime except, possibly, at large radial distances from the optical axis ($r \gg W$).

A finite diameter optical wave propagating through large-scale inhomogeneities will experience random deflections as it propagates, called *beam wander* (see Sections 6.6 and 8.3). As a result, the "short-term" spot size will wander randomly in the plane of the receiver, painting out a larger beam called the "long-term" spot size W_{LT}. The free-space beam spot size W is characterized by the free-space parameter $\Lambda = 2L/kW^2$. However, the long-term spot size caused essentially by large-scale-induced beam wander is characterized by the effective beam parameter $\Lambda_e = 2L/kW_{\mathrm{LT}}^2$. Thus, we will follow the work of Miller et al. [38] and tacitly replace the beam parameter Λ with the effective beam parameter Λ_e in the radial component which, based on Eq. (87), yields

$$\sigma_{I,r}^2(\mathbf{r}, L) \cong 4.42\sigma_R^2\Lambda_e^{5/6}\frac{r^2}{W_{\text{LT}}^2}, \quad 0 \le r < W. \tag{88}$$

However, in the presence of beam wander effects leading to what is an effective pointing error σ_{pe}, the radial component (88) must be adjusted in accordance with the tracked and untracked models developed in Section 8.3. The *variance of pointing error* is

$$\sigma_{pe}^2 = 7.25C_n^2L^3W_0^{-1/3}\int_0^1 \xi^2\left\{\frac{1}{|\Theta_0 + \overline{\Theta}_0\xi|^{1/3}} - \left[\frac{\kappa_r^2W_0^2}{1 + \kappa_r^2W_0^2(\Theta_0 + \overline{\Theta}_0\xi)^2}\right]^{1/6}\right\}d\xi, \tag{89}$$

where $\kappa_r = 2\pi/r_0$, and r_0 is the atmospheric coherence width. Hence, the radial component for untracked and tracked (nonfocused) beams under weak-to-strong irradiance fluctuations leads to

$$\sigma_{I,r}^2(\mathbf{r}, L)_{\text{untracked}} \cong 4.42\sigma_R^2\Lambda_e^{5/6}\left(\frac{r - \sigma_{pe}}{W_{\text{LT}}}\right)^2, \quad \sigma_{pe} \le r < W, \tag{90}$$

$$\sigma_{I,r}^2(\mathbf{r}, L)_{\text{tracked}} \cong 4.42\sigma_R^2\Lambda_e^{5/6}\left(\frac{r - \sqrt{\langle r_c^2\rangle}}{W_{\text{LT}}}\right)^2, \quad \sqrt{\langle r_c^2\rangle} \le r < W, \tag{91}$$

where $\langle r_c^2\rangle$ is the variance of beam wander displacements (see Chap. 7).

Under weak fluctuations, the effective beam parameter Λ_e reduces to Λ and, consequently, (90) and (91) reduce to expressions given in Chap. 8. However, we pointed out in Chap. 8 that there is little distinction in the on-axis scintillation between an untracked propagating collimated beam and that based on first-order Rytov theory. The same is also true under stronger conditions of irradiance fluctuations. Moreover, the radial component (90) for the untracked beam is essentially the same as (88) based on first-order Rytov theory (i.e., when $\sigma_{pe} = 0$). For that reason, we will ignore beam wander effects in the general results presented after Section 9.6.2, and we will not further address the tracked beam case.

When the inner scale is included in the analysis it tends to increase scintillation levels in the radial component, but such effects are relatively weak and can often be ignored. Outer-scale effects, on the other hand, can be quite strong and tend to reduce the overall scintillation level off axis [36,38]. The outer scale effect on the radial component is introduced in Section 9.6.3.

9.6.2 Zero inner scale model

In weak fluctuation regimes where inner-scale and outer scale effects are negligible, we base our calculations on the conventional Kolmogorov spectrum. By use of this spectrum model and the nondimensional quantities $\xi = 1 - z/L$ and

$\eta = L\kappa^2/k$, the longitudinal component of the scintillation index becomes the *Rytov variance for a beam wave* (see Section 8.3.2)

$$\sigma_B^2 = 3.86\sigma_R^2\text{Re}\left[i^{5/6}{}_2F_1\left(-\frac{5}{6}, \frac{11}{6}; \frac{17}{6}; \overline{\Theta} + i\Lambda\right) - \frac{11}{16}\Lambda^{5/6}\right],$$
$$\sigma_R \ll 1, \quad (92)$$

where Re denotes the real part and ${}_2F_1(a, b; c; x)$ is a hypergeometric function [40]. For a collimated or divergent beam, however, the Rytov variance (92) can be approximated by the simpler expression [see Eq. (23) in Chap. 8]

$$\sigma_B^2 \cong 3.86\sigma_R^2\left\{0.40\big[(1 + 2\Theta)^2 + 4\Lambda^2\big]^{5/12}\right.$$

$$\left. \times \cos\left[\frac{5}{6}\tan^{-1}\left(\frac{1 + 2\Theta}{2\Lambda}\right)\right] - \frac{11}{16}\Lambda^{5/6}\right\}. \quad (93)$$

In terms of the large-scale filter function (31), the large-scale log-irradiance variance for a beam wave is defined by

$$\sigma_{\ln X}^2 = 1.06\sigma_R^2 \int_0^1 \int_0^\infty \eta^{-11/6} \exp\left(-\frac{\eta}{\eta_X}\right) \exp(-\Lambda\eta\xi^2)$$

$$\times \left\{1 - \cos\big[\eta\xi(1 - \overline{\Theta}\xi)\big]\right\} d\eta \, d\xi, \quad (94)$$

which, under the geometrical optics approximation, reduces to

$$\sigma_{\ln X}^2 \cong 0.53\sigma_R^2 \int_0^1 \xi^2(1 - \overline{\Theta}\xi)^2 \int_0^\infty \eta^{1/6} \exp\left(-\eta/\eta_X\right) d\eta \, d\xi$$

$$\cong 0.49\left(\frac{1}{3} - \frac{1}{2}\overline{\Theta} + \frac{1}{5}\overline{\Theta}^2\right)\sigma_R^2\eta_X^{7/6}, \quad (95)$$

where

$$\frac{1}{\eta_X} = \left(\frac{1}{3} - \frac{1}{2}\overline{\Theta} + \frac{1}{5}\overline{\Theta}^2\right)^{6/7}\left(\frac{\sigma_R}{\sigma_B}\right)^{12/7} + 1.12\left(\frac{\frac{1}{3} - \frac{1}{2}\overline{\Theta} + \frac{1}{5}\overline{\Theta}^2}{1 + 2.17\overline{\Theta}}\right)^{6/7}\sigma_R^{12/5}$$

$$\cong \left(\frac{1}{3} - \frac{1}{2}\overline{\Theta} + \frac{1}{5}\overline{\Theta}^2\right)^{6/7}\left(\frac{\sigma_R}{\sigma_B}\right)^{12/7}[1 + 0.56(1 + \Theta)\sigma_B^{12/5}]. \quad (96)$$

In arriving at (95) and (96), we have relied on the asymptotic behavior given by (23) and (92) and have also used the approximation $1.12/(1 + 2.17\overline{\Theta})^{6/7} \cong 0.56(1 + \Theta)(\sigma_B/\sigma_R)^{24/35}$. (Note that, to account for larger beams, (96) is a minor variation of the approximation used in Refs. [29] and [30].) By substituting (96) into (95), we find

$$\sigma_{\ln X}^2 = \frac{0.49\sigma_B^2}{\left[1 + 0.56(1 + \Theta)\sigma_B^{12/5}\right]^{7/6}}. \tag{97}$$

For the small-scale filter function, we use a small modification of (32), viz.,

$$G_Y(\kappa, z) = \frac{\kappa^{11/3}}{(\kappa^2 + \kappa_Y^2)^{11/6}} \exp\left[\frac{\Lambda L \kappa^2 (1 - z/L)^2}{k}\right], \quad \kappa_Y \gg 1, \tag{98}$$

where κ_Y is the high-pass spatial frequency cutoff. To justify (98), we argue that effects from the finite size of a beam wave at the transmitter diminish over sufficiently long propagation paths owing to a combination of diffraction effects and optical turbulence—i.e., the beam wave appears to act more like a spherical wave over long propagation paths. Therefore, the small-scale filter should contain a factor that depends on propagation distance z and which essentially eliminates the finite beam character from the analysis. In this case, the small-scale log-irradiance fluctuations lead to

$$\sigma_{\ln Y}^2 \cong 1.06\sigma_R^2 \int_0^1 \int_0^\infty \left(\eta + \eta_Y\right)^{-11/6} d\eta \, d\xi \tag{99}$$

$$\cong 1.27\sigma_R^2 \eta_Y^{-5/6},$$

where the exponential function in the filter has canceled that in the beam wave expression. Thus, Eq. (99) has the same mathematical form as previously found for the plane wave and spherical wave models. Here, we define

$$\eta_Y = \frac{L\kappa_Y^2}{k} = 3\left(\frac{\sigma_R}{\sigma_B}\right)^{12/5} + 2.07\sigma_R^{12/5}, \tag{100}$$

and thus, (99) gives us

$$\sigma_{\ln Y}^2 = \frac{0.51\sigma_B^2}{\left(1 + 0.69\sigma_B^{12/5}\right)^{5/6}}. \tag{101}$$

The combined results of Eqs. (97) and (101) yield the longitudinal component

$$\sigma_{I,l}^2(L) = \exp\left\{\frac{0.49\sigma_B^2}{\left[1 + 0.56(1 + \Theta)\sigma_B^{12/5}\right]^{7/6}} + \frac{0.51\sigma_B^2}{\left(1 + 0.69\sigma_B^{12/5}\right)^{5/6}}\right\} - 1. \tag{102}$$

Note that the functional form of the scintillation index (102) is virtually the same as that for the spherical wave described by (74). If we account for beam wander

effects for the untracked beam case, we find that the combined components of the scintillation index at off-axis points is described by

$$\sigma_I^2(\mathbf{r}, L)_{\text{untracked}} = \exp\left\{\frac{0.49\sigma_B^2}{\left[1 + 0.56(1 + \Theta)\sigma_B^{12/5}\right]^{7/6}} + \frac{0.51\sigma_B^2}{(1 + 0.69\sigma_B^{12/5})^{5/6}}\right\} - 1$$

$$+ 4.42\sigma_R^2\Lambda_e^{5/6}\left(\frac{\sigma_{pe}}{W_{\text{LT}}}\right)^2 + 4.42\sigma_R^2\Lambda_e^{5/6}\left(\frac{r - \sigma_{pe}}{W_{\text{LT}}}\right)^2,$$

$$\sigma_{pe} \leq r < W. \qquad (103)$$

However, as mentioned above, there is virtually no difference in (103) and that obtained by setting $\sigma_{pe} = 0$ in the case of collimated or divergent beams. To account for a tracked beam, we simply drop the first term in the second line in (103), replace $r - \sigma_{pe}$ by $r - \sqrt{\langle r_c^2\rangle}$, and impose the restriction $r > \sqrt{\langle r_c^2\rangle}$.

Equation (103) represents our approximation to the scintillation index at any transverse position in the beam at the receiver plane ($\sigma_{pe} \leq r < W$) of a Gaussian-beam wave under all irradiance fluctuation conditions. We plot the on-axis scintillation index (102) as a function of σ_R in Fig. 9.12 along with previous results for the plane wave and spherical wave cases. The illustrated Gaussian-beam wave is assumed collimated at the transmitter with spot size radius $W_0 = 1$ cm, the structure constant C_n^2 is assumed fixed, and the propagation distance is allowed to vary. In Fig. 9.13 we plot both on- and off-axis results deduced from (103) under the same conditions cited for Fig. 9.12. We note that radial dependency of the scintillation index is virtually eliminated once the beam has passed the focusing regime (location of peak scintillation). However, the somewhat abrupt change in the shape of the curve for $r = W$ and $1 < \sigma_R < 2$ is
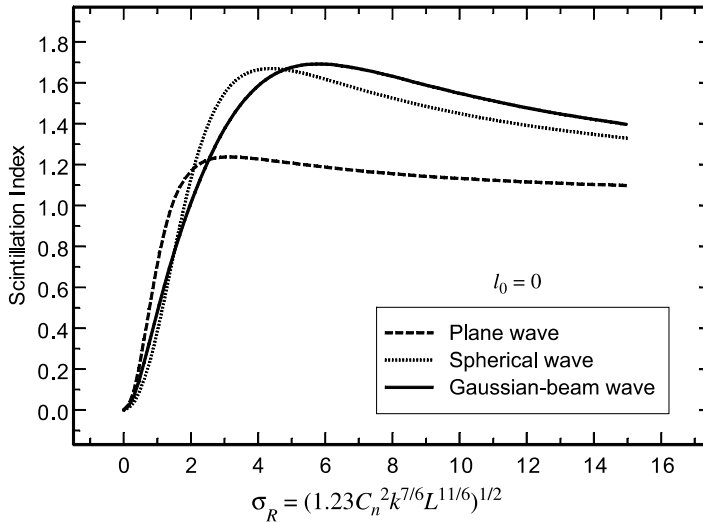

Figure 9.12 Scintillation index for an infinite plane wave, spherical wave, and on-axis for a collimated beam, all plotted as a function of the square root of the Rytov variance. Results are based on a Kolmogorov spectrum.
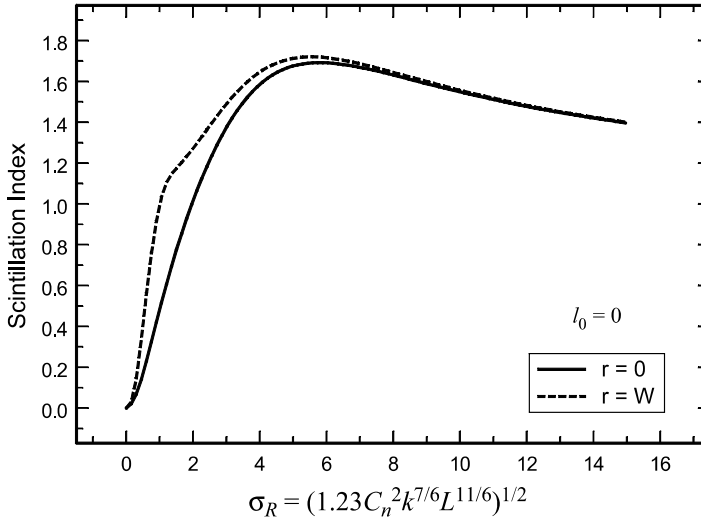
Figure 9.13 Scintillation index on axis (solid curve) and off axis (dashed curve) for a collimated beam plotted as a function of the square root of the Rytov variance. Results are based on a Kolmogorov spectrum.

an anomaly of the effective beam parameters as the strength of turbulence increases, not necessarily characteristic of actual beam behavior.

9.6.3 Inner scale and outer scale effects

When inner scale and outer scale effects cannot be ignored, we base our results on the general spectrum model described by Eqs. (3)–(6). Under weak fluctuations, it has been shown that the longitudinal component of the scintillation index for a Gaussian beam can be approximated by the expression [36]

$$
\sigma_G^2 = 3.86\sigma_R^2 \left\{ 0.40 \frac{[(1+2\Theta)^2 + (2\Lambda + 3/Q_l)^2]^{11/12}}{[(1+2\Theta)^2 + 4\Lambda^2]^{1/2}} \right.
$$

$$
\times \left[\sin\left(\frac{11}{6}\varphi_2 + \varphi_1\right) + \frac{2.61}{[(1+2\Theta)^2 Q_l^2 + (3+2\Lambda Q_l)^2]^{1/4}} \sin\left(\frac{4}{3}\varphi_2 + \varphi_1\right) \right.
$$

$$
\left. - \frac{0.52}{[(1+2\Theta)^2 Q_l^2 + (3+2\Lambda Q_l)^2]^{7/24}} \sin\left(\frac{5}{4}\varphi_2 + \varphi_1\right) \right]
$$

$$
- \frac{13.40\Lambda}{Q_l^{11/6}[(1+2\Theta)^2 + 4\Lambda^2]} - \frac{11}{6}\left[\left(\frac{1+0.31\Lambda Q_l}{Q_l}\right)^{5/6}\right.
$$

$$
\left.\left. + \frac{1.10(1+0.27\Lambda Q_l)^{1/3}}{Q_l^{5/6}} - \frac{0.19(1+0.24\Lambda Q_l)^{1/4}}{Q_l^{5/6}} \right]\right\},
\tag{104}
$$

where φ_1 and φ_2 are angles defined by

$$\varphi_1 = \tan^{-1}\left(\frac{2\Lambda}{1+2\Theta}\right), \quad \varphi_2 = \tan^{-1}\left[\frac{(1+2\Theta)Q_l}{3+2\Lambda Q_l}\right]. \tag{105}$$

Under moderate-to-strong irradiance fluctuations we once again rely on the extended Rytov theory to develop appropriate expressions for the large-scale and small-scale fluctuations of the optical wave. As in the plane wave and spherical wave cases, it follows that the large-scale scintillation for the Gaussian-beam wave can be expressed as the difference

$$\sigma_{\ln X}^2(l_0, L_0) = \sigma_{\ln X}^2(l_0) - \sigma_{\ln X}^2(L_0), \tag{106}$$

which includes both inner scale and outer scale effects. Invoking the geometric optics approximation, the large-scale log irradiance associated with the longitudinal component under the presence of a finite inner scale takes the form

$$
\begin{aligned}
\sigma_{\ln X}^2(l_0) = {}& 1.06\sigma_R^2 \int_0^1 \int_0^\infty \eta^{-11/6} \exp\left(-\eta/Q_l - \eta/\eta_X - \Lambda\eta\xi^2\right) \\
& \times \left[1 + 1.80(\eta/Q_l)^{1/2} - 0.25(\eta/Q_l)^{7/12}\right] \\
& \times \left\{1 - \cos[\eta\xi(1 - \overline{\Theta}\xi)]\right\} d\eta\, d\xi \\
\cong {}& 0.53\sigma_R^2 \int_0^1 \xi^2(1 - \overline{\Theta}\xi)^2 \int_0^\infty \eta^{1/6} \exp\left(-\eta/Q_l - \eta/\eta_X\right) \\
& \times \left[1 + 1.80(\eta/Q_l)^{1/2} - 0.25(\eta/Q_l)^{7/12}\right] d\eta\, d\xi.
\end{aligned}
\tag{107}
$$

Upon evaluation of the integrals, this simplifies to

$$
\begin{aligned}
\sigma_{\ln X}^2(l_0) = {}& 0.49\sigma_R^2\left(\frac{1}{3} - \frac{1}{2}\overline{\Theta} + \frac{1}{5}\overline{\Theta}^2\right)\left(\frac{\eta_X Q_l}{\eta_X + Q_l}\right)^{7/6} \\
& \times \left[1 + 1.75\left(\frac{\eta_X}{\eta_X + Q_l}\right)^{1/2} - 0.25\left(\frac{\eta_X}{\eta_X + Q_l}\right)^{7/12}\right],
\end{aligned}
\tag{108}
$$

where

$$\eta_X = \left[\frac{0.38}{1 - 3.21\overline{\Theta} + 5.29\overline{\Theta}^2} + 0.47\sigma_R^2 Q_l^{1/6}\left(\frac{\frac{1}{3} - \frac{1}{2}\overline{\Theta} + \frac{1}{5}\overline{\Theta}^2}{1 + 2.20\overline{\Theta}}\right)^{6/7}\right]^{-1}. \tag{109}$$

Outer scale effects in the large-scale fluctuations are described by

$$\sigma_{\ln X}^2(L_0) = 0.49\sigma_R^2\left(\frac{1}{3} - \frac{1}{2}\overline{\Theta} + \frac{1}{5}\overline{\Theta}^2\right)\left(\frac{\eta_{X0}Q_l}{\eta_{X0} + Q_l}\right)^{7/6}$$

$$\times\left[1 + 1.75\left(\frac{\eta_{X0}}{\eta_{X0} + Q_l}\right)^{1/2} - 0.25\left(\frac{\eta_{X0}}{\eta_{X0} + Q_l}\right)^{7/12}\right], \quad (110)$$

where $\eta_{X0} = \eta_X Q_0/(\eta_X + Q_0)$ and $Q_0 = 64\pi^2 L/kL_0^2$.

The small-scale log-irradiance variance $\sigma_{\ln Y}^2(l_0)$ is once again described by (99), but in this case we define

$$\eta_Y = 3(\sigma_R/\sigma_G)^{12/5}\left(1 + 0.69\sigma_G^{12/5}\right). \quad (111)$$

The weak-fluctuation scintillation index σ_G^2 is given by Eq. (104) and hence, the small-scale scintillation index takes the form

$$\sigma_{\ln Y}^2(l_0) = \frac{0.51\sigma_G^2}{(1 + 0.69\sigma_G^{12/5})^{5/6}}. \quad (112)$$

As previously pointed out, the radial component is relatively insensitive to the effects of inner scale. For that reason, we will include inner-scale effects only in the longitudinal component. However, if we use the outer-scale model for the radial component developed in Ref. [36], our expression for the radial component of the scintillation index of a Gaussian-beam wave is approximated by

$$\sigma_{I,r}^2(\mathbf{r}, L) = 4.42\sigma_R^2\Lambda_e^{5/6}\left[1 - 1.15\left(\frac{\Lambda_e L}{kL_0^2}\right)^{1/6}\right]\frac{r^2}{W_{LT}^2}, \quad 0 \le r < W. \quad (113)$$

Next, by combining the results given by (108), (110), (112), and (113), we obtain the scintillation model for a Gaussian-beam wave under strong irradiance fluctuations given by

$$\sigma_I^2(\mathbf{r}, L)_{\text{untracked}} = 4.42\sigma_R^2\Lambda_e^{5/6}\left[1 - 1.15\left(\frac{\Lambda_e L}{kL_0^2}\right)^{1/6}\right]\frac{r^2}{W_{LT}^2}$$

$$+ \exp\left[\sigma_{\ln X}^2(l_0) - \sigma_{\ln X}^2(L_0) + \frac{0.51\sigma_G^2}{(1 + 0.69\sigma_G^{12/5})^{5/6}}\right] - 1,$$

$$0 \le r < W. \quad (114)$$

In arriving at (114) we have neglected the minor modifications in both the radial and the longitudinal components that might arise due to beam wander pointing-error effects (see the discussion in Sections 9.6.1 and 9.6.2). Thus, we have generally limited the usefulness of (114) to untracked collimated or divergent beams. However, it may also apply to some convergent beams provided the initial beam diameter is not too large. In Fig. 9.14 we plot the longitudinal component deduced from Eq. (114) with $r = 0$ for a collimated beam and inner scale values
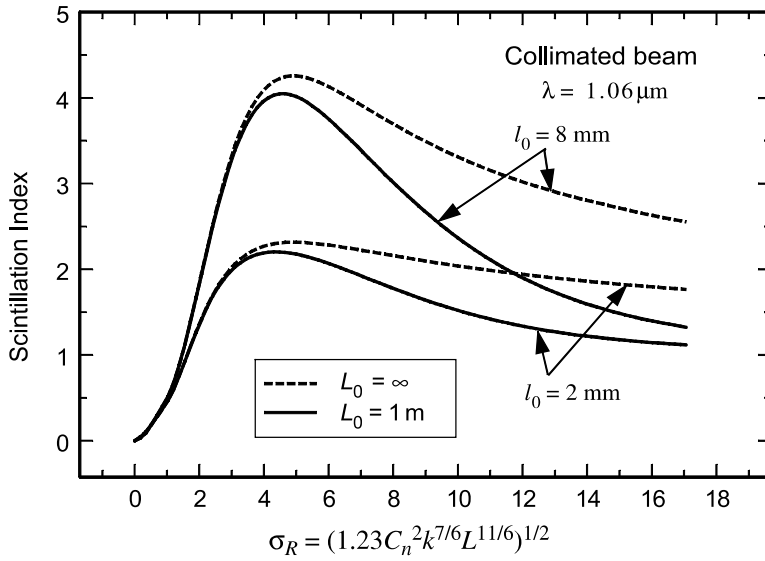
Figure 9.14 Longitudinal component of the scintillation index of a collimated beam vs. σ_R for outer scale $L_0 = \infty$ (dashed lines) and $L_0 = 1$, m (solid lines). Inner-scale values of 2 mm and 8 mm are included in each case and $C_n^2 = 5 \times 10^{-13}\,\mathrm{m}^{-2/3}$.

$l_0 = 2$ and 8 mm. Here we have also selected the parameters $\lambda = 1.06\,\mu$m, $L_0 = 1$ m, and $C_n^2 = 5 \times 10^{-13}\,\mathrm{m}^{-2/3}$. The dashed lines are comparable scintillation values that arise with all parameters the same except $L_0 = \infty$. From the figure it is clear that the outer scale has a negligible effect on the longitudinal component of scintillation under weak fluctuations, but for $\sigma_R > 4$ it initially reduces scintillation at a steeper rate than with an infinite outer scale in much the same fashion as for the plane wave and spherical wave cases.

In Figs. 9.15 and 9.16 we plot the large-scale and small-scale fluctuations σ_X^2 and σ_Y^2 as functions of the rms Rytov variance at the optical axis of a collimated Gaussian-beam wave with a 0.5-cm radius at the transmitter and wavelength $\lambda = 1\,\mu$m. We take atmospheric conditions described by the modified atmospheric spectrum with inner scale sizes of 3 and 8 mm, outer scale of 1 m, and a fixed value of the refractive-index structure parameter $C_n^2 = 0.75 \times 10^{-13}\,\mathrm{m}^{-2/3}$. Variations in the rms Rytov variance are therefore due only to changes in propagation path length. For comparison purposes, we also illustrate the large-scale and small-scale fluctuations based on a Kolmogorov spectrum. Here we note that both large-scale and small-scale behavior based on the Kolmogorov spectrum is essentially the same behavior depicted in Fig. 9.4 for an infinite plane wave. However, the presence of an inner scale in our model significantly increases the large-scale fluctuations near the focusing regime (Fig. 9.15). This increase in scintillation is clearly a consequence of the role that the inner scale plays in defining the scattering disk when $\rho_0 \ll l_0$, viz., $L/k\rho_0 \sim C_n L^{3/2} l_0^{-1/6}$. Also, the presence of a finite outer scale causes a more rapid drop in large-scale scintillation at larger values of the Rytov variance. At the same time, the presence of an inner scale under strong
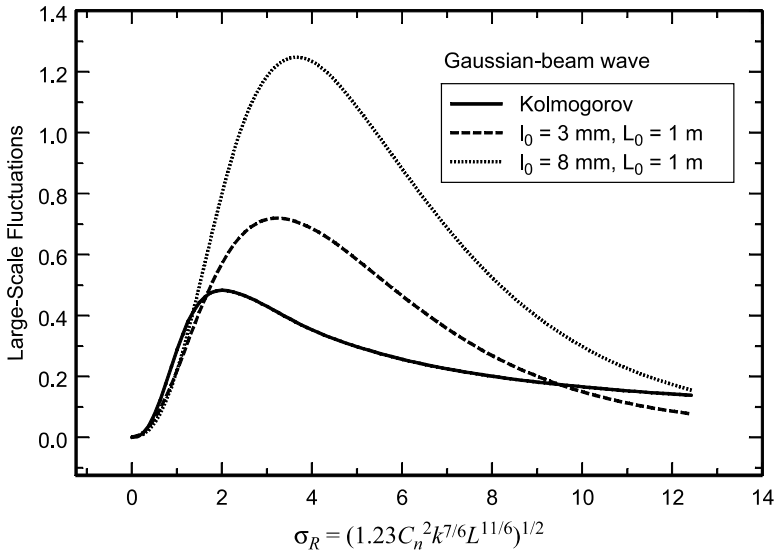
Figure 9.15 Large-scale fluctuations vs. strength of turbulence. The Kolmogorov result is based on $l_0 = 0$ and $L_0 = \infty$. The Gaussian beam is collimated with $W_0 = 0.5$ cm and $\lambda = 1$ μm.
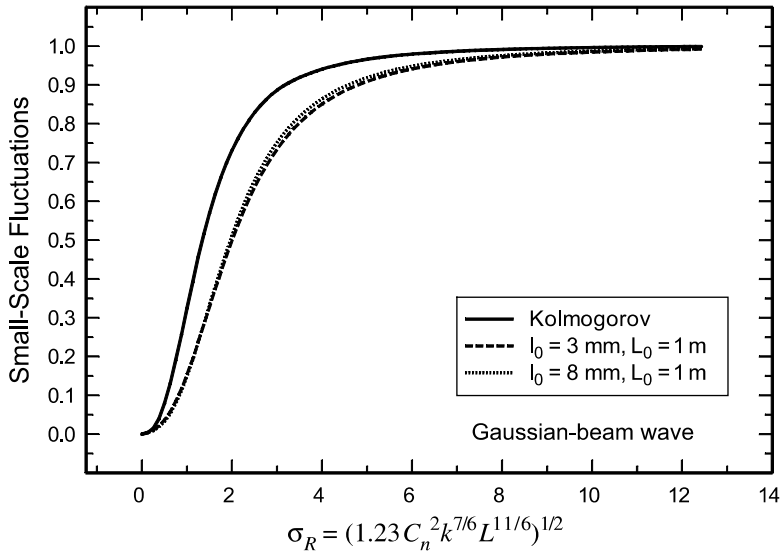

Figure 9.16 Small-scale fluctuations vs. strength of turbulence. The Kolmogorov result is based on $l_0 = 0$ and $L_0 = \infty$. The Gaussian beam is collimated with $W_0 = 0.5$ cm and $\lambda = 1$ μm.

fluctuation conditions tends to decrease the corresponding small-scale fluctuations (Fig. 9.16), whereas the outer scale has no appreciable effect on the small-scale fluctuations. It can be shown that the same general inner-scale and outer-scale behavior depicted here for a Gaussian-beam wave is basically the same for an infinite plane wave and a spherical wave.

9.6.4   Comparison with simulation results

Belmonte [41] conducted a numerical simulation study for the propagation of a collimated Gaussian-beam wave through homogeneous and isotropic turbulence that led to numerical results for a variety of statistical quantities, including the scintillation index. On-axis and off-axis scintillation were treated separately so that the contribution of radial and longitudinal components could be isolated. In Belmonte's analysis a modified von Kármán spectrum described by

$$\Phi_n(\kappa) = 0.033 C_n^2 \frac{\exp\left[-(\kappa l_0/2\pi)^2\right]}{\left(\kappa^2 + 1/L_0^2\right)^{11/6}}$$

was used to model the refractive-index fluctuations. The inherent outer scale was 3 m, equal to the outer width of the numerical grid. Although the modified von Kármán model does not agree with all scintillation values predicted by the modified atmospheric spectrum, the von Kármán spectrum captures most of the behavior of the optical wave. When the two spectrum models are used in the same analysis, the scintillation values derived from the von Kármán spectrum may be somewhat lower under weak irradiance fluctuations than those derived from the modified atmospheric spectrum.

In Fig. 9.17 we show simulation results (open circles) taken from Fig. 17 in Ref. [41] for the longitudinal component of a collimated Gaussian-beam wave with wavelength $\lambda = 2$ μm and beam radius $W_0 = 7$ cm at the transmitter. Atmospheric conditions used for this study were set at $C_n^2 = 10^{-12}$ m$^{-2/3}$, $L_0 = 3$ m, and $l_0 = 1$ cm. Also shown is the corresponding theoretical curve based on (114) for the untracked beam (solid curve) with $r = 0$ and outer scale $L_0 = 3$. However, in the regime where the simulation results are shown we found the dependency on the outer scale was virtually nonexistent for the on-axis scintillation index.

In Fig. 9.18 we show simulation results (open circles) from Fig. 21 in Ref. [41] for the radial component $\sigma_{I,r}^2(\mathbf{r}, L)$ of a collimated beam as a function of radial distance scaled by the effective beam radius. In this figure the distance is fixed at 3 km and the structure constant is $C_n^2 = 10^{-14}$ m$^{-2/3}$. In general, the theoretical curve with infinite outer scale (dashed line) follows the trend of the simulation results but mostly lies above it. However, the theoretical curve with $L_0 = 3$ m (solid line) closely follows the simulation results, showing that the radial component in contrast with the longitudinal component is very sensitive to the presence of a finite outer scale. And, although we generally restrict the theoretical model (114) to radial distances in which $r < W$, we see that the theoretical curve in Fig. 9.18 with $L_0 = 3$ m actually provides an excellent fit in the radial direction out to the point where $r = W_{\mathrm{LT}}$ and somewhat beyond.
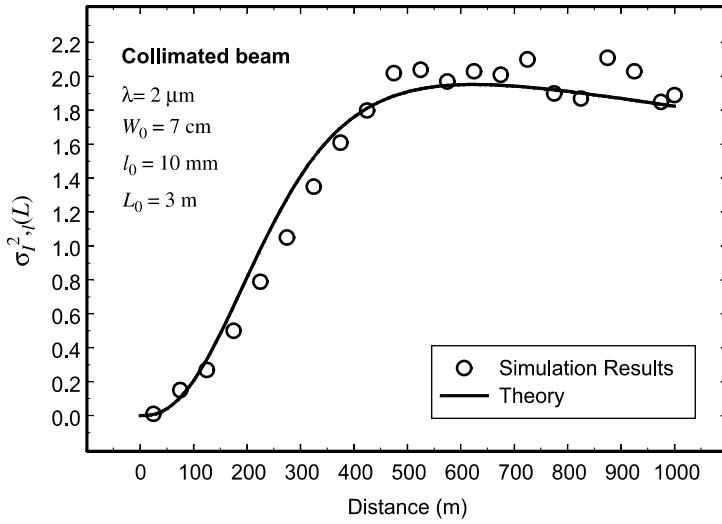
Figure 9.17 On-axis Gaussian-beam wave scintillation index vs. propagation distance. The open circles represent simulation results and the solid line comes from Eq. (114) with $r = 0$. (Simulation results courtesy of A. Belmonte [41].)
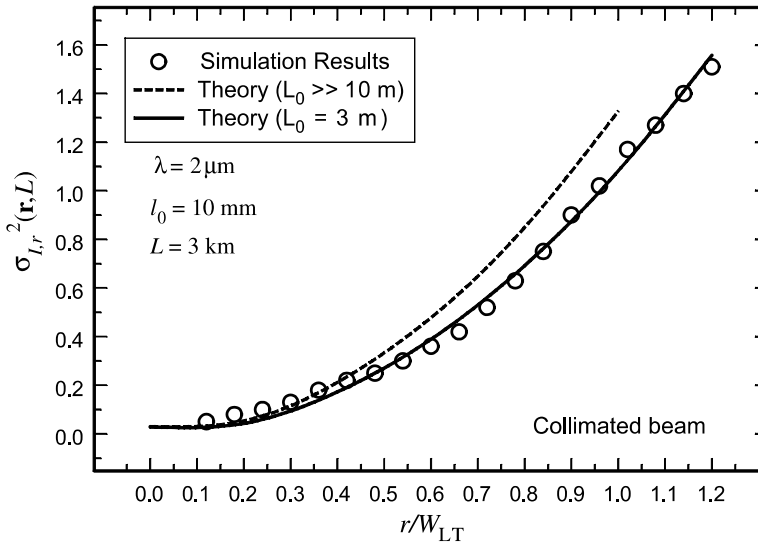

Figure 9.18 Off-axis component of Gaussian-beam wave scintillation index vs. radial distance scaled by the effective beam radius. The open circles represent simulation results and the theoretical curves come from the radial component (113). (Simulation results courtesy of A. Bemonte [41].)

9.7   Covariance Function of Irradiance

In this section we develop expressions for the large-scale and small-scale log-irradiance covariance functions from which we construct the *irradiance covariance function*. The covariance function is useful in defining a characteristic *correlation width* ρ_c (m) for the irradiance fluctuations. Based on the assumed modulation process $I = XY$, the irradiance covariance function can be expressed as a sum

$$B_I(\rho) = B_X(\rho) + B_Y(\rho) + B_X(\rho)B_Y(\rho), \qquad (115)$$

where ρ denotes separation distance between two points on the wave front, $B_X(\rho)$ is the covariance attributed to the large-scale eddies, and $B_Y(\rho)$ is the covariance attributed to the small-scale eddies. Analogous to the scintillation index, the covariance of irradiance (115) can also be expressed as

$$B_I(\rho) = \exp[B_{\ln X}(\rho) + B_{\ln Y}(\rho)] - 1, \qquad (116)$$

where $B_{\ln X}(\rho)$ and $B_{\ln Y}(\rho)$ are the large-scale and small-scale log-irradiance covariances.

9.7.1   Plane wave model

Our treatment here will be limited to the infinite plane wave model. If we initially neglect inner scale and outer scale effects, the geometrical optics approximation applied to the log-irradiance covariance of large-scale fluctuations leads to the expression [26,30]

$$B_{\ln X}(\rho) = 1.06\sigma_R^2 \int_0^1 \int_0^\infty \eta^{-11/6} \exp\left(-\eta/\eta_X\right) J_0(\rho\sqrt{k\eta/L})(1 - \cos \eta\xi)\, d\eta\, d\xi$$

$$\cong 0.16\sigma_R^2 \eta_X^{7/6}\, {}_1F_1\left(\frac{7}{6}; 1;\ -\frac{k\rho^2\eta_X}{4L}\right), \qquad (117)$$

where η_X is defined by (40) and ${}_1F_1$ denotes a confluent hypergeometric function [40]. The corresponding log-irradiance covariance of small-scale fluctuations is approximated by

$$B_{\ln Y}(\rho) = 1.06\sigma_R^2 \int_0^1 \int_0^\infty (\eta + \eta_Y)^{-11/6} J_0\left(\rho\sqrt{k\eta/L}\right)(1 - \cos \eta\xi)\, d\eta\, d\xi$$

$$\cong 1.27\sigma_R^2 \left(\frac{k\rho^2}{L\eta_Y}\right)^{5/12} K_{5/6}\left(\sqrt{\frac{k\rho^2\eta_Y}{L}}\right), \qquad 118)$$

where we have made the approximation $1 - \cos \eta\xi \cong 1$ similar to that in (42). The parameter η_Y is defined by (45) and $K_\nu(x)$ is a modified Bessel function of the second kind. These expressions lead to the covariance function given by

$$B_{I,\,\mathrm{pl}}(\rho) = \exp\left[\frac{0.49\sigma_R^2}{\left(1 + 1.11\sigma_R^{12/5}\right)^{7/6}} {}_1F_1\left(\frac{7}{6}; 1; -\frac{k\rho^2\eta_X}{4L}\right)\right.$$

$$\left. + \frac{0.50\sigma_R^2}{\left(1 + 0.69\sigma_R^{12/5}\right)^{5/6}} \left(\frac{k\rho^2\eta_Y}{L}\right)^{5/12} K_{5/6}\left(\sqrt{\frac{k\rho^2\eta_Y}{L}}\right)\right] - 1. \quad (119)$$

It is customary to equate the *irradiance correlation width* ρ_c with either the $1/e$ or the $1/e^2$ value of the normalized covariance function

$$b_I(\rho) = \frac{B_X(\rho) + B_Y(\rho) + B_X(\rho)B_Y(\rho)}{\sigma_X^2 + \sigma_Y^2 + \sigma_X^2\sigma_Y^2}. \quad (120)$$

In Fig. 9.19 we show the normalized plane wave covariance function (120) for various values of the Rytov variance depicting weak fluctuation conditions ($\sigma_R^2 \ll 1$), the focusing regime ($\sigma_R^2 = 4$), and strong fluctuation conditions ($\sigma_R^2 = 50$). This behavior agrees qualitatively with known results. Namely, in weak scintillations the correlation width of irradiance fluctuations is determined by the Fresnel zone $\sqrt{L/k}$, whereas that in strong fluctuation regimes is defined by the spatial coherence radius ρ_0. Also, the long correlation tail for strong turbulence is characterized by the scattering disk $L/k\rho_0$.
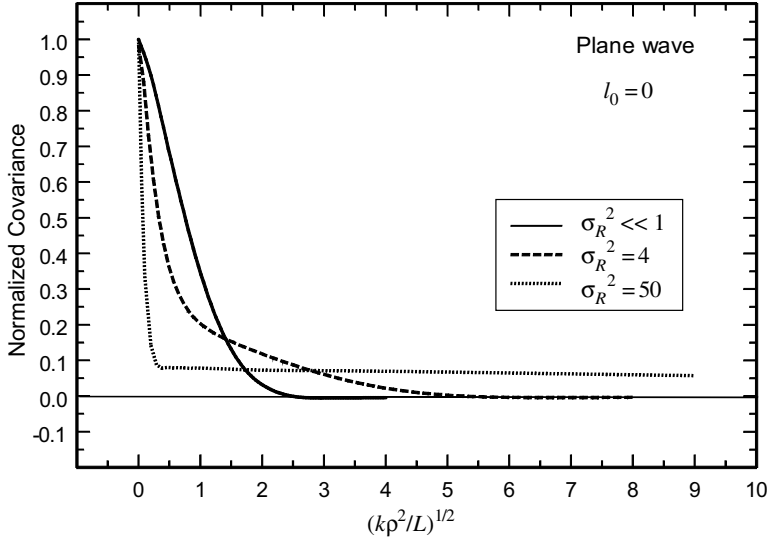

Figure 9.19 Normalized covariance (120) vs. transverse distance scaled by the Fresnel zone for various strengths of irradiance fluctuations. Inner scale and outer scale effects are ignored.

In the presence of inner scale and outer scale effects, we obtain the expression [26]

$$B_{I,\mathrm{pl}}(\rho) = \exp[B_{\ln X}(l_0, \rho) - B_{\ln X}(L_0, \rho)$$

$$+ \frac{0.50\sigma_{PL}^2}{(1 + 0.69\sigma_{PL}^{12/5})^{5/6}} \left(\frac{k\rho^2\eta_Y}{L}\right)^{5/12} K_{5/6}\left(\sqrt{\frac{k\rho^2\eta_Y}{L}}\right)\Bigg] - 1, \qquad (121)$$

where

$$B_{\ln X}(l_0, \rho) = 1.06\sigma_R^2 \int_0^1 \int_0^\infty \eta^{-11/6} \exp\left(-\eta/Q_l - \eta/\eta_X\right) J_0(\rho\sqrt{k\eta/L})$$

$$\times \left[1 + 1.80(\eta/Q_l)^{1/2} - 0.25(\eta/Q_l)^{7/12}\right](1 - \cos\eta\xi)\,d\eta\,d\xi$$

$$\cong 0.16\sigma_R^2 \left(\frac{\eta_X Q_l}{\eta_X + Q_l}\right)^{7/6} \left\{ {}_1F_1\left[\frac{7}{6}; 1; -\frac{k\rho^2}{4L}\left(\frac{\eta_X Q_l}{\eta_X + Q_l}\right)\right]\right.$$

$$+ 1.75\left(\frac{\eta_X}{\eta_X + Q_l}\right)^{1/2} {}_1F_1\left[\frac{5}{3}; 1; -\frac{k\rho^2}{4L}\left(\frac{\eta_X Q_l}{\eta_X + Q_l}\right)\right]$$

$$- 0.25\left(\frac{\eta_X}{\eta_X + Q_l}\right)^{7/12} {}_1F_1\left[\frac{7}{4}; 1; -\frac{k\rho^2}{4L}\left(\frac{\eta_X Q_l}{\eta_X + Q_l}\right)\right]\right\}, \qquad (122)$$

η_X is defined by (54), $B_{\ln X}(L_0, \rho)$ is the same as (122) with η_X replaced by η_{X0} [see (57)], and $Q_l = 10.89\,L/kl_0^2$. The small-scale log-irradiance covariance is the same as (118) but with η_Y defined by (59). Inner scale effects with $L_0 = \infty$ are depicted in Figs. 3.6–3.8 of Ref. [30].

9.7.2 Spherical wave model

In this section we develop the covariance function of irradiance for the case of a spherical wave. Unlike the plane wave, here our expressions are developed only for negligible inner scale and outer scale. Following the treatment for a plane wave, we find that for a spherical wave the large-scale log-irradiance covariance leads to [26]

$$B_{\ln X}(\rho) = 2.65\beta_0^2 \int_0^1 \int_0^\infty \eta^{-11/6} \exp\left(\frac{-\eta}{\eta_X}\right) J_0(\rho\xi\sqrt{k\eta/L})$$

$$\times \left\{1 - \cos[\eta\xi(1 - \xi)]\right\}d\eta\,d\xi$$

$$\cong 0.04\beta_0^2 \eta_X^{7/6}\, {}_3F_3\left(\frac{7}{6}, \frac{3}{2}, 2; \frac{7}{2}, 3, 1; -\frac{k\rho^2\eta_X}{4L}\right), \qquad (123)$$

where $_3F_3$ denotes a generalized hypergeometric function [40] and η_X is defined by Eq. (68). The corresponding small-scale log-irradiance covariance is

$$
\begin{aligned}
B_{\ln Y}(\rho) = {} & 2.65\beta_0^2 \int_0^1 \int_0^\infty (\eta + \eta_Y)^{-11/6} J_0(\rho\xi\sqrt{k\eta/L}) \\
& \times \{1 - \cos[\eta\xi(1 - \xi)]\}d\eta\, d\xi \\
\cong {} & 3.18\beta_0^2 \eta_Y^{-5/6} {}_1F_2\left(\frac{1}{2}; \frac{1}{6}, \frac{3}{2}; \frac{k\rho^2\eta_Y}{4L}\right) \\
& - 2.22\beta_0^2\left(\frac{k\rho^2}{L}\right)^{5/6} {}_1F_2\left(\frac{4}{3}; \frac{11}{6}, \frac{7}{3}; \frac{k\rho^2\eta_Y}{4L}\right), \quad (124)
\end{aligned}
$$

where η_Y is defined by Eq. (71) and $_1F_2$ is a generalized hypergeometric function (see Appendix I or [40]). These expressions lead to the covariance function given by

$$
\begin{aligned}
B_{I,\mathrm{sp}}(\rho) = \exp\Bigg[& \sigma_{\ln X}^2 {}_3F_3\left(\frac{7}{6}, \frac{3}{2}, 2; \frac{7}{2}, 3, 1; -\frac{k\rho^2\eta_x}{4L}\right) \\
& + \sigma_{\ln Y}^2 {}_1F_2\left(\frac{1}{2}; \frac{1}{6}, \frac{3}{2}; \frac{k\rho^2\eta_Y}{4L}\right) - 2.22\sigma_{\ln Y}^2 \left(\frac{k\rho^2\eta_Y}{4L}\right)^{5/6} \\
& \times {}_1F_2\left(\frac{4}{3}; \frac{11}{6}, \frac{7}{3}; \frac{k\rho^2\eta_Y}{4L}\right)\Bigg] - 1, \quad (125)
\end{aligned}
$$

where the log-irradiance variances appearing above are defined by (69) and (72).

In Fig. 9.20, the normalized covariance function for a spherical wave is shown for weak fluctuations ($\beta_0^2 \ll 1$), the focusing regime ($\beta_0^2 = 4$), and strong fluctuations ($\beta_0^2 = 36$). The general behavior is similar to that for a plane wave.

9.8 Temporal Spectrum of Irradiance

In Section 8.4 we used the Taylor frozen turbulence hypothesis to convert the spatial covariance function to the temporal covariance function from which we then calculated the *power spectral density* (PSD) of irradiance. Here we wish to extend that analysis to include the strong irradiance fluctuation regime, but limit our analysis to the case of a plane wave. We will also ignore the effects of a finite inner scale and outer scale.
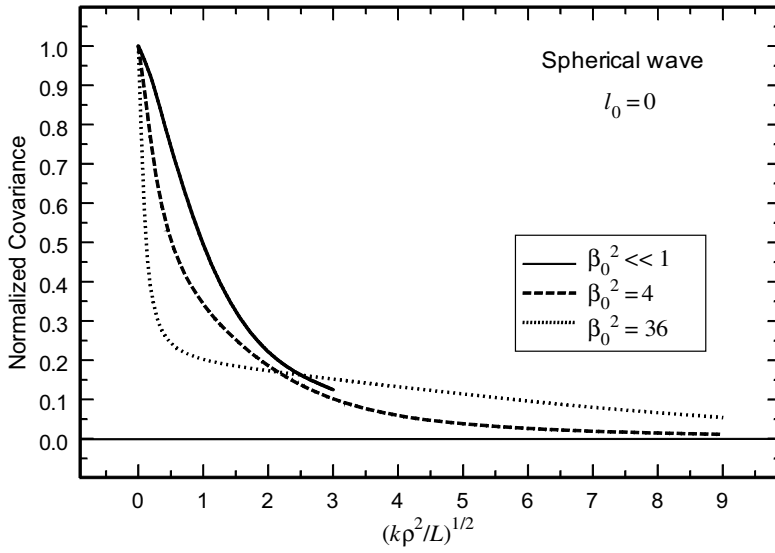
Figure 9.20 Normalized covariance of spherical wave for various strengths of turbulence. Inner scale and outer scale effects are ignored.

The implied temporal covariance function deduced from Eq. (119) by setting $\rho = V_\perp \tau$ is

$$B_{I,\text{pl}}(\tau, L) = \exp\left[\frac{0.49\sigma_R^2}{\left(1 + 1.11\sigma_R^{12/5}\right)^{7/6}} \, {}_1F_1\left(\frac{7}{6}; 1; -\frac{kV_\perp^2\tau^2\eta_X}{4L}\right)\right.$$

$$\left. + \frac{0.50\sigma_R^2}{\left(1 + 0.69\sigma_R^{12/5}\right)^{5/6}} \left(\frac{kV_\perp^2\tau^2\eta_Y}{L}\right)^{5/12} K_{5/6}\left(\sqrt{\frac{kV_\perp^2\tau^2\eta_Y}{L}}\right)\right] - 1.$$

$$(126)$$

Given the temporal covariance function, the irradiance spectrum is determined by solving

$$S_I(\omega) = 4\int_0^\infty B_{I,\text{pl}}(\tau, L)\cos\omega\tau\, d\tau, \tag{127}$$

which, following the change of variables $s = \omega_t\tau$, where $\omega_t = V_\perp/\sqrt{L/k}$, leads to a more useful form for numerical calculations given by

$$S_I(\omega) = \frac{4}{\omega_t}\int_0^\infty B_{I,\text{pl}}(s/\omega_t, L)\cos\left(\frac{\omega s}{\omega_t}\right) ds. \tag{128}$$

The quantity ω_t physically represents the transition frequency at which the spectrum begins to decay under weak fluctuations.

In Fig. 9.21, the scaled PSD $\omega_t S_I(\omega)$ deduced from (128) for a plane wave is plotted as a function of ω/ω_t for the same values of the Rytov variance appearing
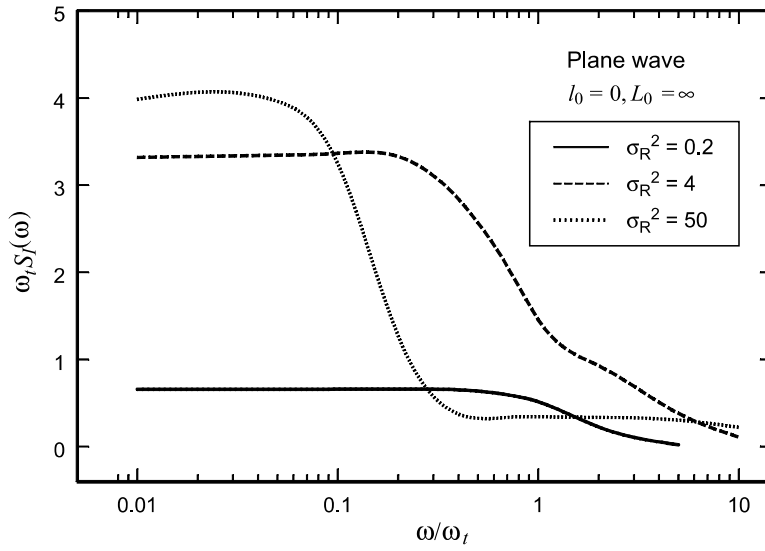
Figure 9.21 Temporal power spectrum $\omega_t S_I(\omega)$ of a plane wave plotted as a function of radial frequency scaled by the quantity $\omega_t = V_\perp / \sqrt{L/k}$, where $V_\perp$ is transverse wind speed.

in Fig. 9.19. Regardless of the strength of optical turbulence, the temporal spectrum is approximately constant at low frequencies and then drops off sharply to level again near zero at high frequencies. The quantity $\omega S_I(\omega)/2\pi\sigma_I^2$ is plotted in Fig. 9.22 as a function of ω/ω_t also with zero inner scale. Plotting the frequency
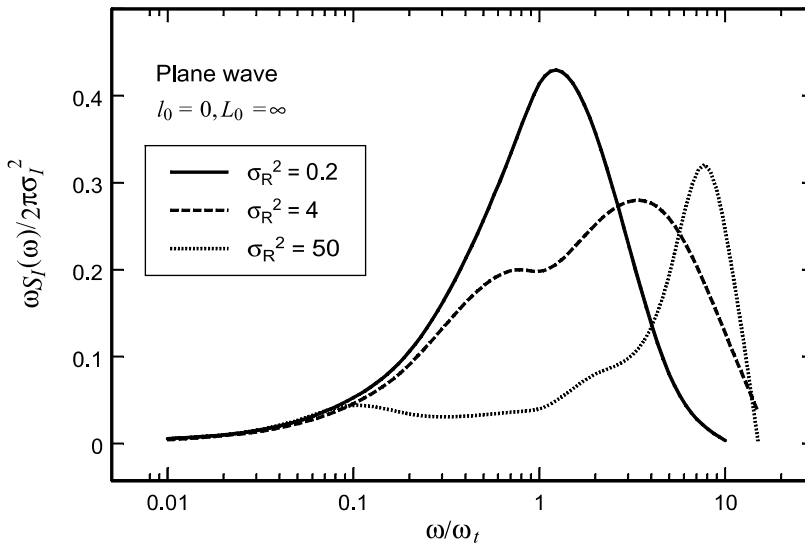

Figure 9.22 Temporal power spectrum $\omega S_I(\omega)/2\pi\sigma_I^2$ of a plane wave plotted as a function of radial frequency scaled by the quantity $\omega_t = V_\perp / \sqrt{L/k}$, where $V_\perp$ is transverse wind speed.

spectrum in this latter fashion provides a clear representation of the distribution of power of the irradiance fluctuations as turbulence strength is increased. Also, the two-scale characteristic of the covariance function is apparent in both Figs. 9.21 and 9.22 for the temporal spectrum under strong irradiance fluctuations. We note that the curves in Fig. 9.22 correspond qualitatively with experimental data shown in Fig. 4.13 of Gracheva et al. [42]. Namely, these curves show that the relative contributions of the high frequencies to the variance increase as the Rytov parameter σ_R^2 increases.

9.9 Distribution Models for the Irradiance

For many years the scientific community has expressed interest in the possibility of using high-data-rate optical transmitters for radar and free space optical (FSO) communications. Applications that could benefit from FSO communication, or *lasercom*, systems are those that have platforms with limited weight and space, require very high data links, and must operate in an environment where fiber-optic links are not practical.

The performance of a laser radar or FSO communication system can be significantly diminished by turbulence-induced scintillation resulting from beam propagation through the atmosphere. Specifically, scintillation can lead to power losses at the receiver and eventually to fading of the received signal below a detectable threshold. The reliability of an optical system operating in such an environment can be deduced from a mathematical model for the *probability density function* (PDF) of the randomly fading irradiance signal. For that reason, one of the goals in studying optical wave propagation through optical turbulence has been the identification of a tractable PDF of the irradiance under all irradiance fluctuation conditions. Over the years, many irradiance PDF models have been proposed with varying degrees of success.

In Section 5.5 we introduced the weak-irradiance fluctuation models known as the modified Rician and lognormal distributions. The modified Rician PDF is a consequence of the Born approximation, whereas the lognormal model follows from the first-order Rytov approximation. Outdoor field measurements [15,16] leading to the lower-order normalized moments $\langle I^n \rangle / \langle I \rangle^n$, $n = 1, 2, 3, \ldots$, generally agree well with values predicted by the lognormal model, but not so with the modified Rician PDF (recall Fig. 5.1). Nonetheless, it has been observed that the lognormal PDF for irradiance can underestimate the peak of the probability density function and also underestimate the behavior in the tails as compared with measured data [23,24,43]. Underestimating the tails of a PDF has important consequences on radar and communication systems where detection and fade probabilities are calculated over the tails of the PDF. In particular, the fade probability is calculated over the interval $0 \leq I < I_T$, where I_T is a specified threshold.

To address the strong fluctuation or multiple scattering regime, a number of statistical models were developed throughout the seventies and eighties, and even into the nineties, but most have various shortcomings. The most useful

models are those based on heuristic arguments and observed experimental data, leading to a PDF of the amplitude, or irradiance, of the optical field that often shows good agreement with experimental data. These distributions are often based on atmospheric models that relate discrete scattering regions in the turbulent medium to the individual phase front inhomogeneities in the optical wave. If the number of discrete scattering regions is sufficiently large, the radiation field of the wave is approximately zero-mean Gaussian, and, thus, the irradiance statistics of the field are governed by the *negative exponential distribution*. This happens only far into the saturation regime. Below we briefly introduce two of the more popular models that have been developed specifically for the strong fluctuation regime, both of which have evolved from an assumed modulation process. We follow this in Section 9.10 with the development of a more recent model applicable under all conditions of optical turbulence.

9.9.1 *K* distribution models

One of the early models to gain wide acceptance for the strong scattering regime is the K distribution [44–47]. The K distribution was originally proposed as a model for non-Rayleigh sea echo, but it was later discovered that the general family of K distributions provide excellent models for predicting amplitude or irradiance statistics in a variety of experiments involving radiation scattered by turbulent media.

Although usually formulated from a discrete statistics point of view, the K distribution can also be derived from a modulation process wherein the PDF of irradiance is assumed governed by the conditional negative exponential distribution

$$p_1(I \mid b) = \frac{1}{b}\exp(-I/b), \quad I > 0, \tag{129}$$

where the mean irradiance b is itself a random quantity. The unconditional PDF for the irradiance is obtained by calculating the expected value

$$p(I) = \int_0^\infty p_1(I \mid b)p_2(b)\,db, \quad I > 0, \tag{130}$$

where $p_2(b)$ is the distribution function of the fluctuating mean irradiance, assumed to be the gamma distribution

$$p_2(b) = \frac{\alpha(\alpha b)^{\alpha-1}}{\Gamma(\alpha)}\exp(-\alpha b), \quad b > 0. \tag{131}$$

In (131), $\Gamma(\alpha)$ is the gamma function and α is a positive parameter related to the effective number of discrete scatterers; also, we have assumed the mean of b is unity for convenience. The resulting distribution arising from (130) is given by

$$p(I) = \frac{2\alpha}{\Gamma(\alpha)}(\alpha I)^{(\alpha-1)/2}K_{\alpha-1}(2\sqrt{\alpha I}), \quad I > 0, \tag{132}$$

where $K_p(x)$ is a modified Bessel function of the second kind. Because of the presence of this particular Bessel function, the PDF (132) became widely known as the *K distribution*. As $\alpha \to \infty$, the *K* distribution tends to the negative exponential distribution [i.e., the gamma distribution (131) approaches a delta function].

The scintillation index predicted by the *K* distribution assumes the form $\sigma_I^2 = 1 + 2/\alpha$, which always exceeds unity but approaches it in the limit $\alpha \to \infty$. Hence, the *K* distribution is applicable only in strong fluctuation regimes. One extension of the *K* distribution to also cover weak fluctuation regimes for which the scintillation index is less than unity is the *I-K distribution* [48–50]. However, both the *K* and *I-K* models have limitations as PDF models for the irradiance in extended turbulence, some of which were reported by Churnside and Frehlich [43] in making comparisons of these PDFs with measured irradiance data in extended turbulence.

9.9.2 Lognormal-Rician distribution

Later models arising out of an assumed modulation process were the *lognormally modulated exponential distribution* [51] (valid only under strong fluctuation conditions) and the more general *lognormal-Rician distribution* [23,24,52], the latter also called *Beckman's PDF* in more recent publications. Both of these models (where applicable) show excellent agreement with experimental data and simulation results concerning the PDF [23,24,51]. The lognormal-Rician PDF, which evolves from the product of a Rician amplitude and a lognormal modulation factor, can be expressed as

$$p(I) = \frac{(1+r)e^{-r}}{\sqrt{2\pi}\sigma_z} \int_0^\infty I_0\left[2\sqrt{\frac{(1+r)rI}{z}}\right] \exp\left[-\frac{(1+r)I}{z} - \frac{(\ln z + \frac{1}{2}\sigma_z^2)^2}{2\sigma_z^2}\right] \frac{dz}{z^2},$$
$$I > 0, \quad (133)$$

where r is a coherence parameter or power ratio, σ_z^2 is the variance of the lognormal modulation factor, and $I_0(x)$ is a modified Bessel function of the first kind. A closed-form solution for this integral is unknown, and its convergence properties for certain parameter values make it somewhat cumbersome for numerical calculations. In addition, like the *K* distribution and *I-K* distribution, it is not known how to relate the parameters r and σ_z^2 of the lognormal-Rician distribution directly to atmospheric conditions.

9.10 Gamma-Gamma Distribution

Based on Eq. (1), the (normalized) irradiance $I = XY$ can be partitioned into factors that act like a modulation process where X and Y arise, respectively, from large-scale and small-scale atmospheric effects. To develop a PDF model of the irradiance with parameters that can be directly related to atmospheric conditions and still be consistent with the scintillation theory presented here, we

assume that both large-scale and small-scale irradiance fluctuations are governed by gamma distributions, viz., [53]

$$p_X(X) = \frac{\alpha(\alpha X)^{\alpha-1}}{\Gamma(\alpha)} \exp(-\alpha X), \quad \alpha > 0, X > 0, \tag{134}$$

$$p_Y(Y) = \frac{\beta(\beta Y)^{\beta-1}}{\Gamma(\beta)} \exp(-\beta Y), \quad \beta > 0, Y > 0. \tag{135}$$

The gamma distribution is selected here because it has been shown to be an excellent approximation for many propagation problems involving intensity (or amplitude) [54]. By first fixing X and writing $Y = I/X$, we obtain the *conditional* PDF

$$p_Y(I \mid X) = \frac{\beta(\beta I/X)^{\beta-1}}{X\Gamma(\beta)} \exp(-\beta I/X), \quad I > 0, \tag{136}$$

in which X is the (conditional) mean value of I. To obtain the unconditional irradiance distribution, we form the average of (136) over the distribution (134), which leads to

$$\begin{aligned} p(I) &= \int_0^\infty p_Y(I \mid X) p_X(X) dX \\ &= \frac{2(\alpha\beta)^{(\alpha+\beta)/2}}{\Gamma(\alpha)\Gamma(\beta)} I^{(\alpha+\beta)/2-1} K_{\alpha-\beta}\left(2\sqrt{\alpha\beta I}\right), \qquad I > 0, \end{aligned} \tag{137}$$

called the *gamma-gamma distribution.*

The gamma-gamma distribution (137) can be interpreted as a generalization of the K distribution (132). To see this, we simply note that the gamma-gamma distribution reduces to the K distribution when either α or β is unity. Also, the gamma-gamma distribution derived here is not a new PDF model. Along with the gamma distribution (related to the m-distribution), the gamma-gamma PDF appears in the much earlier work of Nakagami [54], and it was proposed as an irradiance model for polychromatic and partially developed speckle after propagation through atmospheric turbulence [55]. It also appeared in the work of Lewinski [31] and in that of Teich and Diament [33].

The gamma-gamma PDF (137) is normalized in the sense that $\langle I \rangle = 1$. Thus, for the second moment we have $\langle I^2 \rangle = (1 + 1/\alpha)(1 + 1/\beta)$, and by comparing this result with Eq. (8), we can identify the parameters of the gamma-gamma distribution with the large-scale and small-scale scintillation according to

$$\begin{aligned} \alpha &= \frac{1}{\sigma_X^2} = \frac{1}{\exp(\sigma_{\ln X}^2) - 1}, \\ \beta &= \frac{1}{\sigma_Y^2} = \frac{1}{\exp(\sigma_{\ln Y}^2) - 1}. \end{aligned} \tag{138}$$

It follows that the total scintillation index (9) is related to these parameters by

$$\sigma_I^2 = \frac{1}{\alpha} + \frac{1}{\beta} + \frac{1}{\alpha\beta}. \tag{139}$$

Based on (138), it becomes clear that the parameters α and β can be directly related to atmospheric conditions through models for the large-scale and small-scale scintillations. This feature of the gamma-gamma distribution makes it particularly attractive for predicting detection and fade probabilities associated with a given atmospheric channel (e.g., see Chap. 11).

The cumulative distribution function (CDF) for the gamma-gamma PDF can be found in closed form. For practical purposes, it is the CDF that is of greater interest than the PDF since the former is used to predict probabilities of detection and fade in an optical communication or radar system. The CDF associated with the gamma-gamma distribution is readily found to be [53]

$$\begin{aligned}
P(I \leq I_T) &= \int_0^{I_T} p(I)dI \\
&= \frac{\pi}{\sin[\pi(\alpha - \beta)]\Gamma(\alpha)\Gamma(\beta)} \\
&\quad \times \left\{ \frac{(\alpha\beta I_T)^\beta}{\beta\Gamma(\beta - \alpha + 1)} {}_1F_2(\beta; \beta + 1, \beta - \alpha + 1; \alpha\beta I_T) \right. \\
&\quad \left. - \frac{(\alpha\beta I_T)^\alpha}{\alpha\Gamma(\alpha - \beta + 1)} {}_1F_2(\alpha; \alpha + 1, \alpha - \beta + 1; \alpha\beta I_T) \right\}, \tag{140}
\end{aligned}$$

where I_T is a set threshold.

9.10.1 Plane wave simulation results

Flatté et al. [22] calculated the PDF from numerical simulations for a plane wave propagated through homogeneous and isotropic atmospheric turbulence and compared the results with several PDF models. Here we use results by Al-Habash et al. [53] to compare the gamma-gamma distribution model with some of the plots in Ref. [22] of the log-irradiance PDF as a function of $(\ln I - \langle \ln I \rangle)/\sigma$, covering a range of conditions that extends from weak irradiance fluctuations far into the saturation regime. The quantity $\langle \ln I \rangle$ is the mean value of the log irradiance and $\sigma = (\sigma_{\ln I}^2)^{1/2}$ is the rms value of $\ln I$. The simulation PDFs were displayed in this fashion in the hopes that it would reveal their salient features. In the saturation regime the simulation results obtained by Flatté et al. showed that the plane wave PDF lies somewhere between the lognormal and exponential distributions, and their moments lie between those of a lognormal-exponential distribution and those of a K distribution.

To make the following comparisons, we first note that the large-scale log-irradiance variance in (138) is defined by Eq. (41) in the absence of inner scale
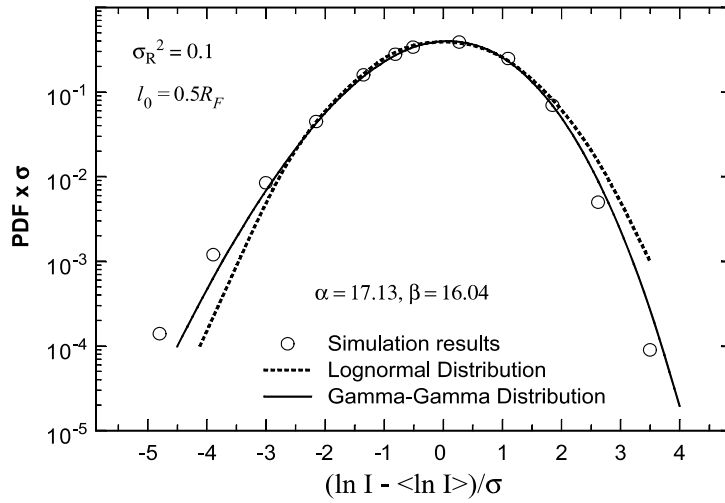
Figure 9.23 PDF of the scaled log irradiance for a plane wave in the case of weak irradiance fluctuations: $\sigma_R^2 = 0.1$ and $l_0/R_F = 0.5$.

and outer scale effects and by Eqs. (51), (55), and (56) in the presence of both inner scale and outer scale. Similarly, the small-scale log-irradiance is defined by either Eq. (46) or by Eq. (60), the latter being the case for a finite (nonzero) inner scale.

We plot in Figs. 9.23–9.27 the predicted log-irradiance PDF associated with the gamma-gamma distribution (solid line) for comparison with the simulation results illustrated in Figs. 4, 5, and 7 of Ref. [22]. As representative of typical atmospheric propagation conditions, we use the inner scale value $l_0 = 0.5R_F$ ($Q_l = 44$) in
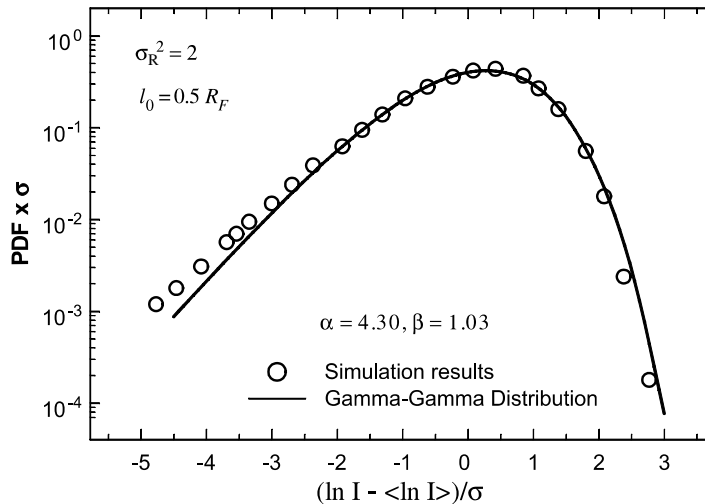

Figure 9.24 Same as Fig. 9.23 with $\sigma_R^2 = 2$, corresponding to moderate irradiance fluctuations. Here we set outer scale parameter $Q_0 = 1$.
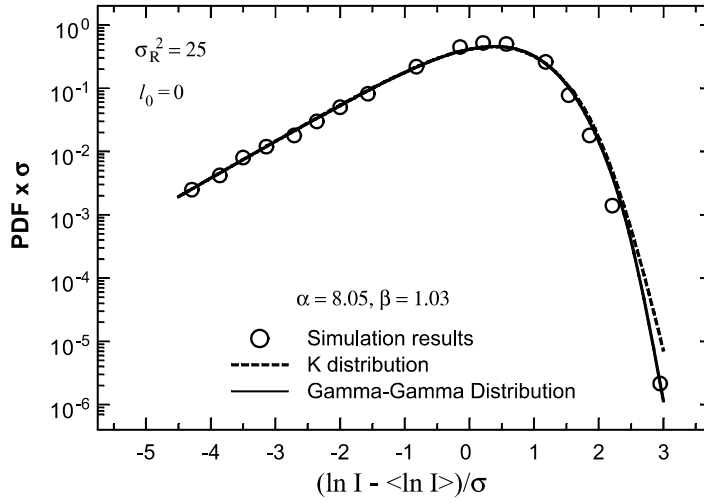
Figure 9.25 PDF of the scaled log irradiance for a plane wave in the case of strong irradiance fluctuations: $\sigma_R^2 = 25$ and $l_0/R_F = 0$.

Figs. 9.23 and 9.24. In Fig. 9.23, we use the simulation values $\sigma_R^2 = 0.1$, $l_0 = 0.5R_F$; and in Fig. 9.24 we use the simulation values $\sigma_R^2 = 2, l_0 = 0.5R_F$, taken from Figs. 4 and 5, respectively, of Ref. [22]. The quantity $R_F = \sqrt{L/k}$ is the scale size of the Fresnel zone. Values of the scaling parameters $\langle \ln I \rangle$ and σ required in the plots for the gamma-gamma PDF are calculated directly from the gamma-gamma PDF, using values of α and β determined from (138). We also plot the lognormal PDF (dashed line) in Fig. 9.23 for the sake of comparison, and in Fig. 9.24 we include the outer-scale parameter $Q_0 = 1$ to achieve a closer fit
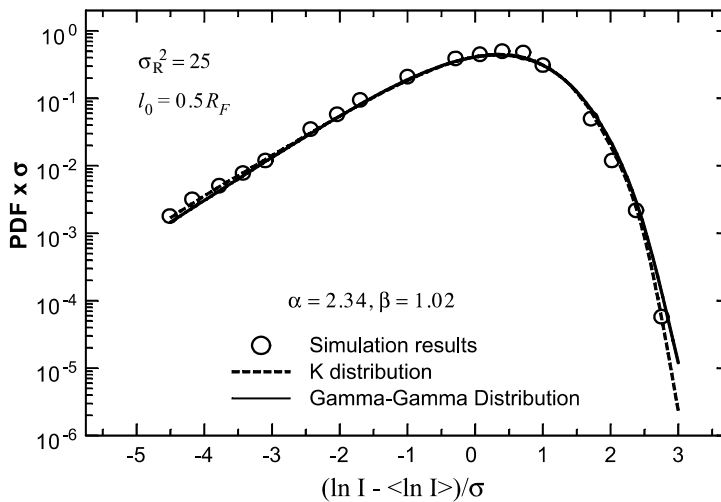

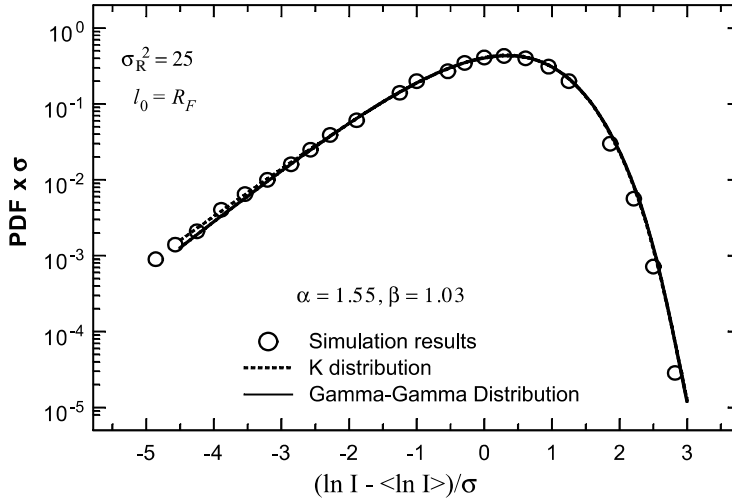**Figure 9.26** Same as Fig. 9.25 with $l_0/R_F = 0.5$.

Figure 9.27   Same as Fig. 9.25 with $l_0/R_F = 1$.

than with $Q_0 = 0$ (infinite outer scale). Note that the gamma-gamma distribution provides a better fit to the weak fluctuation simulation data in Fig. 9.23 than does the lognormal distribution. In fact, the gamma-gamma PDF generally provides a good fit to the simulation results over all abscissa values in Figs. 9.23 and 9.24.

To further test the gamma-gamma model under a variety of inner scale conditions, we considered the three cases presented in Fig. 7 of Ref. [22]. In Fig. 9.25 we use the simulation values $\sigma_R^2 = 25$, $l_0 = 0$ to predict the parameters α and β of the gamma-gamma PDF. This value of the Rytov variance corresponds to the saturation regime, in which the model predicts a scintillation index of $\sigma_{I,\mathrm{pl}}^2 = 1.21$ as compared with the higher simulation value $\sigma_{I,\mathrm{pl}}^2 = 1.39$. In these figures we found the theoretical curves were relatively insensitive to the outer scale over the range of values $0 \leq Q_0 \leq 1$, so the theoretical curves correspond to $Q_0 = 0$. We also plot the K distribution using the simulation results for identifying its free parameter. In this case both distributions provide an excellent fit to the simulation results. In Figs. 9.26 and 9.27, respectively, we use the parameter values $\sigma_R^2 = 25$, $l_0 = 0.5R_F$, and $\sigma_R^2 = 25$, $l_0 = R_F$ ($Q_l = 11$), which correspond to the saturation regime but now with inner-scale effects. The predicted scintillation index is found to be $\sigma_{I,\mathrm{pl}}^2 = 1.82$ and $\sigma_{I,\mathrm{pl}}^2 = 2.25$, respectively, whereas the simulation values are somewhat lower, viz., $\sigma_{I,\mathrm{pl}}^2 = 1.55$ and $\sigma_{I,\mathrm{pl}}^2 = 1.84$. However, once again both the gamma-gamma and K distributions show excellent fits with the PDF simulation results. We do note that in Figs. 9.25 through 9.27 the gamma-gamma parameter $\beta \cong 1$, which means there is little difference between the gamma-gamma PDF and the K distribution in this regime.

Although Flatté et al. [22] did not address the role of the outer scale in their simulation results, it seems plausible from their numerical algorithm that the simulation results could contain an inherent outer scale comparable in size with the outer width of the numerical grid.

9.10.2 Spherical wave simulation results

Hill et al. [23,24] used numerical simulation of the propagation of a spherical wave through homogeneous and isotropic atmospheric turbulence that led to PDF results for the log-irradiance fluctuations of the optical wave. In that analysis they compared several heuristic PDF models with the numerical simulation results and concluded that the lognormal Rician PDF (133) (later called the Beckmann distribution) provided the closest fit over all conditions tested. On the other hand, their simulation results did not generally support the K distribution (132).

Various parameters used in the analysis of the numerical simulation results for a spherical wave include the following:

$$\tilde{\sigma}^2(l_0/R_F) = 10.5 \int_0^1 du \int_0^\infty dx\, x^{-8/3} f(x l_0/R_F) \sin^2\left[x^2 u(1-u)/2\right], \quad (141)$$

$$\sigma^2_{\mathrm{Rytov}} = \beta_0^2 \tilde{\sigma}^2(l_0/R_F), \tag{142}$$

$$\sigma = \sqrt{\sigma^2_{\ln I}}. \tag{143}$$

The quantity $R_F = \sqrt{L/k}$ is the Fresnel zone, β_0^2 is the scintillation index of a spherical wave in the limit of weak scintillation and a Kolmogorov spectrum, and the Rytov parameter (142) is the weak fluctuation scintillation index in the presence of a finite inner scale. The parameter σ is the square root or rms value of the log-irradiance variance. which was used to scale the ordinates and abscissas of the figures in Refs. [23] and [24]. Other parameter values used in the simulations are provided in tabular form in Ref. [23].

The parameter $\tilde{\sigma}^2(l_0/R_F)$ defined by (141) is the ratio between the Rytov parameters $\sigma^2_{\mathrm{Rytov}}$ and β_0^2, with and without inner scale effects. In our calculations we use the expression obtained from (75), viz.,

$$\tilde{\sigma}^2(l_0/R_F) \cong 3.86 \left\{ \left(1 + 9/Q_l^2\right)^{11/12} \left[\sin\left(\frac{11}{6} \tan^{-1}\frac{Q_l}{3}\right) + \frac{2.61}{(9 + Q_l^2)^{1/4}} \right. \right.$$

$$\left. \left. \times \sin\left(\frac{4}{3} \tan^{-1}\frac{Q_l}{3}\right) - \frac{0.52}{(9 + Q_l^2)^{7/24}} \sin\left(\frac{5}{4} \tan^{-1}\frac{Q_l}{3}\right) \right] - \frac{8.75}{Q_l^{5/6}} \right\}. \tag{144}$$

We plot in Figs. 9.28–9.36 simulation PDF results and corresponding PDF values predicted by the lognormal-Rician distribution (dotted line) as a function of $(\ln I + 0.5\sigma^2)/\sigma$ and $\sigma^2_{\mathrm{Rytov}} = 0.06, 2$, and 5. Values of r and σ_z^2 required by the lognormal-Rician PDF were provided in tabular form in Ref. [23] for various values of l_0/R_F and Rytov parameter $\sigma^2_{\mathrm{Rytov}}$. Also shown in the figures are curves deduced from the gamma-gamma distribution (solid line).

In Figs. 9.28–9.30, the inner scale is negligibly small. The gamma-gamma PDF curves in Figs. 9.28 and 9.30 provide very good fits with the simulation results, but
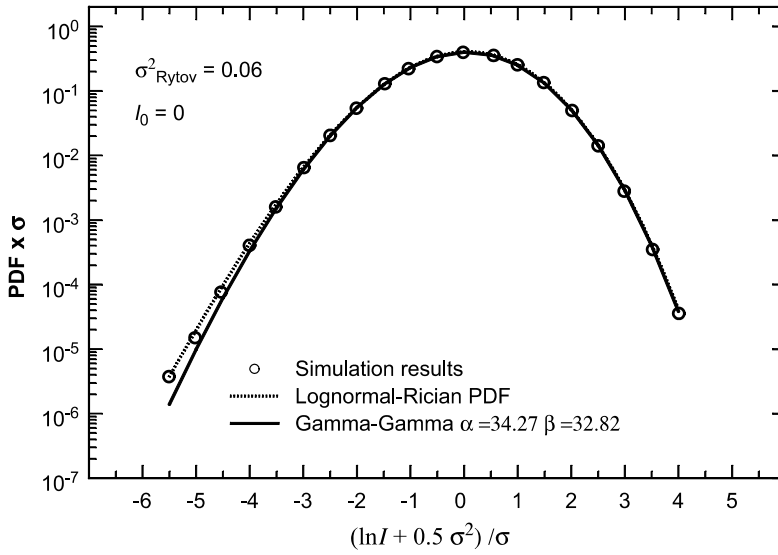
Figure 9.28 PDF of the scaled log irradiance for a spherical wave with: $\sigma^2_{\text{Rytov}} = 0.06$ and $l_0/R_F = 0$. The open circles represent simulation data, the dotted lines is from the lognormal-Rician PDF, and the solid line is from the gamma-gamma PDF.

fairly large deviations in the scaled PDF can be seen in Fig. 9.29 for values along the left side of the abscissa (i.e., small irradiance values). We found that by incrementing the parameters α and β of the gamma-gamma PDF we could produce a "best fit" curve (dashed line) that is comparable to the fit of the

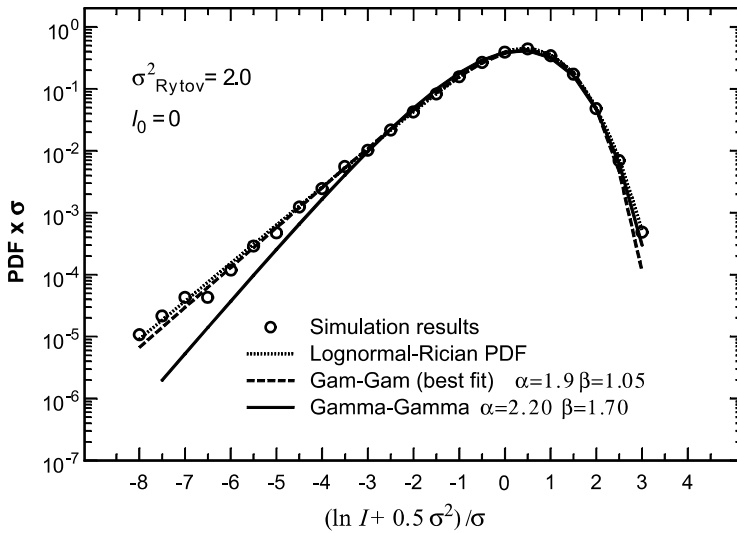**Figure 9.29** Same as Fig. 9.28 with $\sigma^2_{\text{Rytov}} = 2$. Also shown (dashed line) is the gamma-gamma PDF with parameters α and β chose from a best fit to the data.
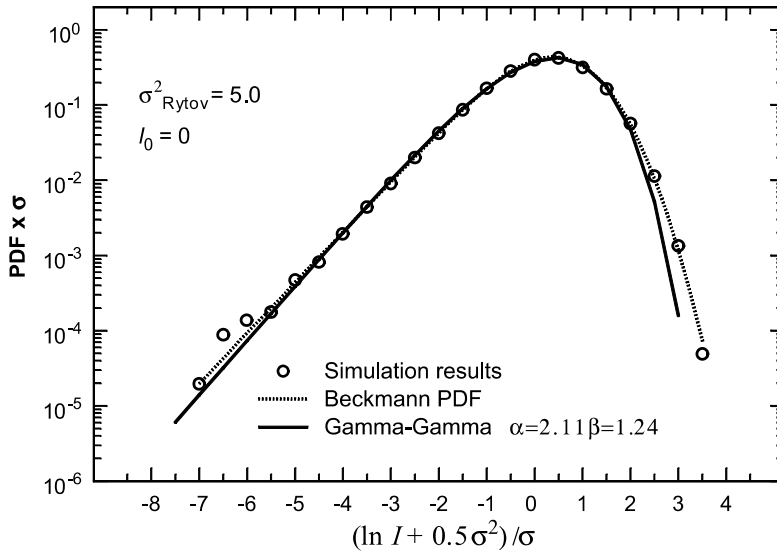
Figure 9.30 Same as Fig. 9.28 with $\sigma^2_{\text{Rytov}} = 5$ corresponding to strong irradiance fluctuations.

lognormal-Rician PDF. This suggests that the gamma-gamma PDF is applicable here, but the scintillation theory used to predict α and β apparently underestimates both large-scale and small-scale scintillations in this particular case.

   The curves and simulation results in Figs. 9.31–9.36 are similar to those in Figs. 9.28–9.30 except that $l_0/R_F = 0.5$ ($Q_l = 44$) in Figs. 9.31–9.33 and $l_0/R_F = 1$
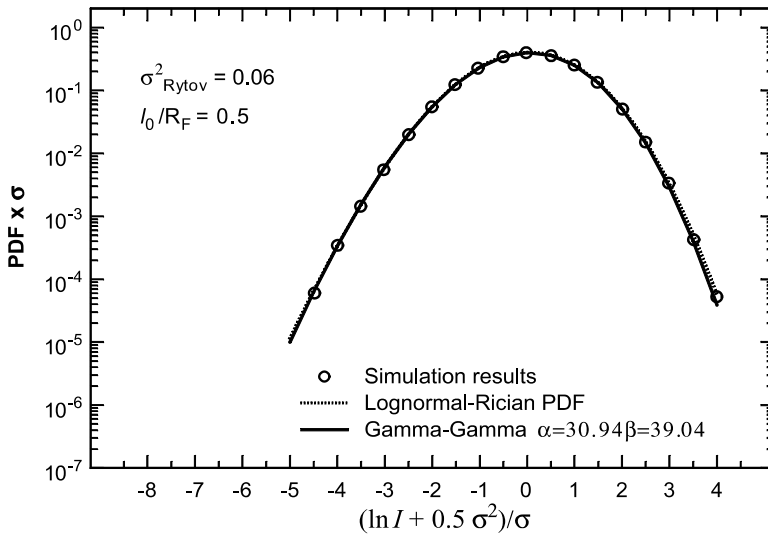

Figure 9.31   Same as Fig. 9.28 with $l_0/R_F = 0.5$.
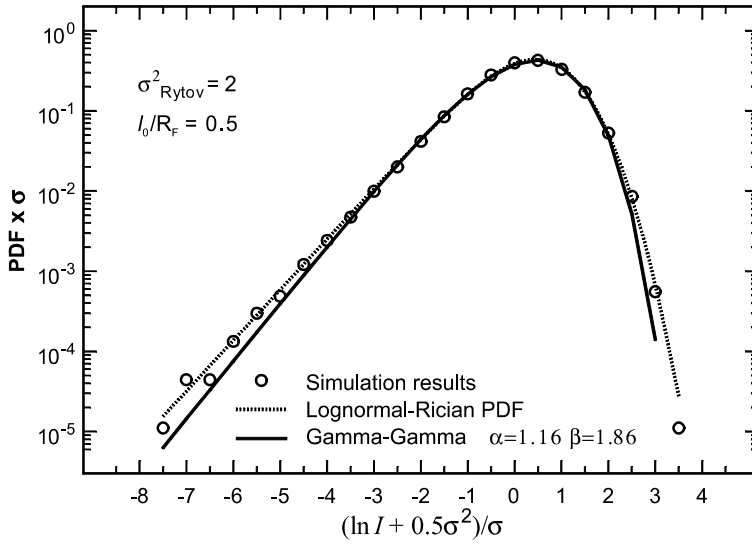
Figure 9.32 Same as Fig. 9.29 with $I_0/R_F = 0.5$.

($Q_l = 11$) in Figs. 9.34–9.36. For the case of $\sigma^2_{\text{Rytov}} = 5$ in Figs. 9.33 and 9.36, the lognormal-Rician PDF did not lend itself directly to numerical calculations and so is omitted [24]. With the exception of Fig. 9.36, the gamma-gamma PDF once again shows good agreement with the simulation results assuming an infinite value of outer scale. In the exceptional case we set the outer scale parameter
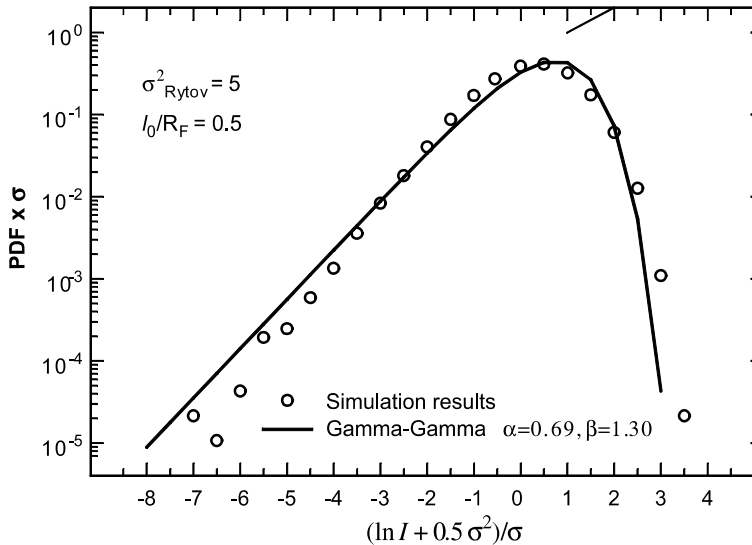
Figure 9.33 Same as Fig. 9.30 with $I_0/R_F = 0.5$ but without the Lognormal-Rician PDF.

Figure 9.34   Same as Fig. 9.28 with $I_0/R_F = 1$.

$Q_0 = 2.2$ and calculated the parameters of the gamma-gamma PDF from the theoretical results provided in Section 9.6.3.

9.11   Summary and Discussion

Under weak irradiance fluctuations ($\sigma_R^2 \ll 1$), the scintillation index of an optical wave propagating through atmospheric turbulence is determined primarily by
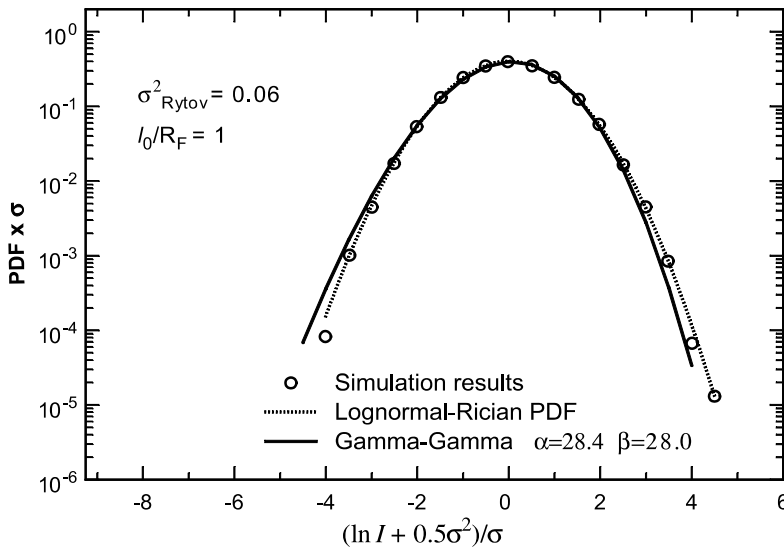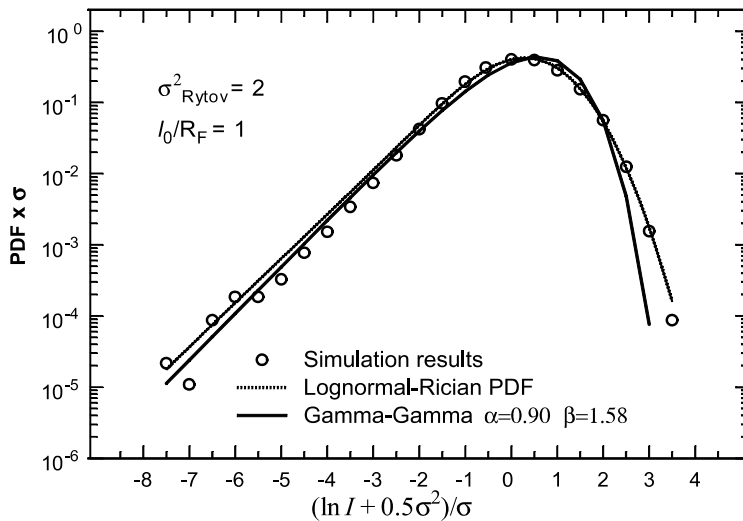

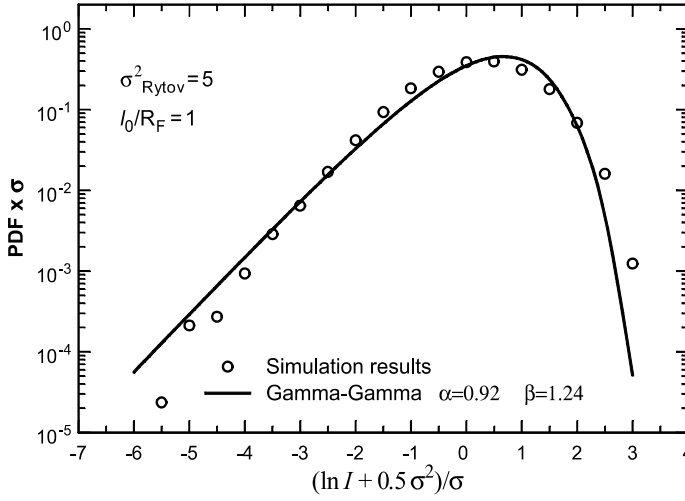**Figure 9.35**   Same as Fig. 9.30 with $I_0/R_F = 1$.

Figure 9.36   Same as Fig. 9.31 with $l_0/R_F = 1$ but without the Lognormal-Rician PDF. Here we set outer scale parameter $Q_0 = 2.2$.

scale sizes on the order of the first *Fresnel zone* $\sqrt{L/k}$, where L is the propagation path length and k is the optical wave number. At the onset of strong irradiance fluctuations, two dominant scale sizes emerge that control the behavior of the scintillation index and covariance function from that point on into the saturation regime. These latter scale sizes are associated, respectively, with the large-scale *scattering disk* $L/k\rho_0$, which is larger than the Fresnel zone, and the small-scale transverse *spatial coherence radius* of the wave ρ_0, which is smaller than the Fresnel zone. The effect of these dominant scale sizes on a propagating optical wave is to induce a "spatial filter" $G(\kappa, l_0, L_0)$ on the atmospheric spectrum that essentially eliminates the effects from scale sizes that lie between the large scale and the small scale. We introduce this filter through the *effective spectrum model*

$$\Phi_{n,e}(\kappa) = 0.033C_n^2\kappa^{-11/3}G(\kappa, l_0, L_0)$$
$$= 0.033C_n^2\kappa^{-11/3}\left[f(\kappa l_0)g(\kappa L_0)\exp\left(-\frac{\kappa^2}{\kappa_X^2}\right) + \frac{\kappa^{11/3}}{(\kappa^2 + \kappa_Y^2)^{11/6}}\right], \quad (145)$$

where l_0 and L_0 denote the inner scale and outer scale, respectively, of the turbulence. The introduction of such a filter in describing atmospheric effects on a propagating wave is comparable to the introduction of inner scale and outer scale filters commonly associated with the Tatarskii and von Kármán spectrum models, among others. The factors $f(\kappa l_0)$ and $g(\kappa L_0)$ appearing in (145) describe inner scale and outer scale filter modifications to the basic Kolmogorov power law, which we take to be defined by

$$f(\kappa l_0) = \exp\left(-\kappa^2/\kappa_l^2\right)\left[1 + 1.802(\kappa/\kappa_l) - 0.254(\kappa/\kappa_l)^{7/6}\right], \qquad \kappa_l = 3.3/l_0,$$
(146)

$$g(\kappa L_0) = 1 - \exp\left(-\frac{\kappa^2}{\kappa_0^2}\right), \qquad \kappa_0 = 8\pi/L_0.$$
(147)

Last, κ_X is a large-scale (or refractive) spatial frequency cutoff and κ_Y is a small-scale (or diffractive) spatial frequency cutoff, which identify the spatial scale sizes beyond which and prior to are essentially ineffective in producing scintillation effects.

Because there is no radial dependency of the scintillation index in the special cases of an infinite plane wave and a spherical wave, *beam wander* is not an issue for such optical waves. In the case of a finite Gaussian beam, however, beam wander effects may increase the scintillation index by a significant amount over that in its absence if the transmitted beam is converging. In such cases we must carefully distinguish between an *untracked beam* and a *tracked beam*. For a collimated or divergent beam propagating along a horizontal path, we find that beam wander effects on scintillation are generally negligible in the untracked case.

In the absence of inner scale and outer scale effects [i.e., $f(\kappa l_0) = g(\kappa L_0) = 1$] the *scintillation index* on the optical axis of an *untracked* collimated or divergent Gaussian-beam wave based on the Kolmogorov spectrum and *weak irradiance fluctuations* is basically that obtained from conventional Rytov theory, viz.,

$$
\begin{aligned}
\sigma_B^2 &= 3.86\sigma_R^2 Re\left[i^{5/6}\,{}_2F_1\left(-\frac{5}{6}, \frac{11}{6}; \frac{17}{6}; \overline{\Theta} + i\Lambda\right) - \frac{11}{16}\Lambda^{5/6}\right] \\
&\cong 3.86\sigma_R^2\left\{0.40[(1 + 2\Theta)^2 + 4\Lambda^2]^{5/12}\right. \\
&\quad \left.\times \cos\left[\frac{5}{6}\tan^{-1}\left(\frac{1 + 2\Theta}{2\Lambda}\right)\right] - \frac{11}{16}\Lambda^{5/6}\right\}.
\end{aligned}
$$
(148)

The second expression in (148) is an accurate approximation to the first line in (148) except for the case of a large-aperture focused beam which we have generally neglected in our discussion. Under *moderate-to-strong irradiance fluctuations*, and taking into account off-axis points as well as on-axis points, the scintillation index throughout the beam profile based on a Kolmogorov spectrum takes the form

$$
\begin{aligned}
\sigma_I^2(\mathbf{r}, L)_{\text{untracked}} &= 4.42\sigma_R^2\Lambda_e^{5/6}\frac{r^2}{W_{\text{LT}}^2} + \exp\left\{\frac{0.49\sigma_B^2}{\left[1 + 0.56(1 + \Theta)\sigma_B^{12/5}\right]^{7/6}}\right. \\
&\quad \left.+ \frac{0.51\sigma_B^2}{\left(1 + 0.69\sigma_B^{12/5}\right)^{5/6}}\right\} - 1, \qquad 0 \le r < W,
\end{aligned}
$$
(149)

where W_{LT} is the long-term spot size of the beam. The first term represents the radial component where the effective beam parameter Λ_e is defined by

$$\Lambda_e = \frac{2L}{kW_{LT}^2} = \frac{\Lambda}{1 + 1.63\sigma_R^{12/5}\Lambda}, \tag{150}$$

and σ_B^2 is the longitudinal component under weak irradiance fluctuations defined by (148). The comparable plane wave and spherical wave expressions are readily deduced from (148) and (149) by setting $\Theta = 1$, $\Lambda = 0$, and $\Theta = \Lambda = 0$, respectively.

If the beam is *tracked* (i.e., beam wander effects are removed), we define the corresponding scintillation index of a collimated or divergent Gaussian-beam wave by

$$\sigma_I^2(\mathbf{r}, L)_{\text{tracked}} = 4.42\sigma_R^2\Lambda_e^{5/6}\left(\frac{r^2 - \sqrt{\langle r_c^2 \rangle}}{W_{LT}^2}\right)^2 + \exp\left\{\frac{0.49\sigma_B^2}{\left[1 + 0.56(1 + \Theta)\sigma_B^{12/5}\right]^{7/6}}\right.$$

$$\left. + \frac{0.51\sigma_B^2}{\left(1 + 0.69\sigma_B^{12/5}\right)^{5/6}}\right\} - 1, \qquad \sqrt{\langle r_c^2 \rangle} \le r < W. \tag{151}$$

If we include the effects of inner scale and outer scale, the scintillation index for the untracked (collimated or divergent) beam becomes

$$\sigma_I^2(\mathbf{r}, L)_{\text{untracked}} = 4.42\sigma_R^2\Lambda_e^{5/6}\left[1 - 1.15\left(\frac{\Lambda_e L}{kL_0^2}\right)^{1/6}\right]\frac{r^2}{W_{LT}^2}$$

$$+ \exp\left[\sigma_{\ln X}^2(l_0) - \sigma_{\ln X}^2(L_0) - \frac{0.51\sigma_G^2}{\left(1 + 0.69\sigma_G^{12/5}\right)^{5/6}}\right] - 1,$$

$$\sqrt{\langle r_c^2 \rangle} \le r < W, \tag{152}$$

where $\sigma_{\ln X}^2(l_0)$ is defined by Eq. (108), $\sigma_{\ln X}^2(L_0)$ is defined by Eq. (110), and σ_G^2 is given by Eq. (104). The same for the tracked beam case is

$$\sigma_I^2(\mathbf{r}, L)_{\text{tracked}} = 4.42\sigma_R^2\Lambda_e^{5/6}\left[1 - 1.15\left(\frac{\Lambda_e L}{kL_0^2}\right)^{1/6}\right]\left(\frac{r^2 - \langle r_c^2 \rangle}{W_{LT}^2}\right)$$

$$+ \exp\left[\sigma_{\ln X}^2(l_0) - \sigma_{\ln X}^2(L_0) - \frac{0.51\sigma_G^2}{\left(1 + 0.69\sigma_G^{12/5}\right)^{5/6}}\right] - 1,$$

$$\sqrt{\langle r_c^2 \rangle} \le r < W. \tag{153}$$

The *covariance function* is important for calculating the *irradiance correlation width*. In the case of an *infinite plane wave*, the covariance function is approximated by (ignoring inner and outer scale effects)

$$
B_{I,\,\text{pl}}(\rho) = \exp\left[\frac{0.49\sigma_R^2}{\left(1 + 1.11\sigma_R^{12/5}\right)^{7/6}} \,_1F_1\left(\frac{7}{6}; 1; -\frac{k\rho^2\eta_X}{4L}\right) \right.
$$

$$
\left. + \frac{0.50\sigma_R^2}{\left(1 + 0.69\sigma_R^{12/5}\right)^{5/6}} \left(\frac{k\rho^2\eta_Y}{L}\right)^{5/12} K_{5/6}\left(\sqrt{\frac{k\rho^2\eta_Y}{L}}\right) \right] - 1, \quad (154)
$$

where $_1F_1(a;c;x)$ is a confluent hypergeometric function, $K_v(x)$ is a modified Bessel function, and

$$
\eta_X = \frac{2.61}{1 + 1.11\sigma_R^{12/5}}, \quad \eta_Y = 3\left(1 + 0.69\sigma_R^{12/5}\right). \quad (155)
$$

The correlation width ρ_c is on the order of the first Fresnel zone under weak irradiance fluctuations and approaches the spatial coherence radius ρ_0 under very strong fluctuations. Equation (121) represents the plane wave covariance function when inner scale effects are included, and Eq. (125) is the covariance function for a spherical wave in the absence of inner scale and outer scale effects. A comparable expression for a Gaussian-beam wave has not yet been calculated.

The *temporal spectrum* for an infinite plane wave is defined by the Fourier transform relation

$$
S_I(\omega) = 4\int_0^\infty B_{I,\,\text{pl}}(\tau, L)\cos\omega\tau\,d\tau, \quad (156)
$$

where the *temporal covariance function* obtained through Taylor's frozen-turbulence hypothesis is

$$
B_{I,\,\text{pl}}(\tau, L) = \exp\left[\frac{0.49\sigma_R^2}{\left(1 + 1.11\sigma_R^{12/5}\right)^{7/6}} \,_1F_1\left(\frac{7}{6}; 1; -\frac{kV_\perp^2\tau^2\eta_X}{4L}\right) \right.
$$

$$
\left. + \frac{0.50\sigma_R^2}{\left(1 + 0.69\sigma_R^{12/5}\right)^{5/6}} \left(\frac{kV_\perp^2\tau^2\eta_Y}{L}\right)^{5/12} K_{5/6}\left(\sqrt{\frac{kV_\perp^2\tau^2\eta_Y}{L}}\right) \right] - 1.
$$

$$
(157)
$$

The quantity $V_\perp$ denotes the transverse wind speed.

Last, we introduced several models for the probability density function (PDF) in Sections 9.9 and 9.10 that govern irradiance fluctuations. In weak fluctuations, the *lognormal model* described by

$$
p_I(I) = \frac{1}{I\sigma_I(\mathbf{r},L)\sqrt{2\pi}} \exp\left\{ -\frac{\left[\ln\left(\dfrac{I}{\langle I(\mathbf{r},L)\rangle}\right) + \dfrac{1}{2}\sigma_I^2(\mathbf{r},L)\right]^2}{2\sigma_I^2(\mathbf{r},L)} \right\} \quad (158)
$$

is often used for calculating the probability of fade for an optical signal, but as shown in Figs. 9.23–9.36, the lognormal model does not fit the simulation data very well in the tails of the distribution. Unfortunately, when calculating fade probabilities (e.g., see Chaps. 11 and 12), it is the behavior of the PDF tail near the origin that is most important. The *gamma-gamma PDF model* is defined by

$$
p_I(I) = \frac{2(\alpha\beta)^{(\alpha+\beta)/2}}{\Gamma(\alpha)\Gamma(\beta)I}\left(\frac{I}{\langle I(\mathbf{r},L)\rangle}\right)^{(\alpha+\beta)/2} K_{\alpha-\beta}\left(2\sqrt{\frac{\alpha\beta I}{\langle I(\mathbf{r},L)\rangle}}\right), \quad I > 0, \quad (159)
$$

where α and β are positive parameters directly related to the large-scale and small-scale scintillations of the optical wave according to

$$
\begin{aligned}
\alpha &= \frac{1}{\sigma_X^2} = \frac{1}{\exp(\sigma_{\ln X}^2) - 1}, \\
\beta &= \frac{1}{\sigma_Y^2} = \frac{1}{\exp(\sigma_{\ln Y}^2) - 1}.
\end{aligned} \quad (160)
$$

In Figs. 9.23–9.36 we showed that the gamma-gamma model provides a good fit to simulation data for both plane waves and spherical waves, including the behavior in the tails. Moreover, because the parameters (160) of this distribution are determined entirely from knowledge of the atmospheric structure parameter C_n^2, inner scale l_0, and outer scale L_0, through the large-scale and small-scale irradiance fluctuations of the propagating optical wave, this model is much easier to use in practice than other PDF models whose parameters are not known.

9.12 Worked Examples

Example 1: A collimated Gaussian-beam wave is propagated through atmospheric turbulence to a receiver located 1000 meters from the transmitter. Assume the initial beam characteristics of a unit-amplitude Gaussian beam at the transmitter are given by

$$W_0 = 0.01 \, \text{m},$$
$$F_0 = \infty,$$
$$\lambda = 0.633 \, \mu\text{m},$$

and that $C_n^2 = 0.5 \times 10^{-13} \, \text{m}^{-2/3}$. If we further assume the beam is *not tracked*,

(a) calculate the on-axis scintillation index at the receiver. What is the total scintillation index at the diffractive beam edge?
(b) If the propagation distance is increased to 2.5 km, what is the corresponding scintillation index at each position?

Solution: We first calculate the parameters:

$$L = 1000 \, \text{m:} \quad \Theta_0 = 1, \quad \Lambda_0 = \frac{2L}{kW_0^2} = 2.015,$$

$$\Theta = \frac{\Theta_0}{\Theta_0^2 + \Lambda_0^2} = 0.198, \quad \Lambda = \frac{\Lambda_0}{\Theta_0^2 + \Lambda_0^2} = 0.398,$$

$$\sigma_R^2 = 1.23 C_n^2 k^{7/6} L^{11/6} = 2.83, \quad r_0 = (0.16 C_n^2 k^2 L)^{-3/5} = 1.83 \, \text{cm},$$

$$\sigma_{pe} = \sqrt{0.48 \left(\frac{\lambda L}{2W_0}\right)^2 \left(\frac{2W_0}{r_0}\right)^{5/3} \left[1 - \left(\frac{C_r^2 W_0^2 / r_0^2}{1 + C_r^2 W_0^2 / r_0^2}\right)^{1/6}\right]} = 0.27 \, \text{cm}$$

$$L = 2500 \, \text{m:} \quad \Theta_0 = 1, \quad \Lambda_0 = \frac{2L}{kW_0^2} = 5.037,$$

$$\Theta = \frac{\Theta_0}{\Theta_0^2 + \Lambda_0^2} = 0.038, \quad \Lambda = \frac{\Lambda_0}{\Theta_0^2 + \Lambda_0^2} = 0.191,$$

$$\sigma_R^2 = 15.18, \quad r_0 = 1.06 \, \text{cm}, \quad \sigma_{pe} = 0.63 \, \text{cm}$$

(a) The on-axis scintillation index is calculated from (102) and that at the diffractive beam edge $r = W$ from (103), which gives us

$$L = 1000 \, \text{m} \, (l_0 = 0, L_0 = \infty): \quad \sigma_I^2(0, L) = 0.63, \quad \sigma_I^2(W, L) = 1.29.$$

(b) Increasing the propagation distance to 2.5 km, we have

$$L = 2500 \, \text{m} \, (l_0 = 0, L_0 = \infty): \quad \sigma_I^2(0, L) = 1.58, \quad \sigma_I^2(W, L) = 2.12.$$

❑

In Example 1 above the effects of beam wander for an untracked beam have not significantly altered the results from conventional Rytov theory. However, in Example 2 below, we examine the same scintillation statistics for a tracked beam for the purpose of comparison with the untracked beam.

Example 2: A collimated Gaussian-beam wave is propagated through atmospheric turbulence to a receiver located 1000 meters from the transmitter. Assume the initial beam characteristics of a unit-amplitude Gaussian beam at the transmitter are given by the same conditions as listed in Example 1 and that $C_n^2 = 0.5 \times 10^{-13}\,\text{m}^{-2/3}$. If the beam is *tracked* in this case,

   (a) calculate the on-axis scintillation index at the receiver. What is the total scintillation index at the diffractive beam edge?
   (b) If the propagation distance is increased to 2.5 km, what is the corresponding scintillation index at each position?

Solution: We first calculate the parameters:

$$L = 1000\,\text{m}: \quad \Theta_0 = 1, \quad \Lambda_0 = \frac{2L}{kW_0^2} = 2.015,$$

$$\Theta = \frac{\Theta_0}{\Theta_0^2 + \Lambda_0^2} = 0.198, \quad \Lambda = \frac{\Lambda_0}{\Theta_0^2 + \Lambda_0^2} = 0.398,$$

$$\sigma_R^2 = 1.23 C_n^2 k^{7/6} L^{11/6} = 2.83, \quad r_0 = (0.16 C_n^2 k^2 L)^{-3/5} = 1.83\,\text{cm},$$

$$\sqrt{\langle r_c^2 \rangle} = 0.69 \left(\frac{\lambda L}{2W_0} \right) \left(\frac{2W_0}{r_0} \right)^{5/6} = 2.32\,\text{cm}$$

$$L = 2500\,\text{m}: \quad \Theta_0 = 1, \quad \Lambda_0 = \frac{2L}{kW_0^2} = 5.037,$$

$$\Theta = \frac{\Theta_0}{\Theta_0^2 + \Lambda_0^2} = 0.038, \quad \Lambda = \frac{\Lambda_0}{\Theta_0^2 + \Lambda_0^2} = 0.191,$$

$$\sigma_R^2 = 15.18, \quad r_0 = 1.06\,\text{cm}, \quad \langle r_c^2 \rangle = 8.49\,\text{cm}$$

   (a) Here we find that the assumption of an infinite outer scale yields a larger value of beam wander displacement than with a finite value. The on-axis scintillation index and that at the diffractive beam edge lead to

$$L = 1000\,\text{m}\,(l_0 = 0, L_0 = \infty): \quad \sigma_I^2(0, L) = 0.61, \quad \sigma_I^2(W, L) = 0.61.$$

   (b) Increasing the propagation distance to 2.5 km, we find

$$L = 2500\,\text{m}(l_0 = 0, L_0 = \infty): \quad \sigma_I^2(0, L) = 1.57, \quad \sigma_I^2(W, L) = 1.87.$$

❑

Problems

Section 9.2

1. Use the Kolmogorov spectrum to compare the relative sizes of the spatial coherence radius, Fresnel zone, and scattering disk as defined in (2) for a plane wave, using $L = 1\,\text{km}$, $C_n^2 = 1.7 \times 10^{-13}\,\text{m}^{-2/3}$, and wavelength
   (a) $\lambda = 0.5\,\mu\text{m}$.
   (b) $\lambda = 1\,\mu\text{m}$.
   (c) $\lambda = 1.5\,\mu\text{m}$.
   (d) $\lambda = 2\,\mu\text{m}$.

2. Verify that the large-scale and small-scale scintillations described by (11) are consistent with the relations given by (12) and (9).

Section 9.3

3. For an infinite plane wave, show that the last integral appearing in Eq. (13) leads to the result

$$\int_0^1 D_S\left[\frac{L\kappa}{k}w(\tau,\xi)\right]d\tau = 2.37\sigma_R^2\left(\frac{L}{k}\right)^{5/6}\kappa^{5/3}\xi^{5/3}\left(1 - \frac{5}{8}\xi\right).$$

4. Use properties of the gamma function in evaluating the inside integral in (17) and show that it leads to

$$2.12\sigma_R^2\left(\frac{L}{k}\right)^{7/6}\int_0^1 \xi^2\int_0^\infty \kappa^{4/3}\exp\left[-2.37\sigma_R^2\left(\frac{L}{k}\right)^{5/6}\kappa^{5/3}\xi^{5/3}\left(1 - \frac{5}{8}\xi\right)\right]d\kappa\,d\xi$$

$$= \frac{0.34}{\sigma_R^{4/5}}\int_0^1 \frac{\xi^{-1/3}}{\left(1 - \frac{5}{8}\xi\right)^{7/5}}d\xi.$$

5. For an infinite plane wave and the modified atmospheric spectrum, show that the last integral appearing in Eq. (13) leads to the result

$$\int_0^1 D_S\left[\frac{L\kappa}{k}w(\tau,\xi)\right]d\tau = 1.02\sigma_R^2 Q_l^{1/6}\left(\frac{L\kappa^2}{k}\right)\xi^2\left(1 - \frac{2}{3}\xi\right).$$

6. For a spherical wave, derive expressions comparable to those given in Probs. 3 and 5 for the infinite plane wave case.

Section 9.4

7. For a plane wave propagating $3\,\text{km}$ through atmospheric turbulence with $\lambda = 1.55\,\mu\text{m}$, $l_0 = 0$, $L_0 = \infty$, and $C_n^2 = 1.7 \times 10^{-13}$, calculate the scintillation index.

8. Repeat Prob. 7 for the case when the inner scale is 5 mm and the outer scale is 1 m.

Section 9.5

9. Repeat Prob. 7 for a spherical wave.
10. Repeat Prob. 8 for a spherical wave.

Section 9.6

11. Consider a collimated beam propagating 3 km through atmospheric turbulence with $W_0 = 3\,\text{cm}$, $\lambda = 1.55\,\mu\text{m}$, $l_0 = 0$, $L_0 = \infty$, and $C_n^2 = 1.7 \times 10^{-13}$. What is the on-axis (longitudinal) component of the scintillation index if
    (*a*) the beam is tracked.
    (*b*) the beam is not tracked.
    Ans. (*a*) 1.48 (*b*) 1.48

12. Repeat Prob. 11 for a beam of radius 1 cm. What is the corresponding scintillation index off axis at $r = W$ when the beam is not tracked?

13. Consider a collimated beam propagating 3 km through atmospheric turbulence with $W_0 = 1\,\text{cm}$, $\lambda = 1.55\,\mu\text{m}$, $l_0 = 5\,\text{mm}$, $L_0 = 1\,\text{m}$, and $C_n^2 = 1.7\times 10^{-13}$. What is the on-axis (longitudinal) component of the scintillation index if
    (*a*) the beam is tracked.
    (*b*) the beam is not tracked.

14. Repeat Prob. 13 if the wavelength is changed to 1.06 μm.

Section 9.7

15. Use Eq. (120) to estimate the correlation width ρ_c at the $1/e^2$ position for an infinite plane wave with $\lambda = 1.55\,\mu\text{m}$, $l_0 = 0$, $L_0 = \infty$, and $C_n^2 = 1.7 \times 10^{-13}$,
    (*a*) if propagation distance is 500 m.
    (*b*) if propagation distance is 2000 m.
    (*c*) if propagation distance is 5000 m.

Section 9.8

16. Use the spherical wave expression (125) for the spatial covariance function to infer the corresponding temporal covariance function for the spherical wave. *Hint:* Recall Section 8.5.2.

Section 9.9

17. Show that the substitution of (129) and (131) into the integral (130) yields the *K* distribution
$$p(I) = \frac{2\alpha}{\Gamma(\alpha)}(\alpha I)^{(\alpha-1)/2}K_{\alpha-1}(2\sqrt{\alpha I}), \quad I > 0.$$

18. Show that the K distribution with $\alpha \to \infty$ leads to the negative exponential distribution, i.e., show that

$$\lim_{\alpha \to \infty} \frac{2\alpha}{\Gamma(\alpha)} (\alpha I)^{(\alpha-1)/2} K_{\alpha-1}(2\sqrt{\alpha I}) = e^{-I}.$$

Section 9.10

19. Show that the substitution of (134) and (135) into the integral (130) yields the gamma-gamma distribution

$$p(I) = \frac{2(\alpha\beta)^{(\alpha+\beta)/2}}{\Gamma(\alpha)\Gamma(\beta)} I^{(\alpha+\beta)/2-1} K_{\alpha-\beta}(2\sqrt{\alpha\beta I}), \quad I < 0.$$

20. By using the identity given by Eq. (13) in Appendix A, use termwise integration to show that the cumulative distribution function for the gamma-gamma distribution is

$$P(I \leq I_T) = \frac{\pi}{\sin[\pi(\alpha - \beta)]\Gamma(\alpha)\Gamma(\beta)}$$

$$\times \left\{ \frac{(\alpha\beta I_T)^{\beta}}{\beta\Gamma(\beta - \alpha + 1)} {}_1F_2(\beta; \beta + 1, \beta - \alpha + 1; \alpha\beta I_T) \right.$$

$$\left. - \frac{(\alpha\beta I_T)^{\alpha}}{\alpha\Gamma(\alpha - \beta + 1)} {}_1F_2(\alpha; \alpha + 1, \alpha - \beta + 1; \alpha\beta I_T) \right\}.$$

References

1. V. I. Tatarskii, *Wave Propagation in a Turbulent Medium*, trans. by R. A. Silverman (McGraw-Hill, New York, 1961).

2. L. A. Chernov, *Wave Propagation in a Random Medium*, trans. by R. A. Silverman (McGraw-Hill, New York, 1960).

3. V. I. Tatarskii, *The Effects of the Turbulent Atmosphere on Wave Propagation* (Keter, Jerusalem, 1971).

4. M. E. Gracheva and A. S. Gurvich, "Strong fluctuations in the intensity of light propagated through the atmosphere close to the earth," *Izvestiya VUZ. Radiofizika* **8**, 717–724 (1965).

5. J. R. Dunphy and J. Kerr, "Scintillation measurements for large integrated-path turbulence," *J. Opt. Soc. Am.* **63**, 981–986 (1973).

6. M. Gracheva, A. S. Gurvich, S. S. Kashkarov, and V. V. Pokasov, "Similarity relations for strong fluctuations of light in a turbulent medium," *Sov. Phys. JETP* **40**, 1011–1016 (1974).

7. H. T. Yura, "Physical model for strong optical-amplitude fluctuations in a turbulent medium," *J. Opt. Soc. Am.* **64**, 59–67 (1974).

8. S. F. Clifford, G. R. Ochs, and R. S. Lawrence, "Saturation of optical scintillation by strong turbulence," *J. Opt. Soc. Am.* **64**, 148–154 (1974).

9. R. J. Hill and S. F. Clifford, "Theory of saturation of optical scintillation by strong turbulence for arbitrary refractive-index spectra," *J. Opt. Soc. Am.* **71**, 675–686 (1981).

10. R. G. Frehlich, S. M. Wandzura, and R. J. Hill, "Log-amplitude covariance for waves propagating through very strong turbulence," *J. Opt. Soc. Am. A* **4**, 2158–2161 (1987).

11. R. J. Hill and R. G. Frehlich, "Onset of strong scintillation with application-to remote sensing of turbulence inner scale," *Appl. Opt.* **35**, 986–997 (1996).

12. K. S. Gochelashvili and V. I. Shishov, "Saturated fluctuations in the laser radiation intensity in a turbulent medium," *Sov. Phys. JETP* **39**, 605–609 (1974).

13. R. L. Fante, "Inner-scale size effect on the scintillations of light in the turbulent atmosphere," *J. Opt. Soc. Am.* **73**, 277–281 (1983).

14. R. G. Frehlich, "Intensity covariance of a point source in a random medium with a Kolmogorov spectrum and an inner scale of turbulence," *J. Opt. Soc. Am. A* **4**, 360–366 (1987); "Intensity covariance of a point source in a random medium with a Kolmogorov spectrum and an inner scale of turbulence: Errata," *J. Opt. Soc. Am. A* **4**, 1324 (1987).

15. G. Parry, "Measurements of atmospheric turbulence-induced intensity fluctuations in a laser beam," *Opt. Acta* **28**, 715–728 (1981).

16. R. L. Phillips and L. C. Andrews, "Measured statistics of laser-light scattering in atmospheric turbulence," *J. Opt. Soc. Am.* **71**, 1440–1445 (1981).

17. W. R. Coles and R. G. Frehlich, "Simultaneous measurements of angular scattering and intensity scintillation in the atmosphere," *J. Opt. Soc. Am.* **72**, 1042–1048 (1982).

18. A. Consortini, R. Cochetti, J. H. Churnside, and R. J. Hill, "Inner-scale effect on irradiance variance measured for weak-to-strong atmospheric scintillation," *J. Opt. Soc. Am. A* **10**, 2354–2362 (1993).

19. J. M. Martin and S. M. Flatté, "Intensity images and statistics from numerical simulation of wave propagation in 3-D random media," *Appl. Opt.* **27**, 2111–2126 (1988).

20. J. M. Martin and S. M. Flatté, "Simulation of point-source scintillation through three-dimensional random media," *J. Opt. Soc. Am. A* **7**, 838–847 (1990).

21. S. M. Flatté, G. Wang, and J. Martin, "Irradiance variance of optical waves through atmospheric turbulence by numerical simulation and comparison with experiment," *J. Opt. Soc. Am. A* **10**, 2363–2370 (1993).

22. S. M. Flatté, C. Bracher, and G.-Y. Wang, "Probability-density functions of irradiance for waves in atmospheric turbulence calculated by numerical simulations," *J. Opt. Soc. Am. A* **11**, 2080–2092 (1994).

23. R. J. Hill, R. G. Frehlich, and W. D. Otto, "The probability distribution of irradiance scintillation," NOAA Tech. Memo. ERL ETL-274 (NOAA Environmental Research Laboratories, Boulder, CO, 1996).

24. R. J. Hill and R. G. Frehlich, "Probability distribution of irradiance for the onset of strong scintillation," *J. Opt. Soc. Am. A* **14**, 1530–1540 (1997).

25. S. M. Flatté and J. S. Gerber, "Irradiance-variance behavior by numerical simulation for plane-wave and spherical-wave optical propagation through strong turbulence," *J. Opt. Soc. Am. A* **17**, 1092–1097 (2000).

26. L. C. Andrews, R. L. Phillips, C. Y. Hopen, and M. A. Al-Habash, "Theory of optical scintillation," *J. Opt. Soc. Am. A* **16**, 1417–1429 (1999).

27. L. C. Andrews, R. L. Phillips, and C. Y. Hopen, "Scintillation model for a satellite communication link at large zenith angles," *Opt. Eng.* **39**, 3272–3280 (2000).

28. L. C. Andrews, R. L. Phillips, and C. Y. Hopen, "Aperture averaging of optical scintillations: power fluctuations and the temporal spectrum," *Waves Random Media* **10**, 53–70 (2000).

29. L. C. Andrews, M. A. Al-Habash, C. Y. Hopen, and R. L. Phillips, "Theory of optical scintillation: Gaussian-beam wave model," *Waves Random Media* **11**, 271–291 (2001).

30. L. C. Andrews, R. L. Phillips, and C. Y. Hopen, *Laser Beam Scintillation with Applications* (SPIE Press, Bellingham, Wash., 2001).

31. D. J. Lewinski, "Nonstationary probabilistic target and clutter scattering models," *IEEE Trans. Antenn. Prop.* **AP-31**, 490–498 (1983).

32. V. I. Tatarskii and V. U. Zavorotnyi, "Wave propagation in random media with fluctuating turbulent parameters," *J. Opt. Soc. Am. A* **2**, 2069–2076 (1985).

33. M. C. Teich and P. Diament, "Multiply stochastic representations for *K* distributions and their Poisson transforms," *J. Opt. Soc. Am. A* **6**, 80–91 (1989).

34. A. M. Prokhorov, F. V. Bunkin, K. S. Gochelashvily, and V. I. Shishov, "Laser irradiance in turbulent media," *Proc. IEEE* **63**, 790–809 (1975).

35. V. I. Tatarskii and V. U. Zavorotnyi, "Strong fluctuations in light propagation in a randomly inhomogeneous medium," in *Progress in Optics III*, W. Wolf, ed. (Elsevier, New York, 1980).

36. J. C. Ricklin, W. B. Miller, and L. C. Andrews, "Effective beam parameters and the turbulent beam waist for initially convergent Gaussian beams," *Appl. Opt.* **34**, 7059–7065 (1995).

37. W. B. Miller, J. C. Ricklin, and L. C. Andrews, "Effects of the refractive index spectral model on the irradiance variance of a Gaussian beam," *S. Opt. Soc. Am. A* **11**, 2719–2726 (1994).

38. L. C. Andrews, W. B. Miller, and J. C. Ricklin, "Spatial coherence of a Gaussian beam in weak and strong optical turbulence," *J. Opt. Soc. Am. A* **11**, 1653–1660 (1994).

39. W. B. Miller, J. C. Ricklin, and L. C. Andrews, "Scintillation of initially convergent Gaussian beams in the vicinity of the geometric focus," *Appl. Opt.* **34**, 7066–7073 (1995).

40. L. C. Andrews, *Special Functions of Mathematics for Engineers*, 2nd ed. (SPIE Optical Engineering Press, Bellingham, Wash.; Oxford University Press, Oxford, 1998); [formerly published as 2nd ed. by McGraw-Hill, New York (1992)].

41. A. Belmonte, "Feasibility study for the simulation of beam propagation: consideration of coherent lidar performance," *Appl. Opt.* **39**, 5428–5445 (2000).

42. M. E. Gracheva, A. S. Gurvich, S. S. Kasharov, and V. V. Pokasov, "Similarity relations and their experimental verification for strong intensity fluctuations of laser radiation," in J. W. Strohbehn, ed., *Laser Beam Propagation in the Atmosphere*, Springer, New York (1978).

43. J. H. Churnside and R. G. Frehlich, "Experimental evaluation of log-normally modulated Rician and *IK* models of optical scintillation in the atmosphere," *J. Opt. Soc. Am. A* **6**, 1760–1766 (1989).

44. E. Jakeman and P. N. Pusey, "A model for non-Rayleigh sea echo," *IEEE Trans. Antenn. Propag.* **AP-24**, 806–814 (1976).

45. E. Jakeman and P. N. Pusey, "The significance of *K*-distributions in scattering experiments," *Phys. Rev. Lett.* **40**, 546–550 (1978).

46. G. Parry and P. N. Pusey, "*K* distributions in atmospheric propagation of laser light," *J. Opt. Soc. Am.* **69**, 796–798 (1979).

47. E. Jakeman, "On the statistics of *K*-distributed noise," *J. Phys. A* **13**, 31–48 (1980).

48. L. C. Andrews and R. L. Phillips, "*I-K* distribution as a universal propagation model of laser beams in atmospheric turbulence," *J. Opt. Soc. Am. A* **2**, 160–163 (1985).

49. L. C. Andrews and R. L. Phillips, "Mathematical genesis of the *I-K* distribution for random optical fields," *J. Opt. Soc. Am. A* **3**, 1912–1919 (1986).

50. L. C. Andrews, R. L. Phillips, and B. K. Shivamoggi, "Relations of the parameters of the *I-K* distribution for irradiance fluctuations to physical parameters of the turbulence," *Appl. Opt.* **27**, 2150–2156 (1988).

51. J. H. Churnside and R. J. Hill, "Probability density of irradiance scintillations for strong path-integrated refractive turbulence," *J. Opt. Soc. Am. A* **4**, 727–733 (1987).

52. J. H. Churnside and S. F. Clifford, "Log-normal Rician probability-density function of optical scintillations in the turbulent atmosphere," *J. Opt. Soc. Am. A* **4**, 1923–1930 (1987).

53. M. A. Al-Habash, L. C. Andrews, and R. L. Phillips, "Mathematical model for the irradiance PDF of a laser beam propagating through turbulent media," *Opt. Eng.* **40**, 1554–1562 (2001).

54. M. Nakagami, "The *m* distribution—a general formula of intensity distribution of rapid fading," pp. 3–36 in *Statistical Methods in Radio Wave Propagation*, W. C. Hoffman, ed., Pergamon, New York (1960).

55. V. S. R. Gudimetla and J. F. Holmes, "Probability density function of the intensity for a laser-generated speckle field after propagation through the turbulent atmosphere," *J. Opt. Soc. Am.* **72**, 1213–1218 (1982).